

The Pennsylvania State University
The Graduate School
Department of Mechanical and Nuclear Engineering

**TRANSMISSION ELECTRON MICROSCOPY OF OXIDES FORMED ON
GENERATION-IV CANDIDATE STEEL ALLOYS**

A Thesis in
Nuclear Engineering
by
Andrew D. Siwy

© 2008 Andrew D. Siwy

Submitted in Partial Fulfillment
of the Requirements
for the Degree of

Master of Science

May 2008

The thesis of Andrew D. Siwy was reviewed and approved* by the following:

Arthur Motta
Professor of Nuclear Engineering and Materials Science and Engineering
Thesis Advisor

Elizabeth Dickey
Associate Professor of Materials Science and Engineering
Associate Director, Materials Research Institute

Lawrence Hochreiter
Professor of Mechanical and Nuclear Engineering

Jack Brenizer
Professor of Mechanical and Nuclear Engineering
Chair of Nuclear Engineering

*Signatures are on file in the Graduate School

ABSTRACT

Generation-IV reactors are currently being studied to help meet future demands for energy production. The operating conditions of Gen-IV reactors provide new material challenges for many reactor components, including fuel cladding. Uniform corrosion is a major concern for fuel cladding in two of these reactors: the Lead-cooled Fast Reactor (LFR) and the Supercritical Water Reactor (SCWR). In this study, oxide layers formed on alloys 9Cr ODS and HT-9 that were exposed to a corrosion medium of supercritical water (SCW), and alloys HT-9 and a model alloy (91 wt% Fe and 9 wt% Cr) that were exposed to a corrosion medium of lead-bismuth eutectic (LBE), are studied in cross-section using transmission electron microscopy to reveal the reasons for their different corrosion behavior on the basis of their oxide structure.

The oxide layers formed on these alloys were examined using primarily transmission electron microscopy (TEM) diffraction and imaging, along with energy dispersive x-ray spectroscopy, and electron energy loss spectroscopy, (and also using optical microscopy and scanning electron microscopy) to complement microbeam synchrotron x-ray fluorescence and diffraction, which was performed in parallel on the same samples. The TEM specimens were fabricated using a focused ion beam, which allowed site-specific samples of areas up to ten times larger than those provided by traditional methods.

The details of the examination of the oxide layers formed on these alloys are presented in this thesis. Examination shows that these alloys form sub-layers consisting of a magnetite outer oxide layer and a spinel inner oxide layer. In between the inner oxide

layer and the metal of the oxides formed in SCW, an additional internal oxidation layer of chromate (9Cr ODS only), spinel, and ferrite was found. The morphology of the oxide grains is characteristic of each corrosion medium.

From the examination of the oxide layer formed of 9Cr ODS, it appears that FeCr_2O_4 initially develops within the internal oxidation layer along the metal grain boundaries. Between two weeks and four weeks of corrosion, the thickness of the internal oxidation layer shrinks relative to the inner oxide thickness due to corrosion retardation caused by a band of chromate (Cr_2O_3) at the metal/internal oxidation layer interface. The HT-9 SCW sample exhibits a highly ordered structure of oxide particles in the diffusion layer and in the inner oxide layer. Diffraction analysis shows that as the oxide advances through the metal, spinel develops uniformly from within the metal grains, until the Fe-bcc crystal lattice transforms to the FeCr_2O_4 crystal lattice.

The oxide formed on the HT-9 LBE corroded sample appears to be influenced by the metal structure. In particular, the grain structure of the inner oxide layer is related to the metal lath sub-boundaries of the HT-9 LBE corroded sample, in forming “packets” of oxide grains within the former austenite grains. In contrast, the oxide layer formed on the model alloy (91 wt% Fe and 9 wt% Cr) exhibits no preferred orientation and the metal grain structure appears to have no influence on the advancement of the oxide. Since it appears that the oxide layer formed on the model alloy is not protective, while the oxide layer formed on the HT-9 corroded sample appears to be protective, it is apparent that the additional minor alloying elements of HT-9 have improved the corrosion behavior of the oxide layer.

TABLE OF CONTENTS

LIST OF FIGURES	vii
LIST OF TABLES	xii
ACKNOWLEDGEMENTS	xiii
Chapter 1 Introduction and Background.....	1
Chapter 2 Experimental Methods and Sample Preparation	7
2.1 Alloy Materials	7
2.1.1 Alloy Chemical Composition and Fabrication	7
2.1.2 SCW and LBE Corrosion Loops	9
2.2 Sample Preparation.....	11
2.2.1 Cross-Sectional Sample Preparation	11
2.2.2 Scanning Electron Microscopy Preparation	13
2.2.3 Focused Ion Beam Sample Preparation.....	13
2.2.3.1 Focused Ion Beam Artifacts	18
2.2.4 Transmission Electron Microscopy	19
2.2.5 Microbeam Synchrotron X-ray Fluorescence and Diffraction	20
Chapter 3 Experimental Results.....	23
3.1 Analysis of oxide layers formed after exposure to SCW	23
3.1.1 9Cr ODS Sample Analysis	25
3.1.1.1 Analysis of oxide layer formed on 9Cr ODS after 4 weeks of exposure to 600°C SCW	25
3.1.1.2 Analysis of oxide layer formed on 9Cr ODS, after 2 weeks exposure to 600°C SCW	43
3.1.2 Analysis of oxide layer formed on HT-9 after 3 weeks exposure to 500°C SCW	51
3.1.3 SCW Alloy Corrosion Summary.....	64
3.2 Analysis of oxide layers formed after exposure to LBE.....	65
3.2.1 Analysis of oxide layer formed on Alloy #3 after 4 weeks exposure to 500°C LBE	66
3.2.2 Analysis of oxide layer formed on HT-9 after 4 weeks exposure to 500°C LBE	79
3.2.3 LBE Alloy Corrosion Summary	87
Chapter 4 Summary and Conclusions.....	88
Bibliography	92

Appendix Power Diffraction Files	94
--	----

LIST OF FIGURES

Figure 1.1 : Ternary phase diagram of Fe, Cr, and O system calculated at 500°C and 0.1 MPa by Tan et al. [5].	5
Figure 2.1 : Layout of the heart of the UW-SCW loop [12].	10
Figure 2.2 : Schematic of LANL DELTA Loop [10].	11
Figure 2.3 : Depiction of sample mounting preparation for use in the synchrotron [15].	12
Figure 2.4 : Illustration of trench-milling a sample in the FIB.	16
Figure 2.5 : Trench-milled samples from 3 mm cross-sectional disks.	18
Figure 2.6 : Beam characteristics of the APS [15].	21
Figure 2.7 : Schematic of microbeam synchrotron x-ray fluorescence and diffraction [15].	22
Figure 3.1 : Optical images of SCW corroded (a) HT-9 3 weeks at 500°C, (b) and 9Cr ODS 2 weeks, & (c) 9Cr ODS 4 weeks both at 600°C.	24
Figure 3.2 : SEM secondary electron image of 9Cr ODS, after 4 weeks exposure to 600°C SCW showing the structure of the oxide layer.	26
Figure 3.3 : TEM bright field image of inner oxide/outer oxide interface from 9Cr ODS, 4 week sample.	28
Figure 3.4 : TEM bright field image of diffusion layer/inner oxide interface from 9Cr ODS, 4 week sample.	29
Figure 3.5 : TEM bright field image of the first metal/diffusion layer interface specimen of 9Cr ODS, 4 week sample.	30
Figure 3.6 : TEM bright field image of the second metal/diffusion layer interface specimen of 9Cr ODS, 4 weeks sample.	31
Figure 3.7 : TEM bright field images and corresponding diffraction patterns of (a) Fe ₃ O ₄ with zone axis [011], taken from an outer oxide grain and (b) FeCr ₂ O ₄ with zone axis [001], taken from the inner oxide of 9Cr ODS, 4 week sample. ...	33

Figure 3.8: JEMS simulated diffraction pattern, TEM diffraction pattern, and corresponding bright field image of Cr_2O_3 , with a zone axis of [210], from diffusion layer oxide front of 9Cr ODS, 4 week sample.	35
Figure 3.9: JEMS simulated diffraction pattern, TEM diffraction pattern, and corresponding bright field image of Cr_2O_3 , with a zone axis of [241], from diffusion layer oxide front of 9Cr ODS, 4 week sample.	36
Figure 3.10: TEM bright field images and corresponding diffraction patterns of FeCr_2O_4 , (a) with a zone axis of [013] and (b) with a zone axis of [112], within the diffusion layer of 9Cr ODS, 4 week sample.	37
Figure 3.11: EDS overlay of spectra from inner oxide layer (black) and outer oxide layer (red).	38
Figure 3.12: EDS spectra of reference metal and region determined to be Cr_2O_3 in diffusion layer of 9Cr ODS, 4 week sample.	39
Figure 3.13: Low magnification EELS maps of iron, oxygen, and chromium for the diffusion layer/metal interface sample of 9Cr ODS, 4 week sample.	40
Figure 3.14: EELS maps of iron, oxygen, and chromium for the diffusion layer/metal interface of 9Cr ODS, 4 week sample.	41
Figure 3.15: Microbeam synchrotron fluorescence of counts associated with iron and chromium $\text{K}_{\alpha 1}$ peaks versus distance in the oxide layer for 9Cr ODS, 4 week sample.	42
Figure 3.16: SEM backscatter electron image of the oxide sub-layers on 9Cr ODS, after 2 week exposure to 600°C SCW.	44
Figure 3.17: TEM bright field image of diffusion layer at the diffusion layer/metal interface of 9Cr ODS, 2 week sample. Arrows indicate the metal/diffusion layer interface.	45
Figure 3.18: EELS maps of iron, oxygen, and chromium for the diffusion layer of 9Cr ODS, 2 week sample.	46
Figure 3.19: TEM bright field image and corresponding diffraction pattern of Fe-bcc with a zone axis of [001] within the diffusion layer of 9Cr ODS, 2 week sample.	47
Figure 3.20: TEM bright field image and corresponding diffraction pattern of FeCr_2O_4 , with zone axis of [101], within the diffusion layer of 9Cr ODS, 2 week sample.	48

Figure 3.21: EDS spectrum of FeCr_2O_4 grain within the diffusion layer of the 9Cr ODS, 2 week sample.....	49
Figure 3.22: Microbeam synchrotron fluorescence of counts associated with iron and chromium $\text{K}_{\alpha 1}$ in 9Cr ODS, 2 week sample.....	50
Figure 3.23: SEM backscatter electron image of HT-9, after 3 weeks exposure to 500°C SCW, showing the different oxide sub-layers.	52
Figure 3.24: TEM bright field image of all three oxide sub-layers on HT-9, after 3 weeks exposure to 500°C SCW. Artifacts are shown in boxes.	52
Figure 3.25: TEM bright field image of the inner oxide layer of HT-9 after 3 weeks exposure to 500°C SCW.	54
Figure 3.26: TEM bright field image and magnification of highly-ordered Fe-bcc and FeCr_2O_4 within the diffusion layer of HT-9, after 3 weeks exposure to 500°C SCW.....	55
Figure 3.27: TEM dark field analysis of Fe-bcc diffraction spot from diffusion layer of HT-9, after 3 weeks exposure to 500°C SCW. (Note: This diffraction pattern is indexed in Figure 3.30.).....	56
Figure 3.28: TEM diffraction pattern and corresponding bright field image of Fe_3O_4 , with a zone axis of $[-111]$, from outer oxide layer of HT-9, after 3 weeks exposure to 500°C SCW.	57
Figure 3.29: TEM (a) bright field image of highly-ordered FeCr_2O_4 grains within the inner oxide of HT-9, after 3 weeks exposure to 500°C SCW, (b) corresponding diffraction pattern, and (c) JEMS indexing of the experimental diffraction pattern.	58
Figure 3.30: TEM (a) bright field image of highly-ordered Fe-bcc and FeCr_2O_4 within the diffusion layer of HT-9, after 3 weeks exposure to 500°C SCW, (b) corresponding diffraction pattern with zone axis $[001]$ for Fe-bcc and with zone axes of $[011]$ and $[101]$ for FeCr_2O_4 , and (c) JEMS indexing of the experimental diffraction pattern..	59
Figure 3.31: TEM diffraction pattern and corresponding bright field image of highly-ordered FeCr_2O_4 , with zone axes $[111]$ and $[112]$, and Fe-bcc within the diffusion layer of HT-9, after 3 weeks exposure to 500°C SCW. This diffraction pattern is exactly the same as that shown in Figure 3.29.....	60

Figure 3.32: TEM EDS of the ratios of oxygen/iron and chromium/iron $K_{\alpha 1}$ spectral lines from diffusion layer to inner oxide of HT-9, after 3 weeks exposure to 500°C SCW.	62
Figure 3.33: Location of EDS line scan data presented in Figure 3.32.	62
Figure 3.34: Microbeam synchrotron fluorescence of counts associated with iron and chromium $K_{\alpha 1}$ in HT-9, after 3 weeks exposure to 500°C SCW.	63
Figure 3.35: Optical images of LBE corroded (a) Alloy #3 and (b) HT-9.	66
Figure 3.36: (a) SEM backscatter electron image of Alloy #3 showing the oxide layers and (b) FIB image of porous inner oxide/metal interface during sample preparation.	66
Figure 3.37: TEM bright field image of entire Alloy #3 specimen.	67
Figure 3.38: TEM bright field image of large equiaxed grains along outer oxide/inner oxide interface of Alloy #3. (Note: The beam stop is present in this image.)	68
Figure 3.39: TEM bright field image of Alloy #3 inner oxide grain structure.	69
Figure 3.40: TEM diffraction patterns and corresponding bright field images of (a) a Fe_3O_4 grain with zone axis $[-112]$ within the outer oxide layer, (b) an unindexed pattern from a region at the outer oxide/inner oxide interface, and (c) a $FeCr_2O_4$ grain with zone axis $[011]$ within inner oxide layer of Alloy #3.	71
Figure 3.41: TEM bright field image and corresponding diffraction pattern of bismuth grain with zone axis $[101]$	72
Figure 3.42: TEM EDS of bismuth and lead $L_{\alpha 1}$ spectral emission lines throughout Alloy #3 from metal/diffusion layer interface with emphasis on (a) Bi/Fe ratio and (b) Pb/Fe ratio.	73
Figure 3.43: EDS (a) locations and (b) spectra overlay of box-like surface structures and a reference point within the outer oxide layer for Alloy #3.	74
Figure 3.44: EDS locations of reference inner oxide (3) and bismuth grains (2 & 20).	75
Figure 3.45: EDS spectra of bismuth grains (black & green) and reference inner oxide spectrum (red).	76

Figure 3.46: Microbeam synchrotron fluorescence of counts associated with iron and chromium $K_{\alpha 1}$ for Alloy #3.....	77
Figure 3.47: Microbeam synchrotron fluorescence of counts associated with copper $K_{\alpha 1}$ for Alloy #3.....	78
Figure 3.48: SEM backscatter electron image of HT-9, after 4 weeks exposure to 500°C LBE.....	79
Figure 3.49: TEM bright field image of entire HT-9, after 4 weeks exposure to 500°C LBE and sketch of $FeCr_2O_4$ grains (region “A”) within the inner oxide layer with pores and small grains in between the grains (depicted as dashed lines).	81
Figure 3.50: TEM diffraction patterns and corresponding bright field images from HT-9, after 4 weeks exposure to 500°C LBE, of (a) a Fe_3O_4 grain within the outer oxide layer, with a zone axis of $[-112]$ and (b) a $FeCr_2O_4$ grain within the inner oxide, with a zone axis of $[-111]$ showing a highly-structured region within the inner oxide layer.	83
Figure 3.51: EDS spectrum of lead grain in outer oxide of HT-9, after 4 weeks exposure to 500°C LBE.	85
Figure 3.52: Microbeam synchrotron fluorescence of counts associated with iron and chromium $K_{\alpha 1}$ for HT-9, after 4 weeks exposure to 500°C LBE.....	86

LIST OF TABLES

Table 1.1: List of phases corresponding to ternary diagram in Figure 1.1.	5
Table 2.1: As-received chemical compositions of alloys examined in this study listed in wt% with iron balance.	8
Table 2.2: Corrosion conditions of as-received alloys for this study.	9
Table 2.3: PDF file numbers of the phases found in this study.	20
Table 3.1: List of phases found in the various layers of 9Cr ODS.	43
Table 3.2: List of phases found within the various layer of HT-9 500°C, 3 weeks SCW corroded sample.	64
Table 3.3: List of phases found within the oxide layers of Alloy #3.	78
Table 3.4: List of phases found within the various layer of HT-9 500°C, 4 weeks LBE corroded.	87
Table A.1: ICDD #: 01-1262, Body-centered cubic, Fe, $a=2.857 \text{ \AA}$	94
Table A.2: ICDD #: 19-0629, Face-centered cubic Fe_3O_4 , $a=8.396 \text{ \AA}$	95
Table A.3: ICDD #: 34-0140, Face-centered cubic FeCr_2O_4 , $a=8.3790 \text{ \AA}$	96
Table A.4: ICDD #: 38-1479, Rhombohedral Cr_2O_3 , $a=4.95876 \text{ \AA}$, $c=13.5942 \text{ \AA}$	97
Table A.5: ICDD #: 44-1246, Rhombohedral Bi, $a=4.547 \text{ \AA}$, $c=11.86 \text{ \AA}$	98

ACKNOWLEDGEMENTS

I would like to thank my advisor, Arthur Motta, for giving me the opportunity to work with him on a project in which I have gained a multitude of experience, which will be carried with me indefinitely, and for his nonpareil guidance during my graduate studies. I would also like to thank Elizabeth Dickey and Lawrence Hochreiter for providing stimulating academic environments within their classrooms, and especially for their comments on this thesis work.

Thanks to Robert Comstock for his help with sample preparation for the APS. Much thanks to Trevor Clark, Joe Kulick, and Josh Maier for all of their help with the FIB and the TEM. After many months and numerous speed bumps, they were still there to help me anytime I needed it. Thanks to John Cantolina and Mark Angelone for their assistance with the SEM.

I would additionally like to thank Jeremy Bischoff and Jamie Kunkle for their collaboration on this project. The discussions I had with them about their work helped me to better understand the findings within my own work.

I would also like to thank all the members of the nuclear material group past and present, in particular, those who became students before me and who were kind enough to impart advice from their own experience. Thanks to all of my friends, who allowed our relationships to grow despite the time and distance between us.

Finally, I would like to thank my family, in particular, my parents. Their love, their support, and their guidance on all aspects of life have helped to shape the person I have become...

“If you raise your children to feel that they can accomplish any goal or task they decide upon, you will have succeeded as a parent and you will have given your children the greatest of all blessings.” ~Brian Tracy

Chapter 1

Introduction and Background

An estimated increase of the world's population by more than fifty percent by 2050 and an ever increasing awareness of global climate change will put huge demands on future energy production. The desire to provide sufficient energy for our future needs has brought together the Generation-IV International Forum, which aims to develop the next generation of nuclear reactors through shared technology and research. These new nuclear reactors, Generation-IV reactors, to be deployable as early 2030, are intended to provide significant improvements in four specific areas: proliferation resistance, enhanced safety, waste minimization, and increased economic viability. In order to meet waste minimization and enhanced economics, the efficiencies of Gen-IV reactors will need to be increased over current reactors. This will be accomplished mainly through increased temperatures, pressures, and residence time within the reactor core compared to current reactor designs. These higher temperatures imply more corrosive environments.[1]

Current reactor designs use zirconium alloys as nuclear fuel cladding because zirconium has a much lower thermal neutron absorption cross section than iron. The neutron absorption cross section is a measure of the ability of a nucleus to absorb neutrons. The trade off between neutron economy and corrosion resistance allows for zirconium alloys to be more desirable in current reactor designs. However, at the higher temperatures envisaged for Gen-IV reactors, zirconium alloys are not feasible because of

their low creep strength and high corrosion rate, which leads to the choices of various steel alloys.

Out of the six Gen-IV designs, the two that were considered for this study are the Lead-Cooled Fast Reactor (LFR) and the Supercritical-Water-Cooled Reactor (SCWR). The LFR is designed to have core outlet temperatures up to 550°C at near atmospheric pressure using lead-bismuth eutectic (LBE) as its coolant, while the SCWR is designed to have core outlet temperatures up to 550°C with a pressure of 25 MPa using supercritical water as its coolant [1].

Potential candidate fuel cladding materials for these reactors are mentioned in “A Technology Roadmap for Generation IV Nuclear Energy Systems” [1]. For the LFR, it is suggested that standard ferritic steels would be sufficient to withstand corrosion imposed by the maximum core outlet temperature. The general requirements imposed for the fuel cladding of the LFR are compatibility with Pb-Bi coolant and a radiation damage resistance in a fast neutron environment for 15-20 years [1]. For the SCWR, no alloy has been chosen as the forerunner for the SCWR, since candidate fuel cladding alloys have not been extensively studied in the environment they would be exposed to within the SCWR. Potential candidate alloys include austenitic stainless steels, solid solution and precipitation-hardened alloys, ferritic-martensitic alloys, and oxide dispersion-strengthened alloys [1]. The focus of this study is on the corrosion behavior of the oxides developed on unirradiated fuel cladding alloy candidates. The alloys examined in this study include an oxide dispersion-strengthened alloy (9Cr ODS) exposed to the SCWR environment, a model alloy consisting of only iron and chromium exposed to the LFR environment, and a ferritic-martensitic steel (HT-9) exposed to each environment.

Uniform corrosion is a concern, and it is believed that the microstructure of an alloy has a significant effect on its corrosion behavior. Varying concentrations of elements among similar alloys can produce drastically different corrosion behavior. The project, of which this thesis is a part, is focused on studying how alloy microstructures and compositions affect corrosion behavior. Previous work has been done on zirconium alloys to relate alloy microstructure to corrosion behavior [2-4]. The hypothesis is that the alloy microstructure affects corrosion behavior by influencing the structure of the protective oxide layer. In order to compare the corrosion behavior of two or more similar alloys, a complete understanding of an individual alloy needs to be attained. This thesis focuses on the examination of the oxide layers of several steel alloys: at various stages of corrosion for the SCWR, various (similar) compositions within each corrosion medium, and finally between two alloys from the same family for both corrosion mediums.

To investigate the oxides formed on the steel alloys studied in this project, two specialized and complementary techniques were employed: Transmission Electron Microscopy (TEM) and microbeam x-ray fluorescence and diffraction using Synchrotron Radiation. The focus of this thesis will be on TEM. The TEM samples were fabricated with the aid of a focused ion beam (FIB). The FIB allows the user to fabricate TEM samples with increased ease, reproducibility, and larger viewing areas than conventional techniques.

Previous work performed on these alloys is reviewed in the following. The information from the articles mentioned below consists of reviews of two of the alloys presented in this study as well as a review of an article providing methodology of the thermodynamics of oxide formation.

Steel alloys are comprised mostly of iron and chromium, but may include minor alloying elements which are usually limited to less than 2 wt% bal. iron each. During corrosion in supercritical water, the phases that are most likely to be found will be composed of a mixture of iron, chromium, and oxygen. The thermodynamics of oxide formation on chromium enriched steels has been explored by Tan et al. on HCM12A [5], which consists mainly of iron and ~11 wt% Cr bal. iron with additional minor alloying elements. The expected phases for Fe-Cr-O systems were found by using the calculated ternary diagram of Fe-Cr-O at 500°C and 0.1 MPa. Tan showed that even though the samples were exposed to 500°C and 25 MPa, the differences between the nominal and adjusted ternary diagrams are negligible. The ternary diagram calculated in their study is shown in Figure 1.1 and the phases corresponding to this diagram are listed in Table 1.1. The white areas on the ternary diagram depict the location of an individual phase, which is listed next to it. The shaded areas represent regions in which more than one phase is possible, composed of the phases adjacent to each of their borders. For example, the largest shaded area could have either Fe-bcc or Cr-bcc, but should not have the other listed phases. This ternary diagram provides a base for phase identification of grains within the examined oxides, but it is not exhaustive.

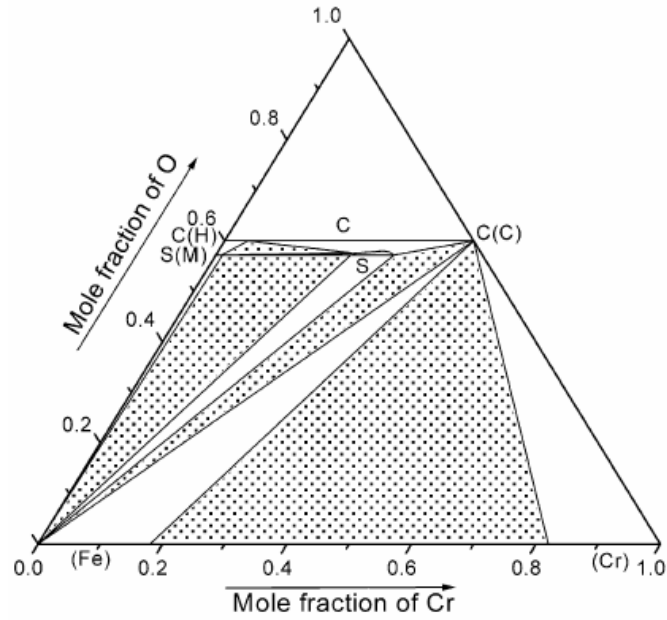


Figure 1.1: Ternary phase diagram of Fe, Cr, and O system calculated at 500°C and 0.1 MPa by Tan et al. [5].

Table 1.1: List of phases corresponding to ternary diagram in Figure 1.1.

Denotation	Phase
C	$(\text{Fe,Cr})_2\text{O}_3$ (Corundum)
C(H)	Fe_2O_3 (Hematite)
C(C)	Cr_2O_3 (Chromite)
S	$\text{Fe}_{(1-x)}\text{Cr}_{(2-x)}\text{O}_4$, (Spinel) $0 \leq x \leq 0.5$
S(M)	Fe_3O_4 (Magnetite)
(Fe-bcc)	Iron-rich solid solution
(Cr-bcc)	Chromium-rich solid solution

A study of the HT-9 alloy corroded in SCW has previously been performed on the same sample by Ren et al. [6]. Their study compared the corrosion rates of HT-9 at 500°C

SCW with dissolved oxygen contents of 25 ppb and 2 ppm. Another HT-9 sample was surface modified by implanting oxygen, then exposed to 500°C SCW with dissolved oxygen content of 25 ppb to study the effects of oxygen implantation. The findings of their study, as they pertain to this study, were that the examination of the HT-9 sample indicated the presence of an Fe-rich magnetite outer oxide and a Cr-rich inner oxide that was a mixture of ferrite and spinel phases [6].

A study has already been performed on the 9Cr ODS sample by Chen et al. [7-8]. Their study compared the 9Cr ODS alloy to non-oxygen dispersion strengthened steels, as well a focus on the 9Cr ODS at 500°C and 600°C. Their study also included a weight gain study of 9Cr ODS at varying corrosion stages of 2, 4, and 6 weeks. In the case of the temperature and stage of corrosion of which was examined in this study, they observed an outer oxide magnetite layer of Fe_3O_4 , an inner oxide spinel layer of $(\text{Fe,Cr})_3\text{O}_4$, and an innermost internal oxidation layer. Although these oxide sub-layers were found in both of the oxides formed on the 500°C and 600°C samples, the 600°C sample had an additional ~1 μm thick, dense and continuous Cr-rich oxide layer which developed along the interface between the internal oxidation layer and the base metal [8]. The analysis presented in Chapter 3 includes a detailed comparison of the 9Cr ODS at different stages (2 and 4 weeks) of oxide development, in particular, the formation of the internal oxidation layer which is believed to be the location of the corrosion limiting process in the 9Cr ODS alloy.

The following chapter details the alloy fabrication and corrosion processes as well as the specimen preparation for examination.

Chapter 2

Experimental Methods and Sample Preparation

2.1 Alloy Materials

The alloys 9Cr ODS and HT-9 were supplied by The University of Wisconsin and their fabrication as well as their exposure in the SCW corrosion loop are discussed in the following sections. The alloys Alloy #3 and HT-9 were supplied by Los Alamos National Laboratory and their fabrication as well as their exposure in the LBE corrosion loop are discussed in the following sections.

2.1.1 Alloy Chemical Composition and Fabrication

The pre-corrosion compositions for the 9Cr ODS, Alloy #3, and both HT-9 samples are listed in Table 2.1 as wt% with iron balance.

The SCW corroded samples were fabricated in Japan and then sent to the University of Wisconsin to be put into the SCW corrosion loop. The 9Cr ODS samples were normalized at 1050°C for one hour, air cooled, then tempered at 770°C for two hours before a final air cooling. Further details of their fabrication can be found elsewhere [9]. The HT-9 SCW corroded sample was normalized at 1040°C for one hour, air cooled, then tempered at 740°C before the final air cooling.

The LBE corroded samples Alloy #3 and HT-9 were fabricated by MIT and Sandvik Steel, respectively, and then sent to LANL to be put into the DELTA Loop.

Alloy #3 was made from iron and chromium powder that was mixed together and ball milled. Next, the material was pressed into rods for a hot isostatic pressing consolidation process. After LANL received the alloy, the material was rolled into sheets and annealed so that a ferritic structure would remain. HT-9 was produced by melting the alloying components and casting in a block. After casting, the material was forged and hot rolled at 1050°C for one hour, air cooled, then annealed at 750°C for two hours, and cooled within the furnace.[10]

Table 2.1: As-received chemical compositions of alloys examined in this study listed in wt% with iron balance.

	9Cr ODS	HT-9 (SCW)	Alloy #3	HT-9 (LBE)
Cr	8.6	11.94	9	11.5
Si	0.048	0.30	-	0.4
Ni	0.06	0.62	-	0.5
Mn	0.05	0.69	-	0.6
C	0.14	0.21	-	0.1
O	0.14	-	-	-
P	<0.05	0.013	-	-
S	0.003	0.005	-	-
Ti	0.21	<0.01	-	-
Y	0.28	-	-	-
W	2	0.48	-	-
N	-	0.005	-	-
Al	-	<0.01	-	-
V	-	0.3	-	-
Co	-	0.03	-	-
Cu	-	0.02	-	-
Mo	-	1.03	-	-

2.1.2 SCW and LBE Corrosion Loops

The corrosion tests on these samples had been previously performed by The University of Wisconsin and Los Alamos National Laboratory.

Table 2.2: Corrosion conditions of as-received alloys for this study.

Alloy	Temperature (°C)	Time (weeks)	Corrosion Medium	Pressure (MPa)
Alloy #3	500	4	LBE	Atmospheric
HT-9	500	4	LBE	Atmospheric
	500	3	SCW	25
9Cr	600	4	SCW	25
ODS	600	2	SCW	25

The 9Cr ODS samples and an HT-9 sample were cut into test samples with dimensions 31.8 mm × 12.7 mm × 0.5 mm. Both samples were corroded at UW in a natural circulation loop with supercritical water at the conditions given in Table 2.2. The UW-SCW loop (Figure 2.1) is made of Inconel 625 and has a flow velocity of 1 m/s and a mass flow rate of 0.4 kg/s. The test samples are inserted into the section between the green flanges (Figure 2.1) on the left side of the loop. The heating manifold is located on the pipes at the bottom and left of the image, while the cooling manifold is located on the pipe at the top of the image. The cooling manifold is necessary to prevent the pump from being exposed to temperatures in excess of its design criteria. Further details of the UW-SCW corrosion loop can be found elsewhere [11].

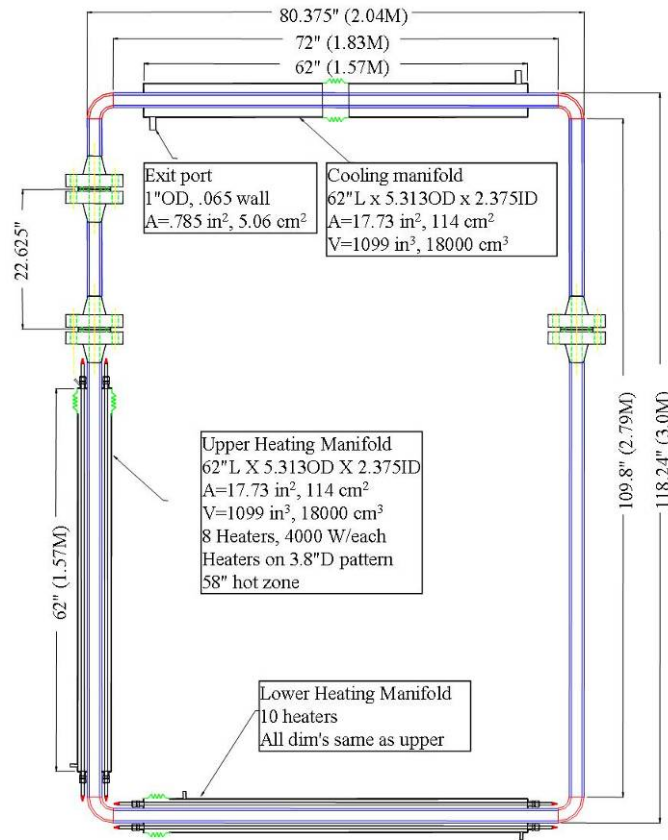


Figure 2.1: Layout of the heart of the UW-SCW loop [12].

The Alloy #3 sample and HT-9 sample were fabricated into coupons with dimensions of 35-mm \times 8-mm \times 1-mm. Both samples were corroded at LANL in the DELTA Loop in lead-bismuth eutectic (LBE) at the conditions given in Table 2.2. Lead-bismuth is eutectic at 44.8 wt% lead, 55.2% bismuth, and 123.5 °C as provided by the IPPE [13]. The test section in which the samples were inserted is seen on the right side of the diagram depicted in Figure 2.2. The details of the DELTA Loop can be found elsewhere [14].

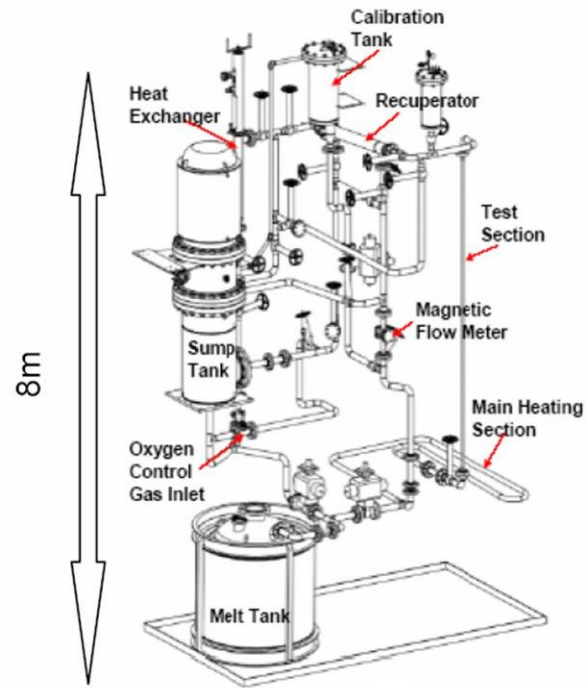


Figure 2.2: Schematic of LANL DELTA Loop [10].

2.2 Sample Preparation

All of the instruments used in this study are located at The Pennsylvania State University's Materials Research Institute (MRI).

2.2.1 Cross-Sectional Sample Preparation

The oxide layer cross-sectional samples were prepared for use first in the synchrotron, with the intention of using them in the TEM afterwards. The process for synchrotron sample preparation is depicted in Figure 2.3. The samples were prepared for

the synchrotron by first (a) cutting slivers from the coupon corrosion samples and (b) grinding the samples on one side to a thickness of approximately 0.35-mm. Next, the samples were (c) submerged in epoxy and fit into slotted molybdenum rods, which are 2-mm in diameter. They were then (d) put into copper rods of 3-mm outside diameter after which the epoxy was allowed to cure for 15-20 minutes at 80°C. After the rods were cured, they were (e) cut into disks of approximately 1-mm thickness and polished on one side through several levels of polishing paper before finally being polished with a 0.1 μ m diamond paste.

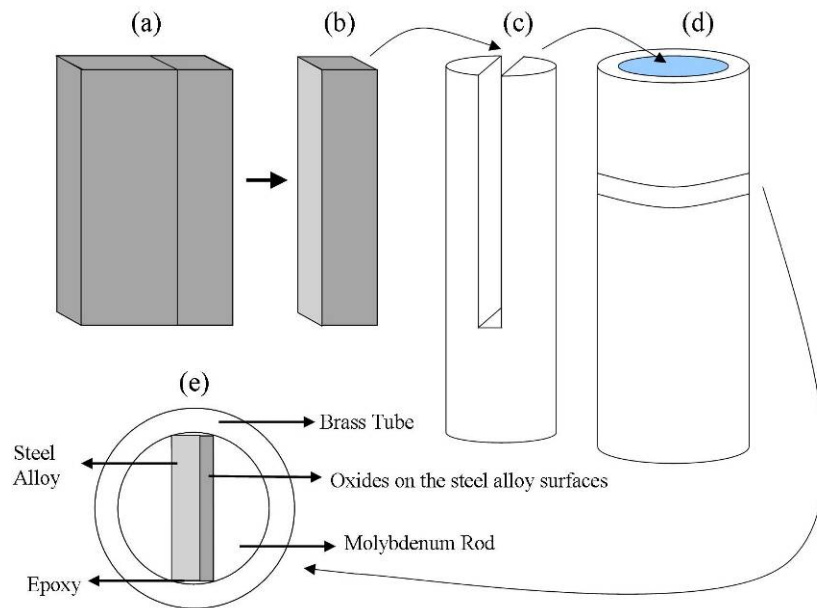


Figure 2.3: Depiction of sample mounting preparation for use in the synchrotron [15].

2.2.2 Scanning Electron Microscopy Preparation

The Scanning Electron Microscope used in this study was a FEI Quanta 200 ESEM. Sample preparation for the scanning electron microscope (SEM) was simple but great care had to be taken to prevent damage to the oxide so the sample could be removed from the sample holder at a later time.

The 3-mm discs were mounted to standard FEI SEM stubs with two thin strips of carbon tape on either side that were running parallel to (but not in contact with) the oxide layer. The strips of bulk substrates were placed with the less desired oxide side face down and onto carbon tape. Since only one side of the bulk substrate is needed for disc fabrication, special care only needed to be taken for the chosen side of the substrate. After the samples were attached to the stubs, liquid silver was applied to provide a ground for the electrons from the SEM to prevent local charging on the sample during examination. This was done very carefully by twisting one corner of a Kim-Wipe into a fine point, dipping the point into the liquid silver, and providing a very thin continuous line of silver paint from the oxidized alloy to the FEI SEM stub.

2.2.3 Focused Ion Beam Sample Preparation

The TEM samples were prepared using a Focused Ion Beam (FIB). The model is a FEI Company Quanta 200 3D Dual Beam FIB. The FIB was used instead of traditional mechanical thinning with ion milling, primarily because the FIB allows for the production of site-specific specimens, a greater viewing area, and a greater degree of reproducibility. This means that if the oxide layer to be examined is small enough

(~10 μm) a specimen can be produced that will include electron transparency of the entire oxide layer, the interface between the oxide and the metal, as well as part of the metal layer with lateral electron transparency up to 10 microns or more. Preparing samples with the FIB also allowed us to have a much larger viewing area than previous methods, ensuring consistency throughout the specimen.

The FIB uses Ga^+ ions to mill samples as well as to deposit a layer of tungsten or platinum to protect the sample during milling and also to use the tungsten/platinum deposition to attach the milled sample to a sample holder. The Ga^+ ions are extracted from the source much in the same way as the SEM extracts electrons from its source.

There are many different methods for preparing samples using the FIB, all of which are very useful depending upon the type of samples and the examination to be performed. The method used to prepare the samples in this study has been termed the FIB *in-situ* lift-out (INLO) method by Gianuzzi and Stevie [16] and was chosen for convenience, reproducibility, and versatility.

The samples were prepared in a manner similar to that of the *ex-situ* lift-out (EXLO) technique in which the sample is trench-milled from the bulk and lifted out using a microprobe. The benefit of using the lift-out technique is that it requires no initial specimen preparation. The EXLO method thins the specimen first then removes it; whereas, the INLO method employed in this study removes the specimen first then thins it.

Removing the sample and attaching it to a sample holder with tungsten before thinning allows for the sample to relieve itself of stress during thinning as well as to have a heat sink during TEM examination. This method also has the advantage of full range of

tilt during examination in the TEM and the sample can be returned to the FIB for additional thinning if necessary.

The step-by-step process for producing a TEM specimen using the FIB is as follows:

First, a layer of tungsten or platinum approximately 1 μm wide x 10 μm long x 3 μm high is deposited to the area of interest to protect the sample during the milling and thinning processes. The tungsten is deposited by injecting tungsten hexacarbonyl gas $\text{W}(\text{CO})_6$ into the path of the ion beam, while platinum is deposited by injecting methylcyclopentadienyl platinum trimethyl $(\text{CH}_3)_3(\text{CH}_3\text{C}_5\text{H}_4)\text{Pt}$ [16]. The ion beam decomposes the precursor gas into tungsten/platinum and volatile products at a predetermined current that allows for a net deposition instead of milling. After the protective layer is deposited, the region of interest is milled at an angle of 22° using a horseshoe shape (with an approximate thickness of 1.5 μm), rotated 180° , and milled again to produce a wedge-shaped sample as illustrated in Figure 2.4. It is important that the trench-milling be performed in two steps: an initial step to mill the size and location of the sample, and a secondary step to free the sample from the bulk substrate. The second step is necessary because, as the second horseshoe shape is milled, material from the sample is redeposited to regions that had been milled during the first horseshoe cut. After performing the initial milling with a horseshoe thickness of 1.5 μm , the procedure must be repeated at a reduced thickness of ~ 0.7 μm and with the horseshoe hugging the specimen. This serves to free the specimen from the substrate by allowing the milled material to redeposit on the substrate instead of the specimen.

The sample is trench-milled at the maximum current of 7 nA in order to limit the amount of time spent on this step. The milling time is determined by considering the major elements of the sample and their respective sputtering yields (the number of ejected ions divided by the number of incident ions). The FIB/SEM system has already been preset for silicon and the corrected sample milling depth is calculated by multiplying the desired depth by the ratio of silicon's sputtering yield and the sample's sputtering yield. Because all of the major elements within our samples have higher sputtering yields than silicon, correcting the milling depth ends up reducing the total milling time.

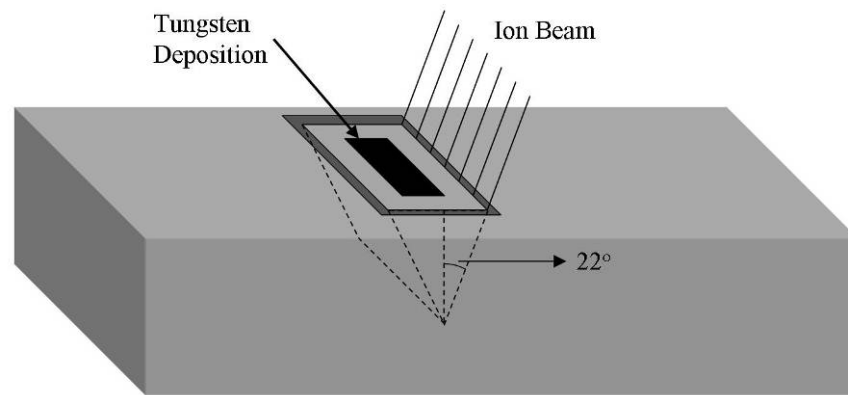


Figure 2.4: Illustration of trench-milling a sample in the FIB

After the sample is milled free from the substrate, it is attached to a tungsten microprobe by tungsten deposition, transferred to a FIB/TEM sample holder where the sample is also attached by tungsten deposition, and then the microprobe is detached from the sample by milling it with the FIB. The sample then undergoes several steps of

thinning in which decreasing currents are used (1nA-30pA) until the sample has reached electron transparency or an approximate thickness of 100 nanometers or less. Electron transparency is determined approximately by dropping the voltage of the SEM to 5 keV, and thinning the sample until it appears bright. At this point of maximum brightness, not only are the electrons reflecting from the viewable surface of the sample back to the SEM detector but the electrons are also reflecting from the back surface of the sample as well. During the final stages of thinning, the sample was rocked back and forth by angles of $\sim 1-3^\circ$ in order to reduce tapering which is caused by a combination of the long tails of the Gaussian shaped ion beam and the sputtering yield dependence on the ion beam incident angle [17]. All milling steps were completed at a voltage of 30 keV.

This same method has been used to produce TEM specimens from the cross-sectional samples prepared for the synchrotron. The cross-sectional samples were used when the oxide layers, which had thickness in excess of 10 microns, proved to be too thick to be prepared from the bulk samples. This allowed the examination of a sample with an oxidation layer of approximately 80 microns by preparing several specimens from the cross-sectional samples as shown in Figure 2.5. From this image, the locations of the TEM samples that were fabricated for this study can be seen. Additionally, there is a specimen in the upper right corner of the image that was irretrievable because the attempt to lift this sample was made before the technique mentioned above was developed.

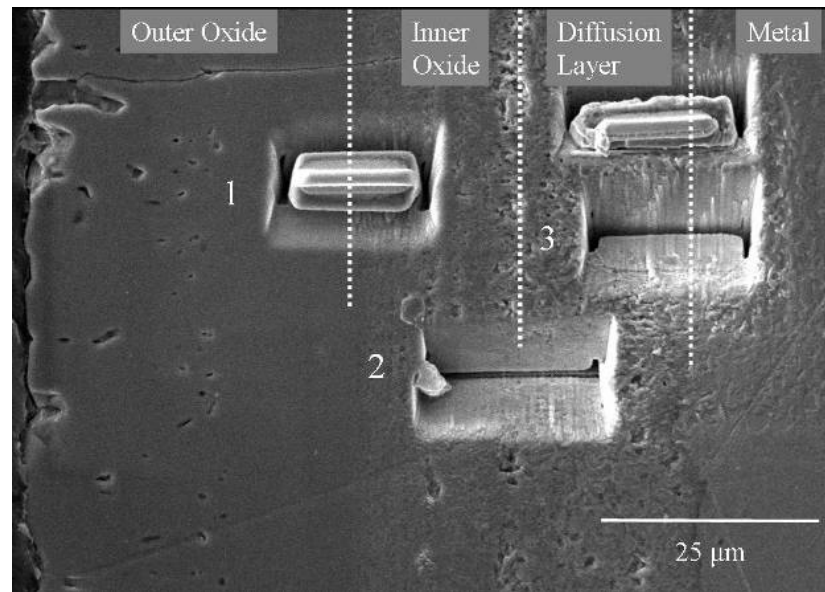


Figure 2.5: Trench-milled samples from 3 mm cross-sectional disks.

2.2.3.1 Focused Ion Beam Artifacts

Almost every method of sample preparation can induce artifacts into the sample and it is important to know and understand the possible artifacts so as not to confuse them with pertinent information taken from the sample.

The “curtain effect” occurs when no protective layer is present, either by not having one initially or by losing it during the milling process [17]. It is characterized by a wavy appearance near the top of the sample which can appear to be rows of columnar grains and is caused by the rastering of the ion beam during milling. Also, ion implantation can occur, in which the incident gallium ions implant themselves within a short distance (order of nanometers) of the milled surface. The amount of implantation is dependent on many factors including the ion energy, the incident angle, and the milling

time. Redeposition occurs at the opposite end of the sample from the incident beam and consists of tungsten, gallium, and sputtered material from the sample undergoing milling. It was found during this study through Energy Dispersive Spectroscopy (EDS) that redeposition can also occur in porous areas of the sample.

Other artifacts may occur, due to differences in user experience and differences between samples (porosity, alloying elements, phases present, etc.). These artifacts occur most often when ion milling is interrupted. Reasons for interruption include, but are not limited to: loss of protective tungsten/platinum (due to milling at too shallow of an angle), bending of the sample (from relief of stresses, particularly if the sample is porous), and uneven milling (improper placement of ion milling regions, overestimation of ion milling depth during final milling, milling across two different mediums, etc.).

2.2.4 Transmission Electron Microscopy

TEM imaging, diffraction analysis, and chemical analysis using Energy Dispersive Spectroscopy spectra were obtained using a Philips 420, 120 keV TEM with a tungsten filament with the aid of a Gatan double tilt sample holder. Electron energy loss spectroscopy was performed on a JEOL, LaB₆ filament based 200 keV TEM, with the aid of a Gatan Imaging Filter (GIF). The energy filtered images were acquired by selecting peaks for each desired element and integrating the intensity under the peaks. It is important to select peaks that do not overlap, in order to provide individual images of each selected element.

Several computer programs were employed for this study in order to aid in making the analysis faster, more precise, and systematic. The program AMT Image Capture Engine 5.42.544 was used to measure d-spacings and the program ImageJ 1.38x was used to extract geometrical information from the TEM diffraction patterns. The program Revolution v1.5.6 by 4pi Analysis, Inc. was used to identify peaks in the EDS spectra and the program Peak-Fit v4 was used to deconvolute the peaks for semi-quantitative chemical analysis. Finally, the program JEMS[15] was employed to assist in indexing TEM diffraction patterns as well as to simulate diffraction patterns for phase identification and zone axis confirmation. The Powder Diffraction Files used in this study are listed in Table 2.3 and the detailed listings are tabulated in the Appendix.

Table 2.3: PDF file numbers of the phases found in this study.

Phase	Crystal Structure	ICDD PDF #
Fe-bcc	bcc	01-1262
Fe ₃ O ₄	fcc	19-0629
FeCr ₂ O ₄	fcc	34-0140
Cr ₂ O ₃	Rhombohedral	38-1479
Bi	Rhombohedral	44-1246

2.2.5 Microbeam Synchrotron X-ray Fluorescence and Diffraction

The Advanced Photon Source (APS) at Argonne National Laboratory outside of Chicago is unique because of the high photon energy and brilliance in which it offers its users as seen from the APS-UA curve in Figure 2.6. The APS is able to focus an x-ray beam down to 2 microns long by 200 nanometers wide.

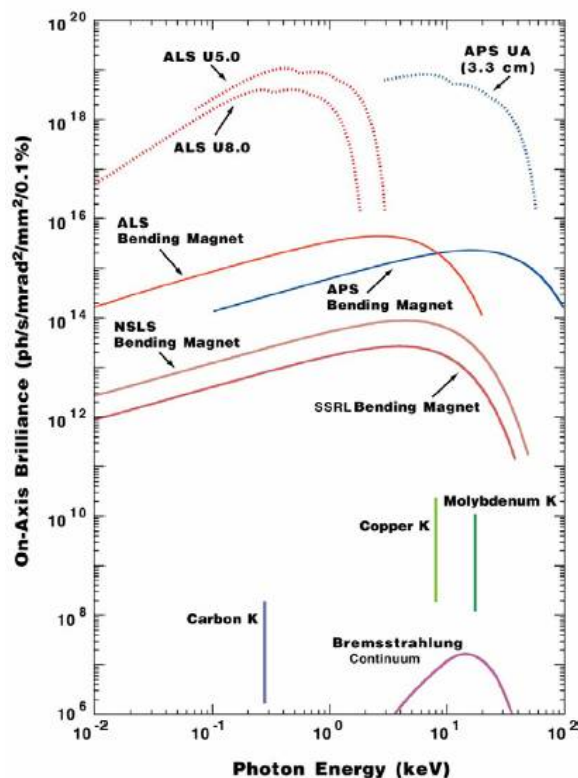


Figure 2.6: Beam characteristics of the APS [15].

The APS was used in this study to extract microbeam x-ray fluorescence and diffraction data. The microbeam fluorescence data provides chemical information, while the diffraction data provides structural information. It can be seen from the diagram in Figure 2.7 that as the microbeam is scanned across the oxide layer the diffraction data is collected by a CCD camera, while the fluorescence data is simultaneously collected by an x-ray detector. The microbeam fluorescence data will be presented in this thesis as a comparison since it compliments the TEM EDS analysis. The microbeam x-ray

diffraction data will be presented in the Master theses of Jeremy Bischoff and Jamie Kunkle, with preliminary findings presented here as further comparison to the overall TEM analysis.

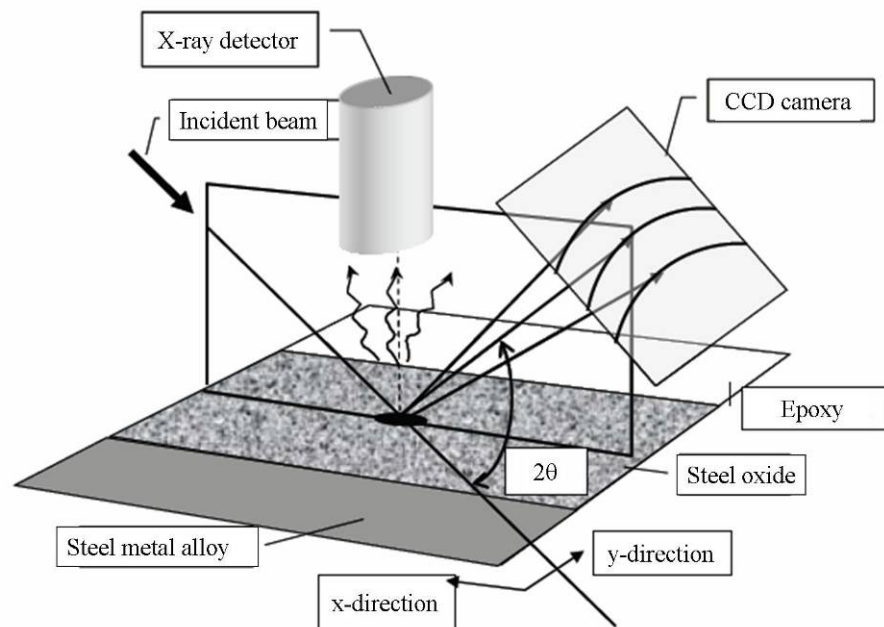


Figure 2.7: Schematic of microbeam synchrotron x-ray fluorescence and diffraction [15].

Chapter 3

Experimental Results

This chapter presents the results of TEM examinations of the oxide layers formed after exposure to supercritical water (SCW) and lead-bismuth eutectic (LBE), with two alloys per environment. The various sub-layers are characterized to determine phases present, grain morphology, and chemical composition.

3.1 Analysis of oxide layers formed after exposure to SCW

The oxide layers formed in SCW selected for analysis were formed on HT-9 and 9Cr ODS. The chemical compositions of the bare metal are listed in Table 2.1. When the chemical composition is compared side-by-side, the alloy 9Cr ODS has seven additional elements (<2 wt%) to those present in HT-9. The comparison of the TEM examination of the oxide layers formed on these two alloys shows how the addition of minor alloying elements (and especially an oxide dispersion) affects the structure of the oxide layer and consequently the corrosion behavior. This is not a direct correlation because of the difference in chromium content as well as metal microstructure. Additionally, 9Cr ODS was examined at 2 weeks and 4 weeks of oxidation in order to study the evolution of the oxide layer, particularly the internal oxidation sub-layer, during this period.

Figure 3.1 shows cross-sectional optical images of oxide layers formed on HT-9 and 9Cr ODS. These images show several sub-layers, referred to here as the outer oxide,

the inner oxide, and the diffusion layer (also called the internal oxidation layer). These sub-layers are especially visible in Figure 3.1 (b) & (c) and will be discussed in more detail later. Figure 3.1 also allows a partial view of the microstructure in the underlying metal. HT-9 exhibits prior austenite grains which contain elongated lath sub-boundaries (see also Figure 3.35), while the 9Cr ODS sample shows equiaxed grains ($\sim 4 \mu\text{m}$) which are small due to the mechanical processing of the alloy.

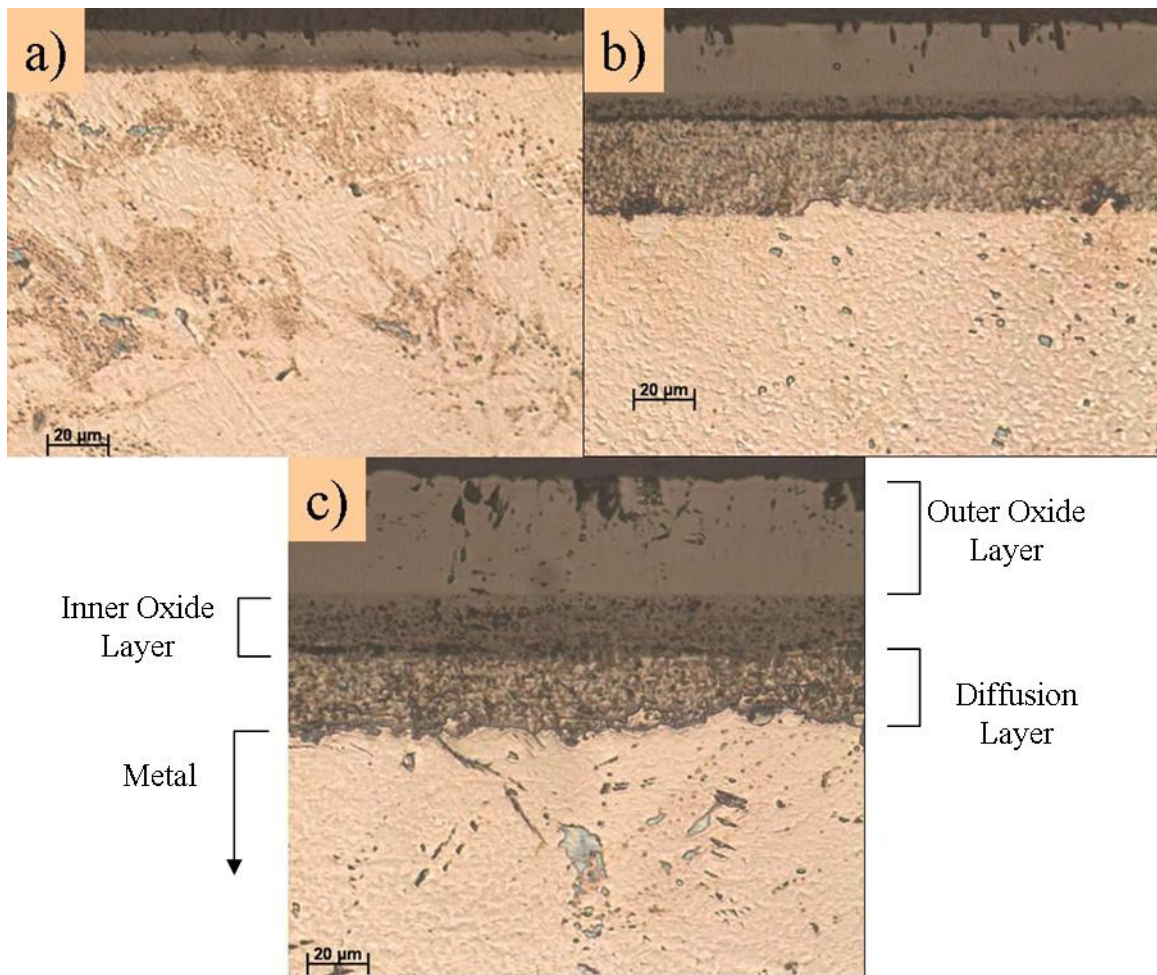


Figure 3.1: Optical images of SCW corroded (a) HT-9 3 weeks at 500°C, (b) and 9Cr ODS 2 weeks, & (c) 9Cr ODS 4 weeks both at 600°C.

3.1.1 9Cr ODS Sample Analysis

Two samples of oxide layers formed on 9Cr ODS (formed after 2 weeks and 4 weeks exposure to SCW) were examined. Because the oxide layer formed on the 9Cr ODS after a 600°C 4 week SCW exposure was thick, four TEM specimens were fabricated to examine specific regions (outer oxide, inner oxide, and the diffusion layer). Special attention was given to the interfaces between these sub-layers; these include the two interfaces from between the three sub-layers and the interface between the diffusion layer and the metal. Since a full examination had been performed on the 4 week sample, only the metal/diffusion layer interface of the 2 week sample was investigated in this study.

3.1.1.1 Analysis of oxide layer formed on 9Cr ODS after 4 weeks of exposure to 600°C SCW

Figure 3.2 shows an SEM image of the 4 week oxide layer formed on 9Cr ODS with approximate TEM sample locations indicated by the white dotted boxes. Three distinct sub-layers are seen: an outer oxide, an inner oxide, and a diffusion layer with thicknesses of 36 μm , 20 μm , and 20 μm , respectively. The TEM samples have been numbered according to the order in which they are presented here with samples 1 and 2 located at the outer oxide/inner oxide interface and the inner oxide/diffusion layer interface, respectively, and with samples 3 and 4 both located at the diffusion layer/metal interface. The oxide layer shows considerable porosity in the sub-layers, with the highest concentration of pores along the inner oxide/diffusion layer interface, but also visible in

the outer part of the outer oxide and in the diffusion layer. The outer region of the outer oxide also appears to be breaking up or spalling, suggesting that weight gain measurements are not that useful in determining corrosion kinetics. The inner oxide layer exhibits “lines” of pores, with some periodicity, the origin of which is not clear. The diffusion layer is considerably more wavy, and shows a dark band at the interface with the metal, which will be discussed later. Both the outer oxide/inner oxide and diffusion layer/metal interfaces of the 4 week sample are clearly distinguishable by a straight line of contrast and a wavy dark band, respectively; whereas, the inner oxide/diffusion layer interface is more difficult to define because of the large amount of porosity located at that interface.

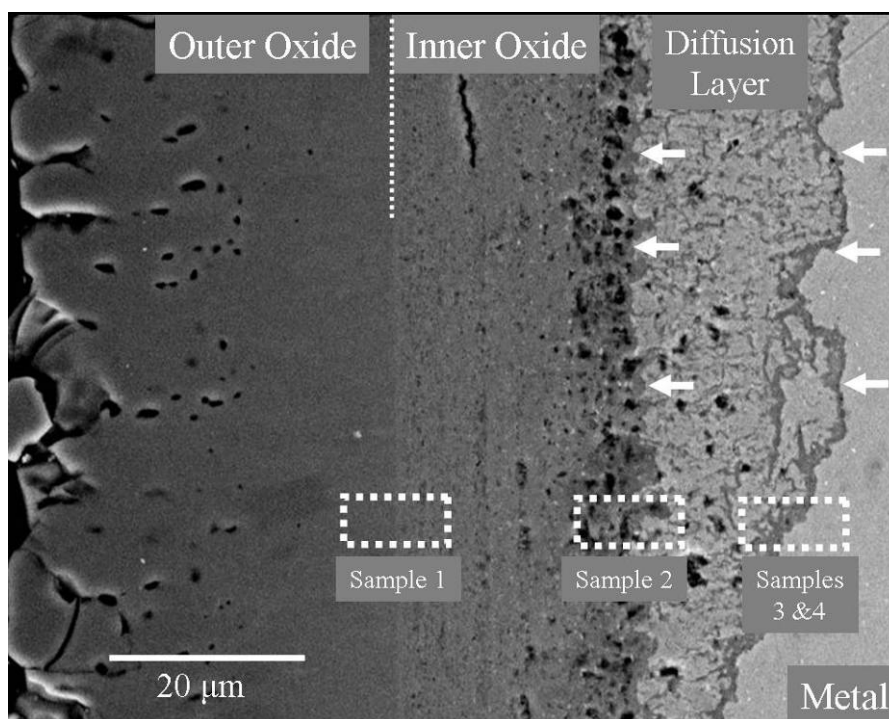


Figure 3.2: SEM secondary electron image of 9Cr ODS, after 4 weeks exposure to 600°C

SCW showing the structure of the oxide layer.

Since the outer oxide layer is thick enough that it would have required ~ 4 TEM specimens for full analysis and is expected to contain a single phase (Fe_3O_4), the first sample was taken from the region of the outer oxide layer within several microns of the outer oxide/inner oxide interface. The TEM bright field image in Figure 3.3 shows the first $\sim 4 \mu\text{m}$ of the outer oxide layer from the inner oxide/outer oxide interface. The outer oxide grains seen in this sample are columnar, measuring up to $3 \mu\text{m}$ long by $2 \mu\text{m}$ wide. Large equiaxed grains within the outer oxide layer along the inner oxide/outer oxide interface can also be seen in Figure 3.3. Since it is generally agreed that the outer oxide/inner oxide interface is the original surface of the metal alloy before corrosion [19], it can be understood that the equiaxed grains, develop from the outer oxide/inner oxide interface and later become the columnar grains seen in the remainder of the outer oxide layer. Figure 3.3 shows pores within the inner oxide layer as well as small equiaxed grains ($<250 \text{ nm}$).

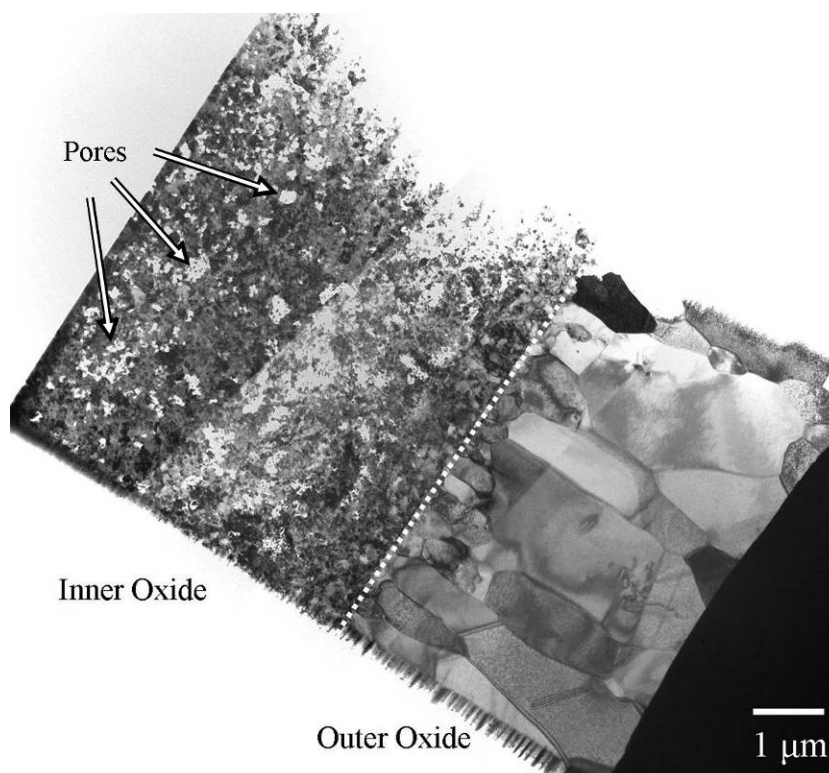


Figure 3.3: TEM bright field image of inner oxide/outer oxide interface from 9Cr ODS, 4 week sample.

Figure 3.4 shows a TEM bright field image of a cross-sectional sample from the diffusion layer/inner oxide sample with the interface indicated by the arrows. EDS analysis could not confirm the exact location of the interface in the TEM bright field image because of the similar chemical and phase composition between the two layers. The location of the interface was determined through examination of the SEM image. Considering the contrast between the inner oxide layer and the diffusion layer as seen in the SEM image, it was decided that the pores along the inner oxide/diffusion layer interface are within the inner oxide layer. Therefore, it has been determined that the inner oxide/diffusion layer interface exists at the metal side of these pores. The pores in the

inner oxide layer are likely condensed vacancies created by the outward diffusion of iron to the outer oxide.

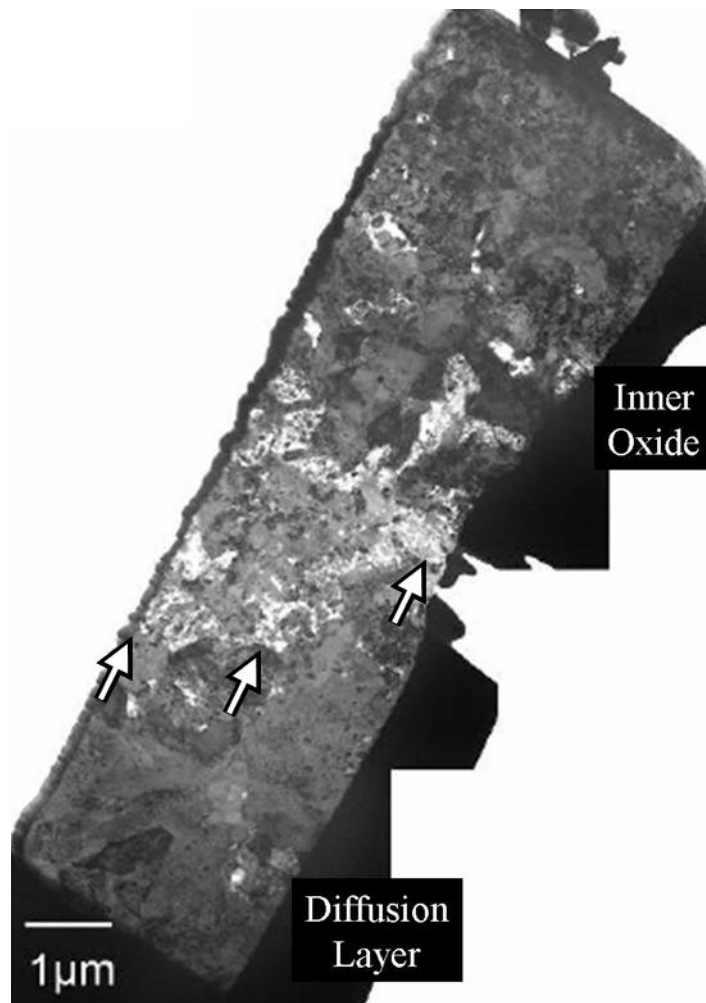


Figure 3.4: TEM bright field image of diffusion layer/inner oxide interface from 9Cr ODS, 4 week sample.

Figure 3.5 shows a bright field image of the first of two TEM specimens fabricated from the diffusion layer/metal interface. The diffusion layer shows equiaxed oxide grains, up to one micron in diameter, but the average grain within this layer is

approximately 500 nm in diameter. The diffusion layer in the 4 week sample shows a bold dark band along the metal/diffusion layer interface, as seen in the SEM image in Figure 3.2, which appears as a light band in the TEM bright field image of Figure 3.5 (indicated as region “A”). A pore approximately 1 μm in diameter (indicated by region “B”) near the metal/diffusion layer interface was found to have significant tungsten contamination, due to redeposition of the protective tungsten layer during milling. This indicates that any porous region can serve as a sink for milled particulate and that any pores found within a FIB prepared TEM sample may appear smaller than they would without contamination.

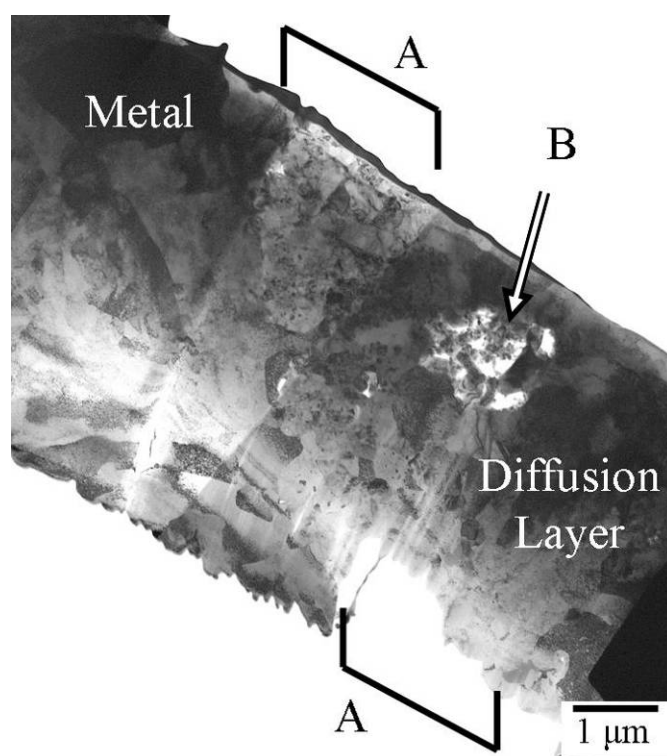


Figure 3.5: TEM bright field image of the first metal/diffusion layer interface specimen of 9Cr ODS, 4 week sample.

Figure 3.6 shows a bright field image of another sample from the diffusion layer/metal interface. The light band at the interface and marked as region “A” was found to be Cr-rich, as shown later by EELS analysis. Tilting this sample revealed that the light band along the diffusion layer/metal interface consists of either large irregularly shaped grains or large areas of grouped grains which could be highly oriented. These shapes are better shown in the TEM bright field images of the diffraction pattern analysis in Figures 3.8 & 3.9 .

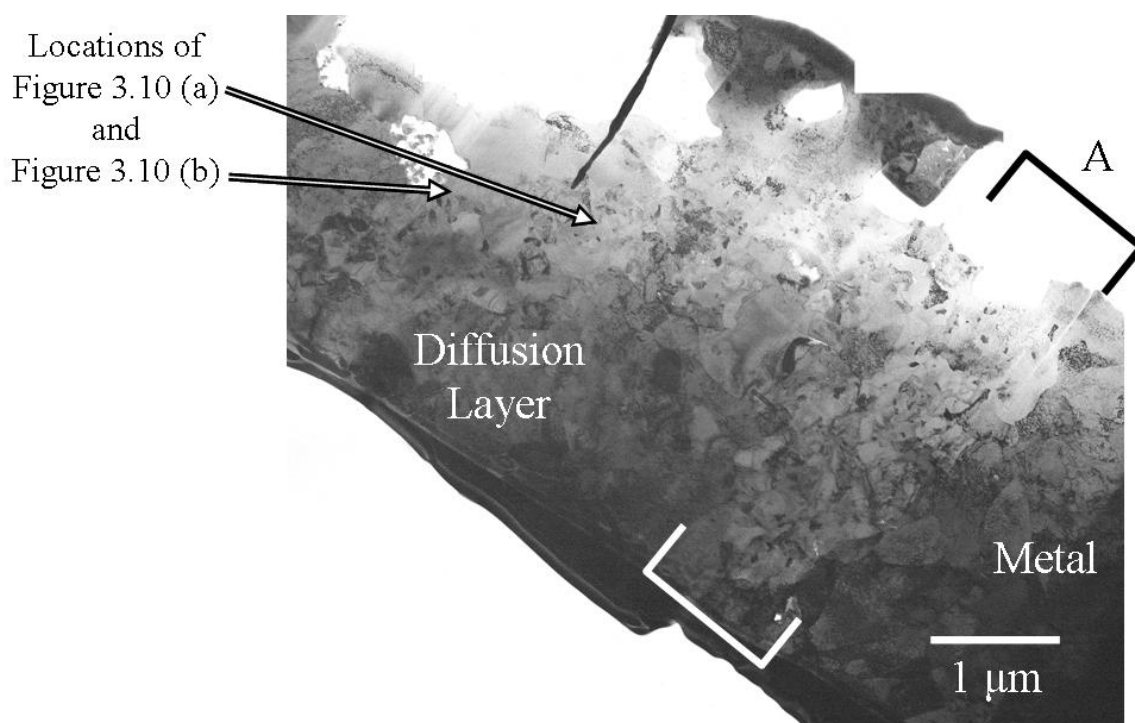


Figure 3.6: TEM bright field image of the second metal/diffusion layer interface specimen of 9Cr ODS, 4 weeks sample.

After initial SEM and TEM bright field analysis, TEM diffraction patterns were taken to help determine which phases are present in each sub-layer.

Figure 3.7(a) shows a diffraction pattern and corresponding bright field image from the outer oxide layer, which was indexed as Fe_3O_4 . Figure 3.7(b) shows a bright field image of the small grains of the inner oxide and the corresponding diffraction pattern which was indexed as FeCr_2O_4 . The sub-structure of the diffraction pattern could not be identified. Since Fe_3O_4 and FeCr_2O_4 have the same crystal structure with only slight lattice parameter differences, it is difficult to discern the two phases from electron diffraction information alone. Therefore, the designation Fe_3O_4 will be used whenever chromium is certain to not be present and the designation FeCr_2O_4 will be used when the presence of chromium is a possibility. The presence of chromium was detected with EDS. In any instance where either phase has initially been determined through TEM diffraction analysis, identification of the phase will be verified through EDS analysis. The white circles in the bright field images depict the sizes and locations of the selected area diffraction apertures for the corresponding diffraction patterns.

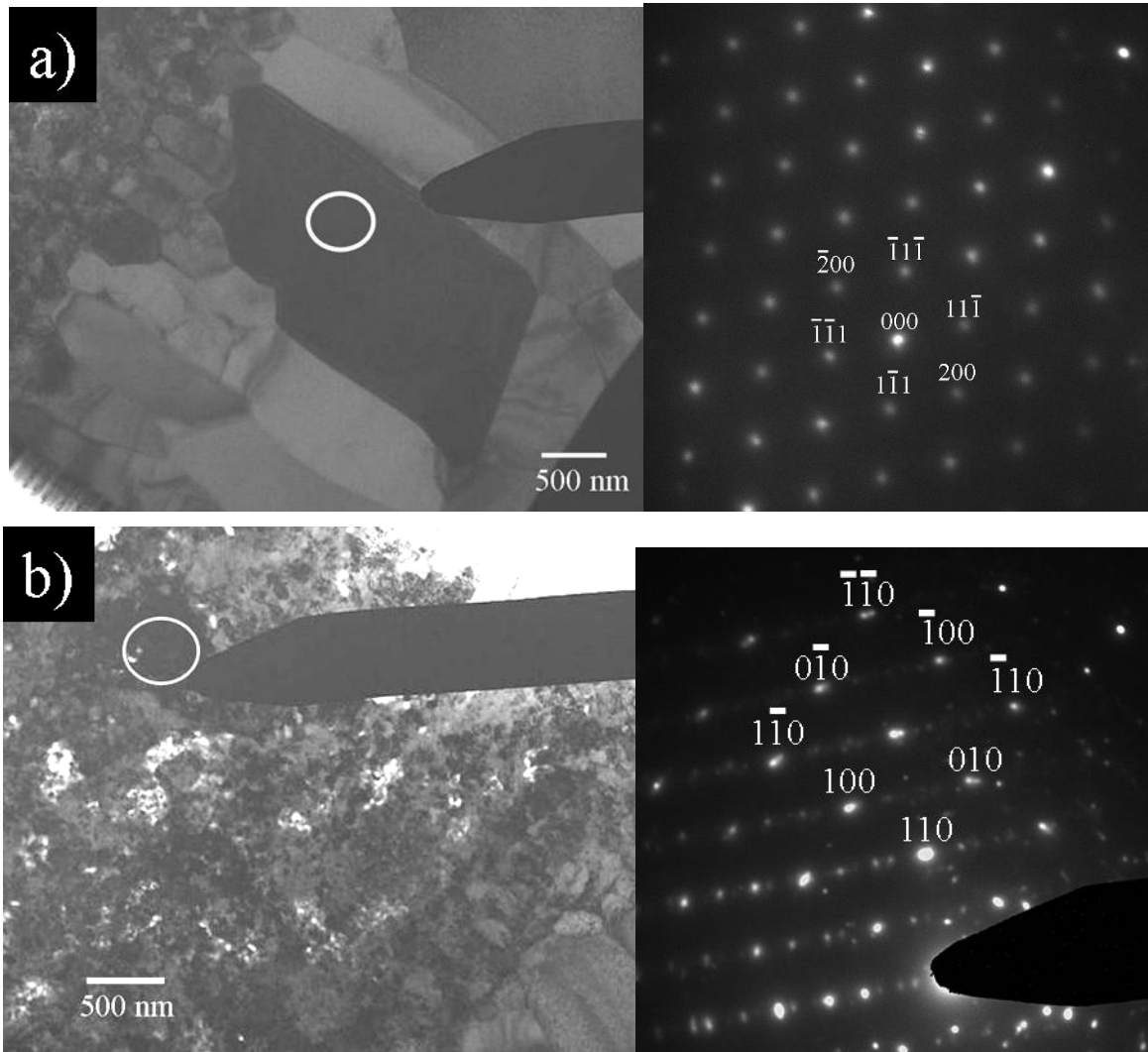


Figure 3.7: TEM bright field images and corresponding diffraction patterns of (a) Fe_3O_4 with zone axis $[011]$, taken from an outer oxide grain and (b) FeCr_2O_4 with zone axis $[001]$, taken from the inner oxide of 9Cr ODS, 4 week sample.

Since the location of the diffusion layer/inner oxide layer interface for this sample was difficult to define, it was decided to begin the diffusion layer analysis from the diffusion layer/metal interface.

Figure 3.8 & 3.9 show diffraction patterns taken from within the light band from the 2nd metal/diffusion layer sample (see Figure 3.5). Both diffraction patterns were taken

from the same Cr_2O_3 grain, tilted to the $[210]$ and $[241]$ zone axes, respectively. These diffraction patterns were indexed with the help of JEMS[15] simulated diffraction patterns, which are shown to the left of the experimental diffraction patterns. It has been determined that the entire band at the oxide front is composed of Cr_2O_3 .

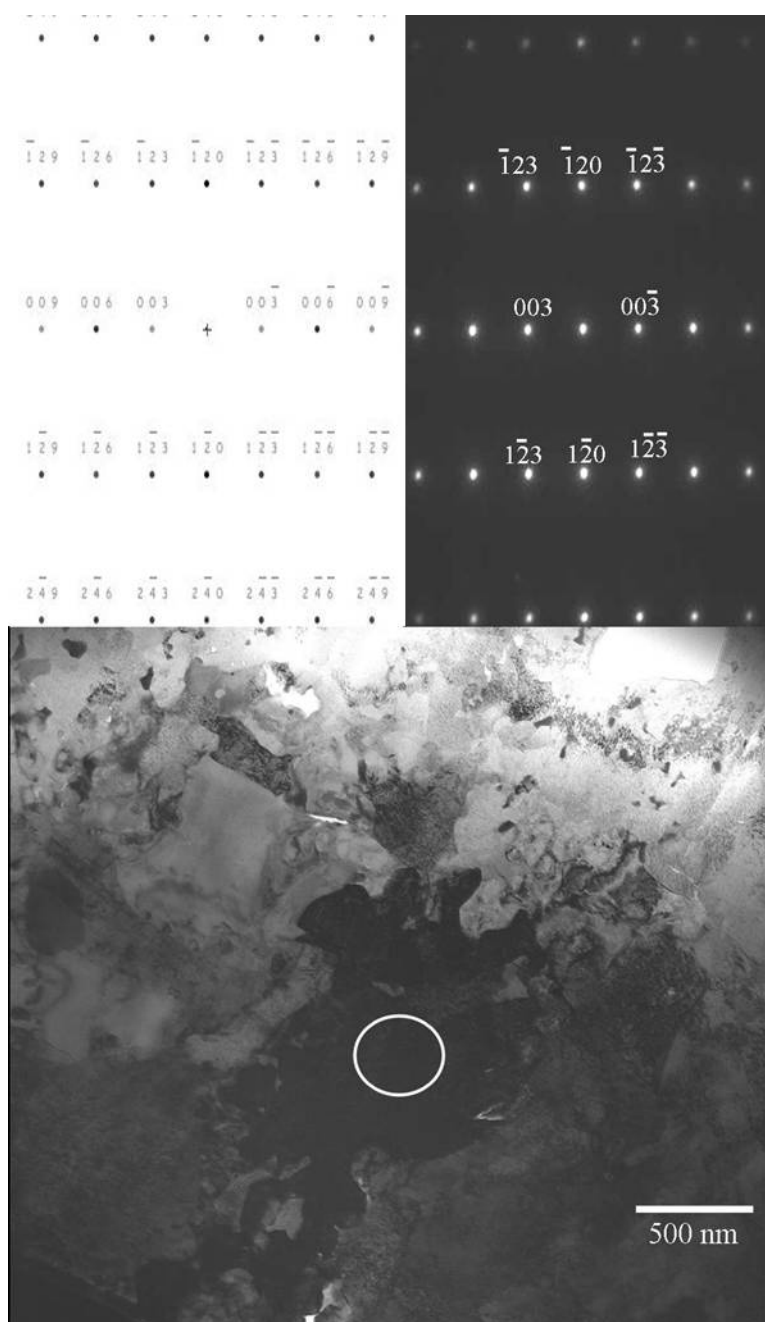


Figure 3.8: JEMS simulated diffraction pattern, TEM diffraction pattern, and corresponding bright field image of Cr_2O_3 , with a zone axis of $[210]$, from diffusion layer oxide front of 9Cr ODS, 4 week sample.

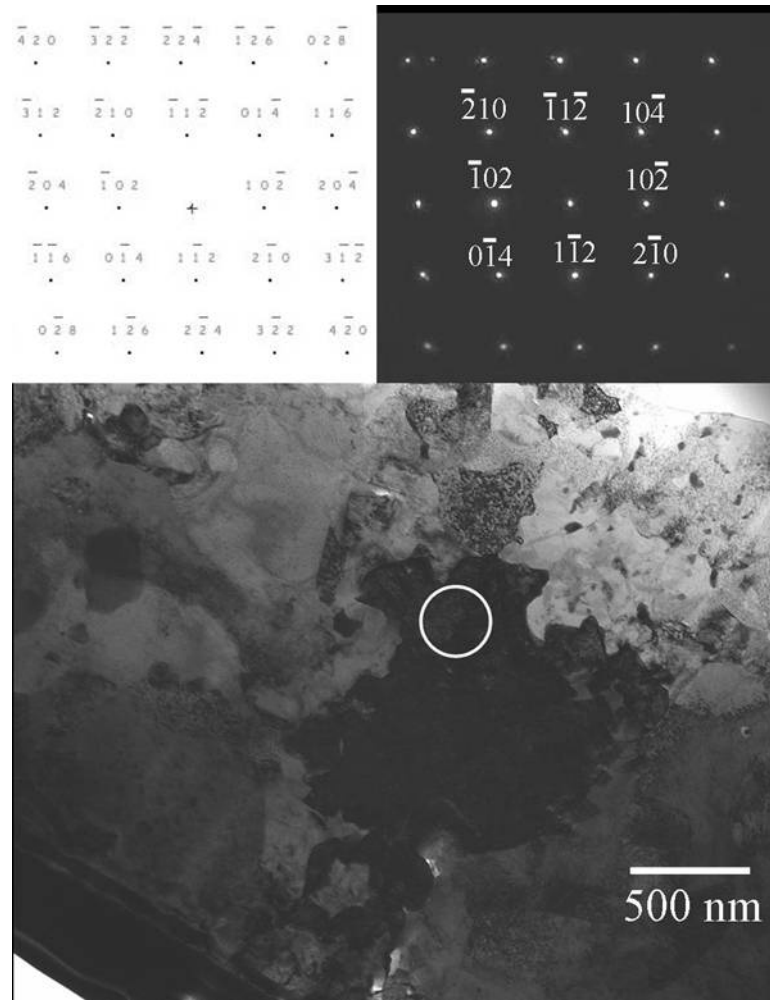


Figure 3.9: JEMS simulated diffraction pattern, TEM diffraction pattern, and corresponding bright field image of Cr_2O_3 , with a zone axis of $[241]$, from diffusion layer oxide front of 9Cr ODS, 4 week sample.

Diffraction patterns taken from the region immediately trailing the Cr_2O_3 grains at the oxide front, could be indexed as FeCr_2O_4 . Figure 3.10 shows diffraction patterns from two different FeCr_2O_4 grains with zone axes of $[013]$ and $[112]$, respectively, and their locations within the diffusion layer are shown in Figure 3.6. Cr_2O_3 and FeCr_2O_4 peaks were also found in the same locations in this sample during previous synchrotron analysis [20].

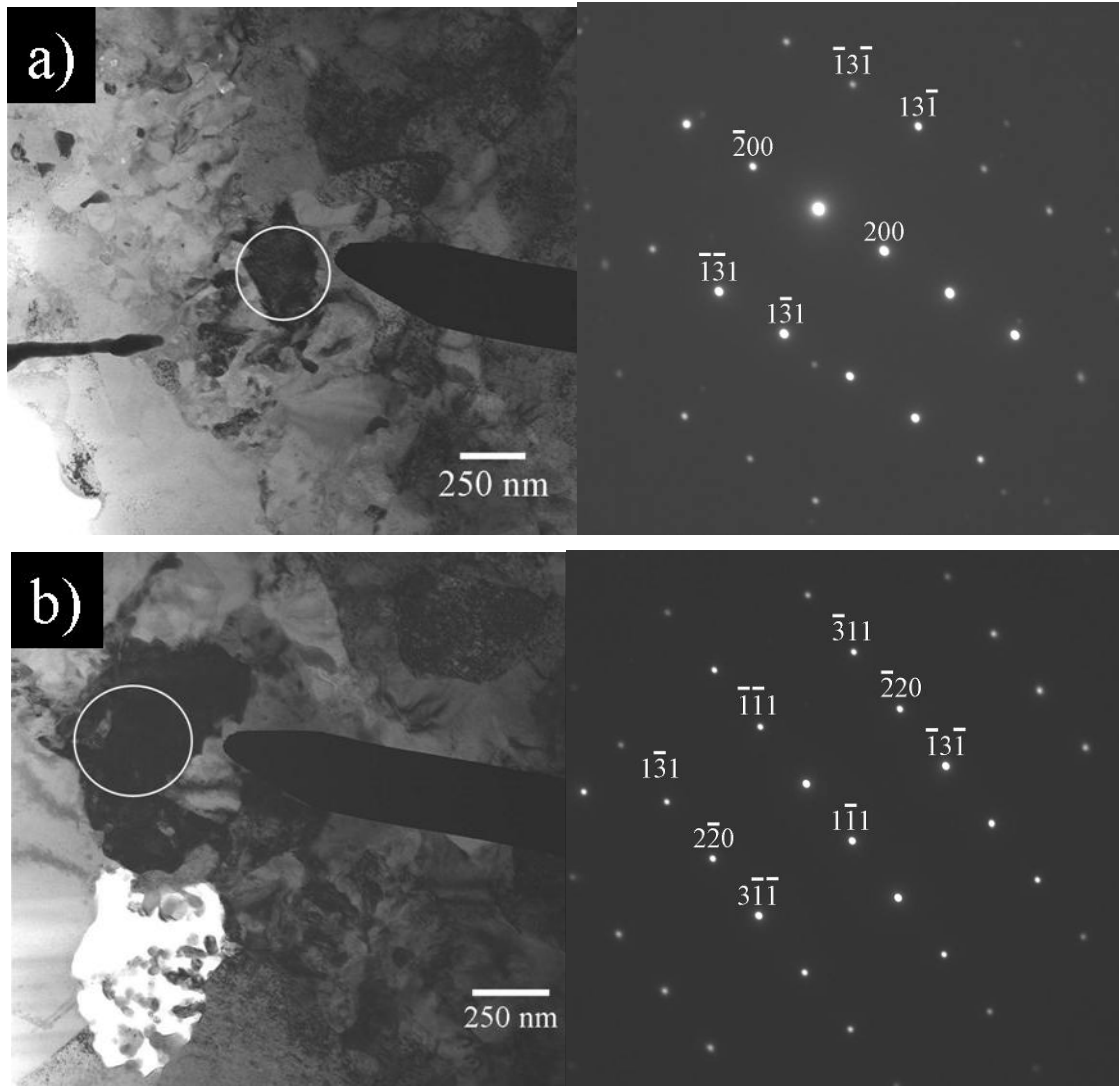


Figure 3.10: TEM bright field images and corresponding diffraction patterns of FeCr_2O_4 , (a) with a zone axis of $[013]$ and (b) with a zone axis of $[112]$, within the diffusion layer of 9Cr ODS, 4 week sample.

Energy Dispersion Spectroscopy analysis was performed on each layer to aid in the identification of phases within each layer.

The EDS overlay of spectra from the outer oxide layer and the inner oxide layer is shown in Figure 3.11. All EDS spectra from the outer oxide layer show only iron and oxygen with no chromium present, which confirms the outer oxide layer is composed of Fe_3O_4 . The inner oxide layer spectrum shows the same peaks as the outer oxide layer spectrum with additional chromium peaks, which was characteristic of all spectra acquired from the inner oxide layer. This indicates that FeCr_2O_4 is a likely phase, but does not indicate the absence or presence of Fe_3O_4 within the inner oxide layer. Previous synchrotron diffraction analysis was able to confirm that both FeCr_2O_4 and Fe_3O_4 are present in the inner oxide layer and only Fe_3O_4 in the outer oxide layer.

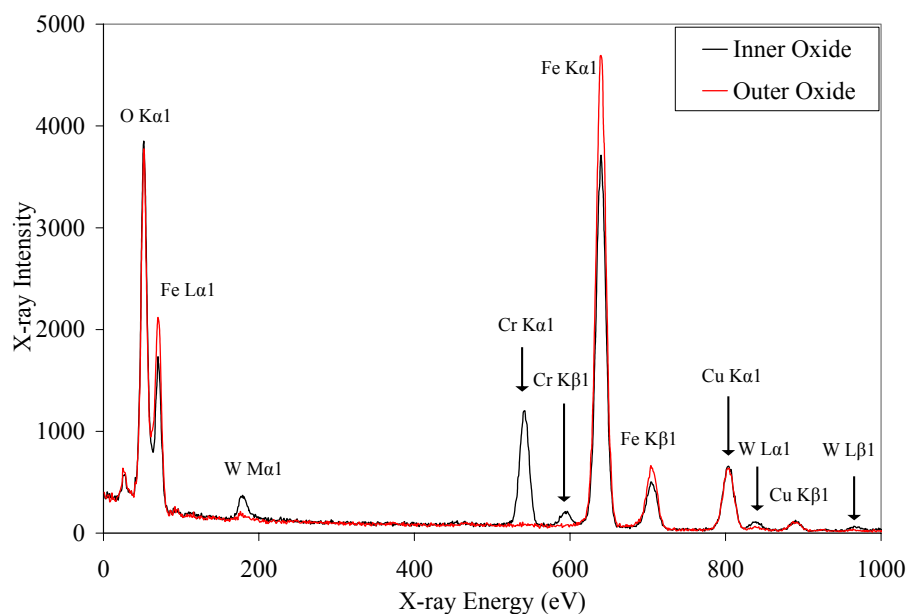


Figure 3.11: EDS overlay of spectra from inner oxide layer (black) and outer oxide layer (red).

EDS was also used to investigate the diffusion layer/metal interface, especially the band identified as Cr_2O_3 , to confirm diffraction analysis. A spectrum was taken from the metal layer far enough away from the oxide layer, so that a reference point could be taken. Figure 3.12 shows EDS spectra overlay of a spectrum from the oxide front, presumed to be Cr_2O_3 , compared to a spectrum from the metal. The spectrum from the oxide front shows chromium and oxygen enrichment with little iron present; whereas, the reference spectrum from deep inside the metal layer shows prominent iron peaks, minor chromium peaks, and no oxygen peaks. This is in agreement with the diffraction analysis mentioned above.

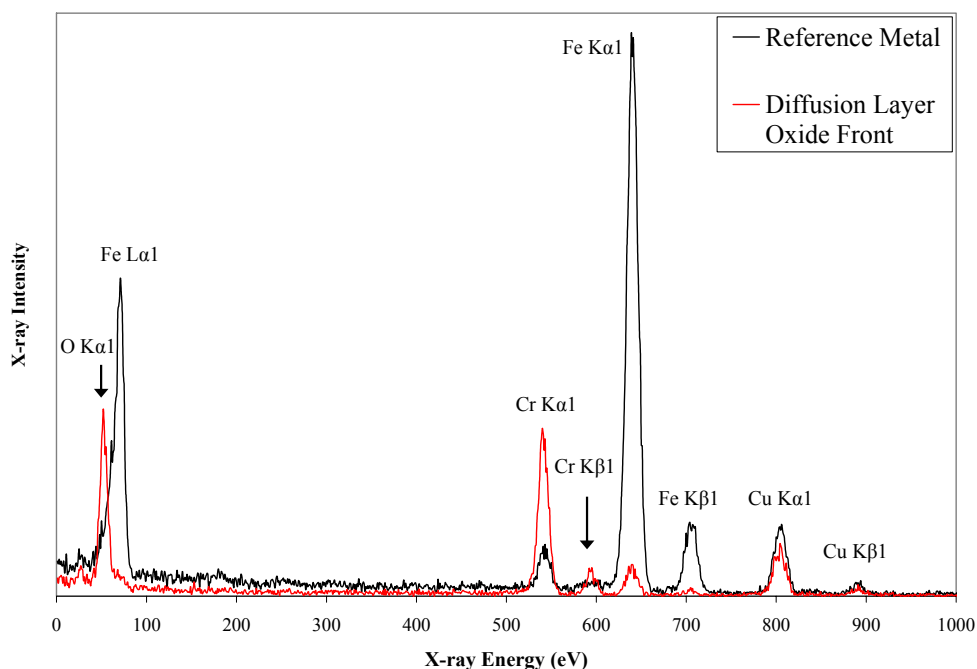


Figure 3.12: EDS spectra of reference metal and region determined to be Cr_2O_3 in diffusion layer of 9Cr ODS, 4 week sample.

To characterize the elemental distribution in the oxide layer, electron energy loss spectroscopy (EELS) was performed at the oxide front to determine if the entire band was composed of Cr_2O_3 or a combination of phases. Low magnification EELS maps were taken from the 2nd diffusion layer/metal sample and are displayed in Figure 3.13. The band of Cr_2O_3 is located in the bracketed region marked “A”. There is a strong correlation between the chromium and oxygen maps; whereas, the iron map appears as an inversion of the chromium and oxygen maps. This indicates the chromium oxidizes preferentially and there is a mixture of Cr-rich oxide and Fe-rich metal in the diffusion layer. The scale bars in the top left corner of the EELS maps are one micron in length. The diffusion layer/metal interface is located near the bottom of the red box, where the iron map shows a high concentration.

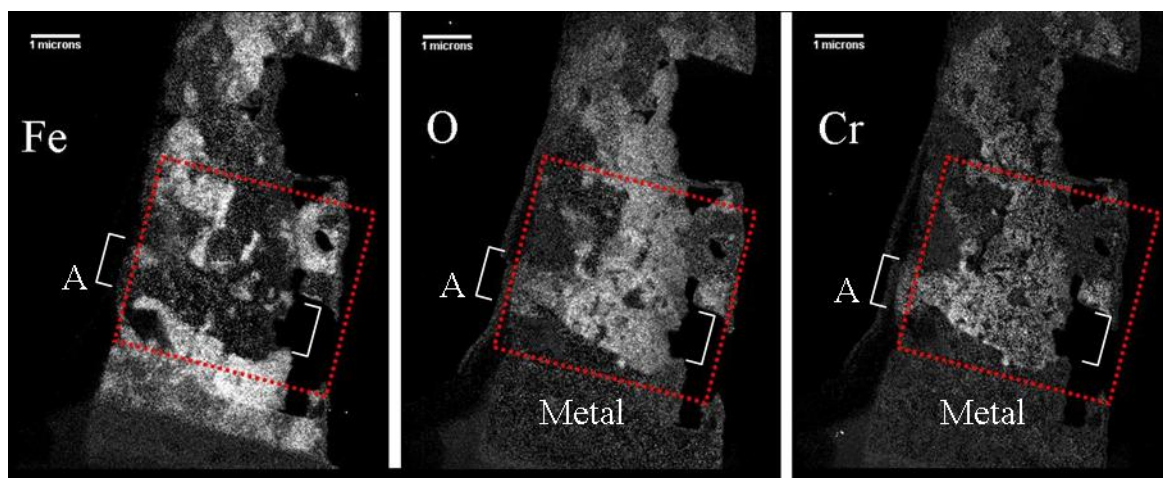


Figure 3.13: Low magnification EELS maps of iron, oxygen, and chromium for the diffusion layer/metal interface sample of 9Cr ODS, 4 week sample.

The regions located within the red boxes on the low magnification EELS maps of Figure 3.13 are shown in the high magnification EELS maps in Figure 3.14. The scale bars in the lower left corner for these EELS maps are 0.25 μm in length. It can be seen from the EELS maps that the oxygen and chromium maps show a sharp contrast at the metal/ diffusion layer interface. The band (between the brackets marked “A”) at the interface, previously determined to be Cr_2O_3 , appears clearly as a dark band in the iron map, and a light band in the chromium and oxygen maps. The EELS maps show small iron “islands” within the Cr_2O_3 band. This confirms the composition of the band at the oxide front to be a combination of chromium and oxygen, with traces of iron or iron oxide grains.

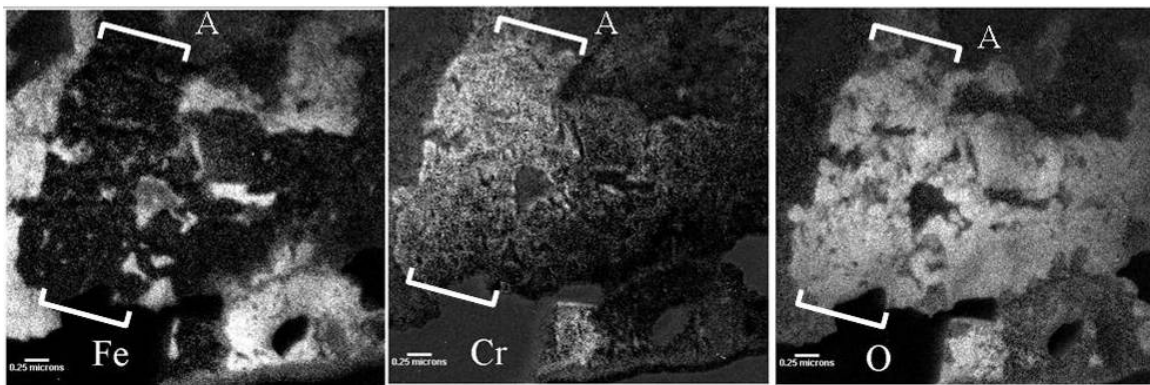


Figure 3.14: EELS maps of iron, oxygen, and chromium for the diffusion layer/metal interface of 9Cr ODS, 4 week sample.

This oxide was also examined by the Advanced Photon Source (APS) at Argonne National Laboratory using microbeam synchrotron diffraction and fluorescence.

Figure 3.15 shows microbeam synchrotron fluorescence scan from the 9Cr ODS 4 week sample in which the iron and chromium $K_{\alpha 1}$ counts are plotted versus distance. The shapes of the iron and chromium peaks are complementary, in the sense that, when the iron decreases, chromium increases. From Figure 3.15 we can see that the diffusion layer is depleted in iron compared to the base alloy, the inner oxide layer has even less iron, but the outer oxide layer has a higher concentration of iron than in any other region. This indicates that the iron, which is feeding the outer oxide, is coming from the diffusion layer but more so from the inner oxide. The outer oxide layer has no chromium, in agreement with the TEM EDS analysis. Also, the synchrotron fluorescence data shows a sharp increase of chromium at the metal/diffusion layer interface, which agrees with the finding of Cr_2O_3 at the oxide front.

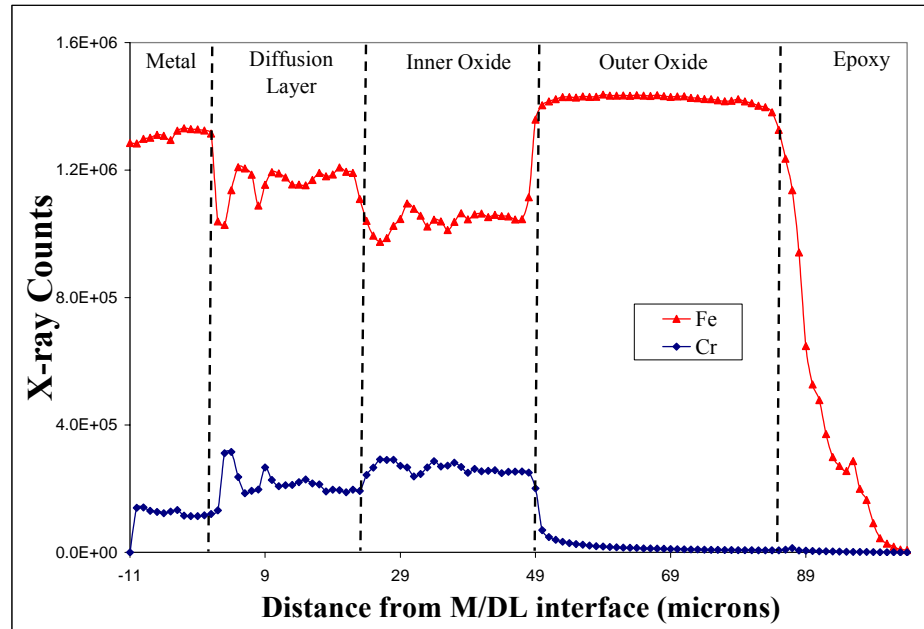


Figure 3.15: Microbeam synchrotron fluorescence of counts associated with iron and

chromium $K_{\alpha 1}$ peaks versus distance in the oxide layer for 9Cr ODS, 4 week sample.

A summary of the phases found in each sub-layer of the oxide is listed in Table 3.1.

Table 3.1: List of phases found in the various layers of 9Cr ODS.

Layer	Outer oxide	Inner oxide	Diffusion layer	Meta l
Phases Found	Fe_3O_4	$FeCr_2O_4$ and possibly Fe_3O_4	Fe-bcc, Cr_2O_3 and $FeCr_2O_4$ and/or Fe_3O_4	Fe-bcc

3.1.1.2 Analysis of oxide layer formed on 9Cr ODS, after 2 weeks exposure to 600°C SCW

Figure 3.16 shows an SEM micrograph of the oxide layer after 2 week SCW exposure. This sample exhibits three sub-layers: an outer oxide, an inner oxide, and a diffusion layer with thicknesses of 22.3 μm , 9.5 μm , and 28.6 μm , respectively. The diffusion layer is much thicker in this shorter exposure sample, and a different morphology is seen, consisting of dark tendrils uniformly progressing into the metal. It can be seen from the SEM image that a portion of the sample exhibits a dark wavy band at the diffusion layer/metal interface. Such a band was present throughout the diffusion layer/metal interface for the 4 week sample and was identified as a Cr-rich layer, with high content of Cr_2O_3 . The lack of a fully developed band makes the metal/diffusion

layer interface for the 9Cr ODS 2 week sample of particular interest. The approximate location from which the TEM sample was extracted is shown by the red dotted box in Figure 3.16.

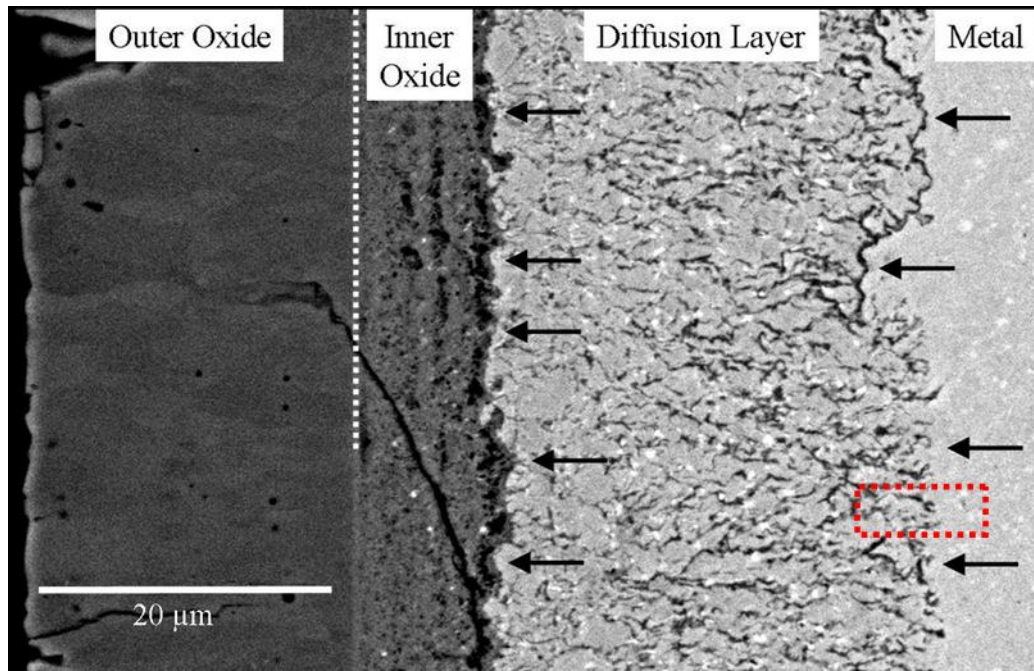


Figure 3.16: SEM backscatter electron image of the oxide sub-layers on 9Cr ODS, after 2 week exposure to 600°C SCW.

The TEM bright field image in Figure 3.17 shows the first 10 μm of the diffusion layer from the diffusion layer/metal interface. The metal layer starts at the beginning of the dark region at the right end of the sample.

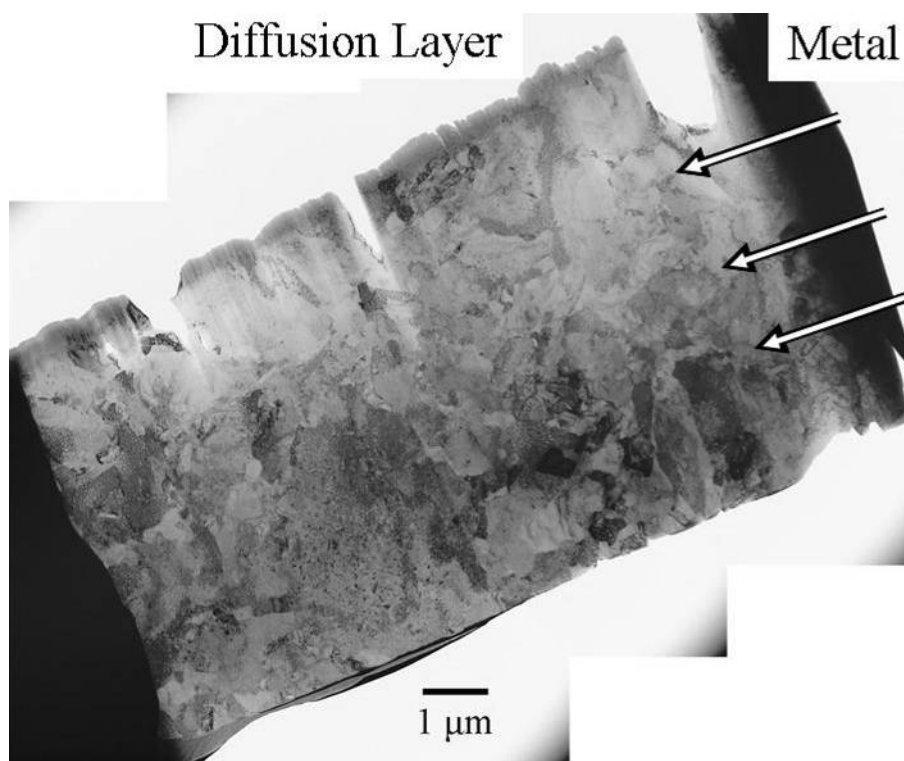


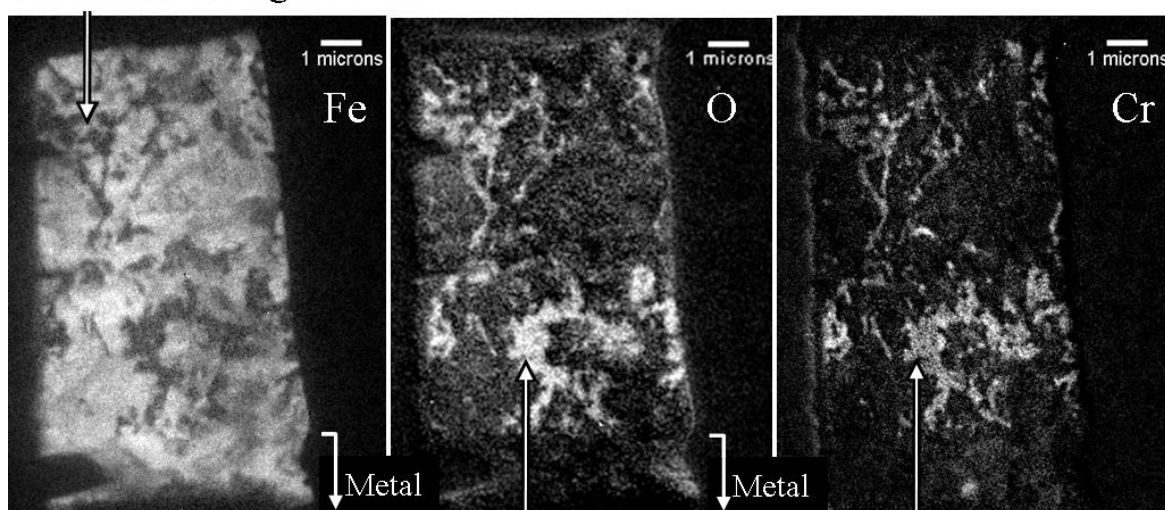
Figure 3.17: TEM bright field image of diffusion layer at the diffusion layer/metal interface of 9Cr ODS, 2 week sample. Arrows indicate the metal/diffusion layer interface.

As suspected from the SEM image of this sample, the TEM bright field image of the diffusion layer shows many grains that are neither columnar nor equiaxed, contrary to what was seen in the 4 week sample. Given this complicated structure of the diffusion layer from the TEM bright field image, EELS maps were used to quickly determine regions of interest for this sample.

Figure 3.18 shows EELS maps of iron, oxygen, and chromium for this sample. As in the 9Cr ODS 4 week EELS analysis, a strong correlation of chromium and oxygen within the diffusion layer can be seen in the EELS maps. It appears that the chromium and oxygen-rich filaments can be associated with the dark features seen within the

diffusion layer in Figure 3.16. The complex structure of the diffusion layer is revealed by the intricate detail in these EELS maps. EELS maps show that the majority of the diffusion layer has a strong presence of iron, and within these regions of high iron content, chromium and oxygen are not present. Using these EELS maps as a template, areas of interest were singled out in order for diffraction analysis to provide a more thorough understanding of the sample.

Location of Figure 3.19



Location of Figure 3.20

Figure 3.18: EELS maps of iron, oxygen, and chromium for the diffusion layer of 9Cr ODS, 2 week sample.

After initial SEM, TEM bright field and EELS analysis, TEM diffraction patterns were taken to help determine which phases are present in each sub-layer.

Figure 3.19 shows a bright field image of an iron containing grain. The corresponding diffraction pattern has been indexed with a zone axis of Fe-bcc [100].

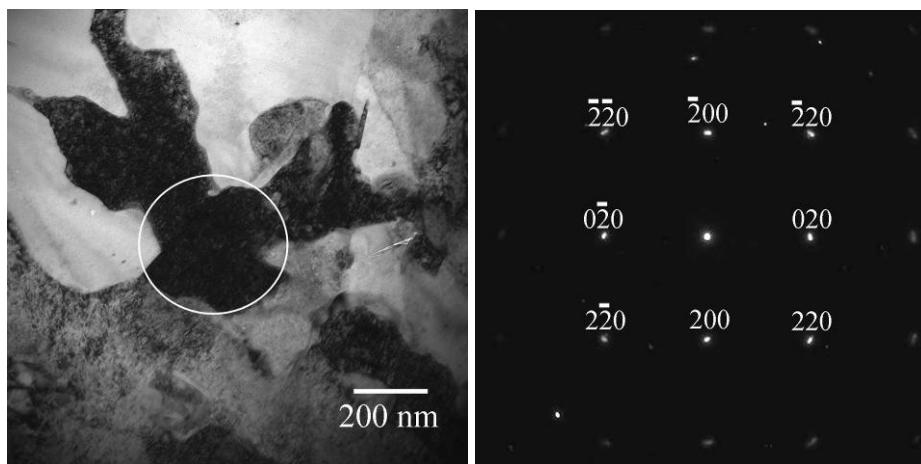


Figure 3.19: TEM bright field image and corresponding diffraction pattern of Fe-bcc with a zone axis of [001] within the diffusion layer of 9Cr ODS, 2 week sample.

Figure 3.20 shows a diffraction pattern and corresponding bright field image from a grain with high oxygen content. This diffraction pattern was indexed as FeCr_2O_4 with a zone axis of [011]. Other diffraction patterns have confirmed that the chromium and oxygen-rich regions are FeCr_2O_4 and that the iron-rich regions are Fe-bcc.

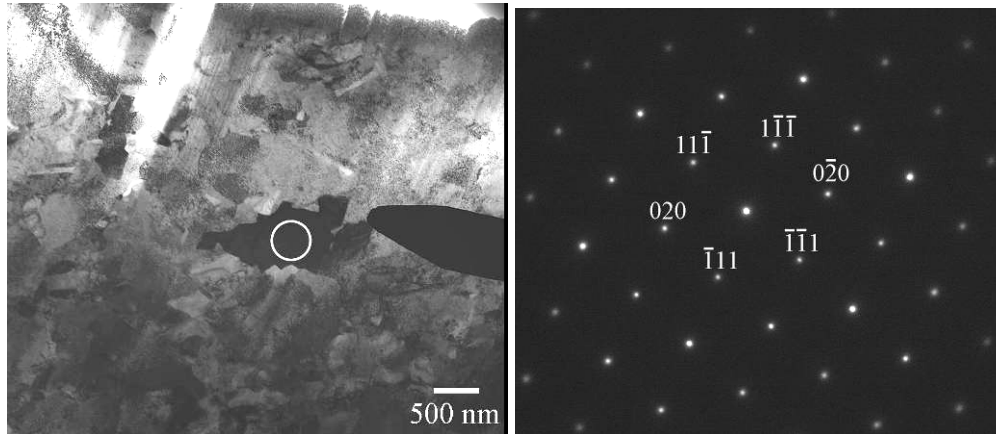


Figure 3.20: TEM bright field image and corresponding diffraction pattern of FeCr_2O_4 , with zone axis of $[101]$, within the diffusion layer of 9Cr ODS, 2 week sample.

In order to confirm these conclusions, the composition of these regions was analyzed using EDS. Figure 3.21 shows the EDS spectrum from the FeCr_2O_4 grain shown in Figure 3.20. The spectrum shows strong oxygen and chromium peaks, and smaller iron peaks. It can be seen from the spectrum that the chromium $K_{\alpha 1}$ peak is approximately twice the amplitude of the iron $K_{\alpha 1}$ peak. Combining this information with the diffraction analysis indicates that the grain is FeCr_2O_4 .

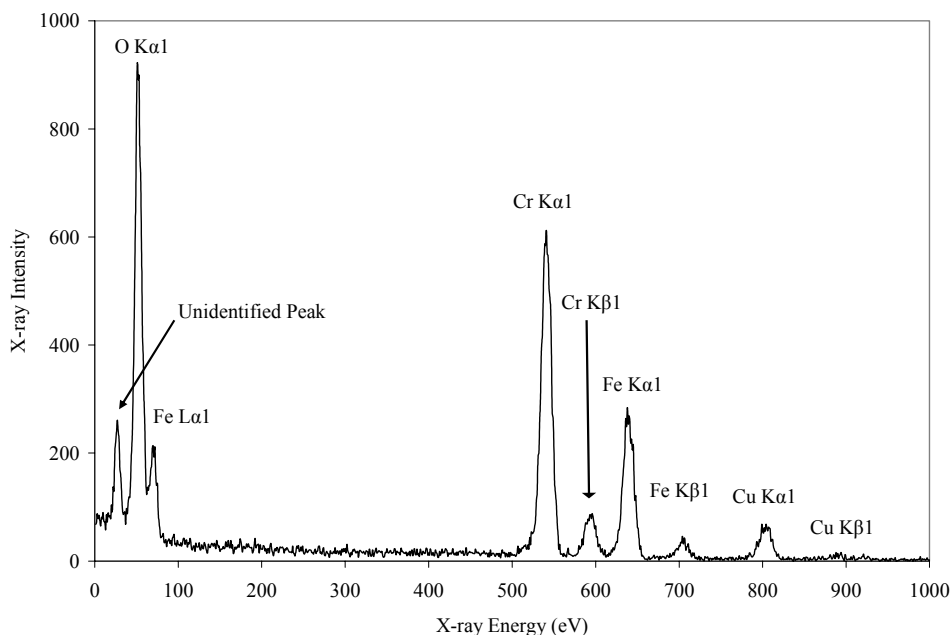


Figure 3.21: EDS spectrum of FeCr_2O_4 grain within the diffusion layer of the 9Cr ODS, 2 week sample.

The FeCr_2O_4 filament-like grains found within the diffusion layer were found to be no larger than $1.5\ \mu\text{m}$ in their longest dimension. This means that although the finger-like structure has been determined to be one phase, it is broken up into many differently oriented side-by-side grains.

The diffusion layer was found to have a mixture of Fe-bcc and FeCr_2O_4 . Although one large ($3.5\ \mu\text{m}$ diameter) Fe-bcc grain was found within this sample, most of the Fe-bcc grains were found to be one micron or less in their longest dimension. The iron grains were also found to be irregular in shape, as seen in Figure 3.19.

These observations largely agree with the microbeam synchrotron radiation fluorescence and diffraction examination of the same sample. Figure 3.22 shows

microbeam synchrotron fluorescence of iron and chromium $K_{\alpha 1}$ from the entire 9Cr ODS, 2 week. The fluorescence profile shows a gradual increasing level of chromium in the diffusion and inner oxide layers relative to the metal with a corresponding decrease of iron. The outer oxide layer is composed only of iron. Synchrotron radiation diffraction analysis found intense peaks, associated with the FeCr_2O_4 phase, within the diffusion layer combined with Fe-bcc. The synchrotron measurements can distinguish between FeCr_2O_4 and Fe_3O_4 , and Fe_3O_4 were not seen in the diffusion layer in agreement with the present study.

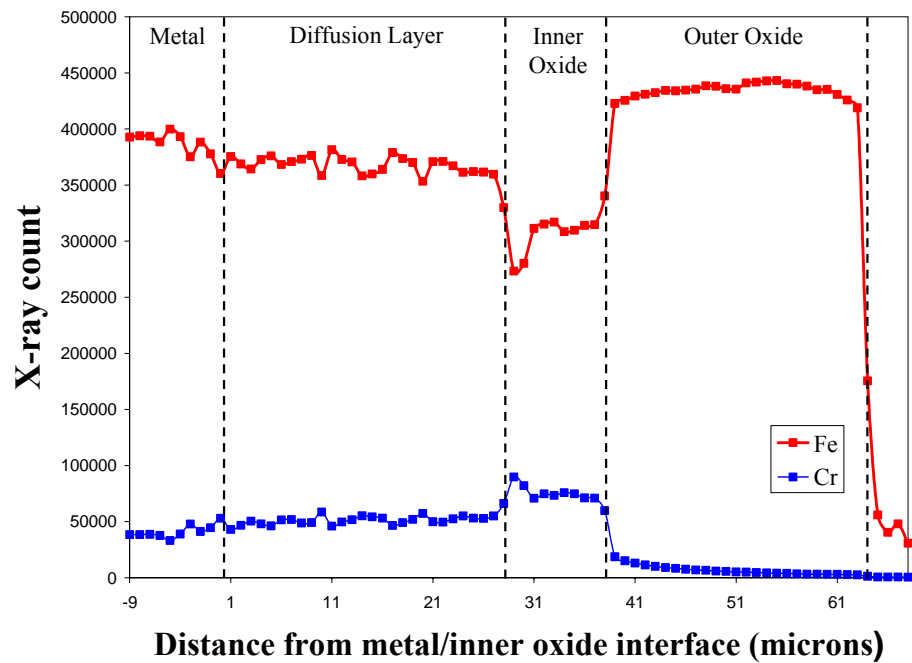


Figure 3.22: Microbeam synchrotron fluorescence of counts associated with iron and chromium $K_{\alpha 1}$ in 9Cr ODS, 2 week sample.

3.1.2 Analysis of oxide layer formed on HT-9 after 3 weeks exposure to 500°C SCW

Figure 3.23 shows a SEM micrograph of the oxide layer formed on HT-9 after corrosion in SCW for 3 weeks. The layer exhibits three sub-layers: an outer oxide, an inner oxide, and a diffusion layer, with approximate thicknesses of 6.6 μm , 4.8 μm , and 2.4 μm , respectively. The ratio of the outer oxide layer to the inner oxide layer is approximately 1.38. The thickness of the oxide layer developed on this sample is almost 1/4 of the thickness of the oxide layer developed on 9Cr ODS, and although a direct correlation cannot be made, it is expected to find a smaller oxide thickness for a lower temperature. The inner oxide layer has significant porosity along the inner oxide/diffusion layer interface, which was also seen in the inner oxide layer of 9Cr ODS. The SEM image also shows four noticeable bright white spots in the inner oxide layer, which are likely artifacts from sample polishing. The arrows indicate the location of the diffusion layer/metal interface, which appears to be developing along the grain boundaries of the metal as indicated by the morphology of the diffusion layer in comparison to the bare metal.

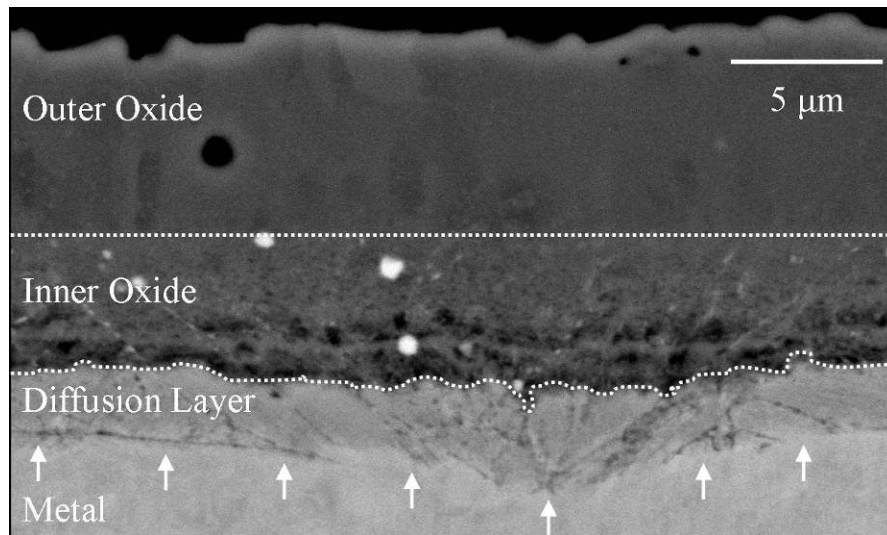


Figure 3.23: SEM backscatter electron image of HT-9, after 3 weeks exposure to 500°C SCW, showing the different oxide sub-layers.

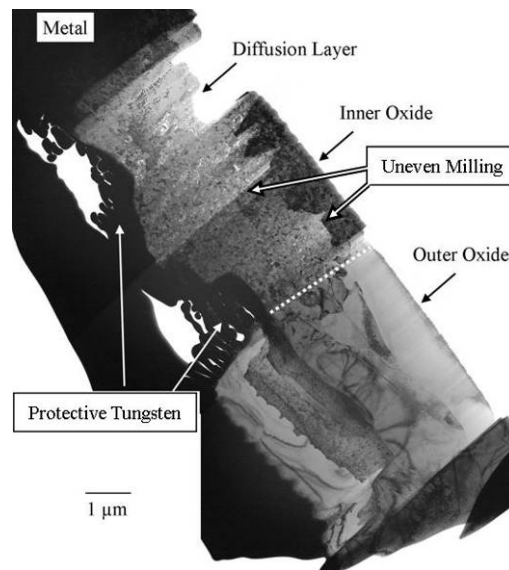


Figure 3.24: TEM bright field image of all three oxide sub-layers on HT-9, after 3 weeks exposure to 500°C SCW. Artifacts are shown in boxes.

Figure 3.24 shows a TEM bright field image of all three sub-layers. Because this oxide layer is thinner overall, it is possible to make a cross-sectional TEM sample showing all the layers. The outer oxide layer shows large columnar grains up to 1 μm wide by 5 μm long, which is similar to those found in the oxide layer developed on 9Cr ODS. The outer oxide layer also exhibits small equiaxed grains (~ 500 nm in diameter) along the outer oxide/inner oxide interface. Similar to the oxide layer developed on 9Cr ODS, the inner oxide layer is composed of small equiaxed grains, no larger than 100 nm in diameter, as shown in Figure 3.25. Through TEM examination, and tilting, it was found that a large group of grains (with a diameter almost the size of the inner oxide layer) within the inner oxide layer is highly oriented. This group of grains is shown as the dark region enclosed by the arrows in Figure 3.25. The entire group of grains exhibited the same TEM diffraction pattern and the orientation is explained later in the TEM diffraction analysis corresponding to Figure 3.29.

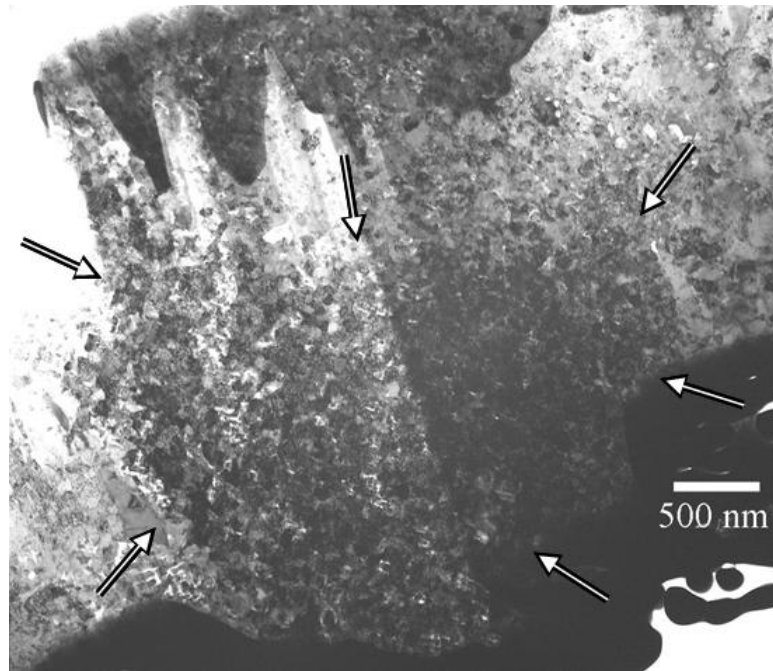


Figure 3.25: TEM bright field image of the inner oxide layer of HT-9 after 3 weeks exposure to 500°C SCW.

The majority of the grains in the inner oxide layer are equiaxed, with diameters of ~100 nm. Figure 3.26 shows a structure observed in the diffusion layer, near the interface with the inner oxide layer. This structure is composed of white platelets growing in two orthogonal directions, amidst a dark background. This region extends approximately 2 μm by 2 μm . The platelets grew parallel and perpendicular to the oxide growth direction.

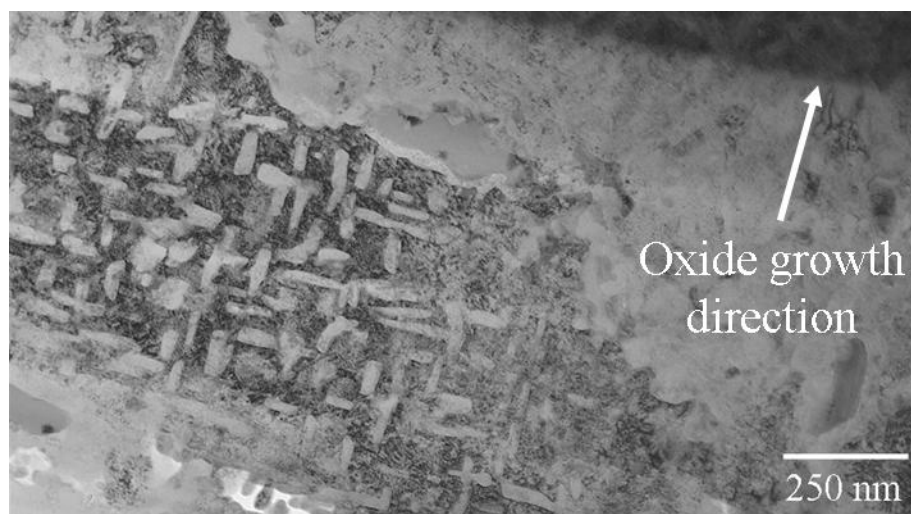


Figure 3.26: TEM bright field image and magnification of highly-ordered Fe-bcc and FeCr_2O_4 within the diffusion layer of HT-9, after 3 weeks exposure to 500°C SCW.

It appears that the dark region in Figure 3.26 corresponds to the iron spots in the diffraction pattern in Figure 3.30, while the light strips within this region correspond to the FeCr_2O_4 spots from that same diffraction pattern. The dark field image of an Fe-bcc diffraction spot from the corresponding diffraction pattern in Figure 3.27 confirms this observation. The diffusion layer from this sample does not have a band of Cr_2O_3 at the oxide front nor does it have a finger-like structure of FeCr_2O_4 , as found in the oxides developed on 9Cr ODS after 4 weeks and 2 weeks exposure to SCW, respectively.

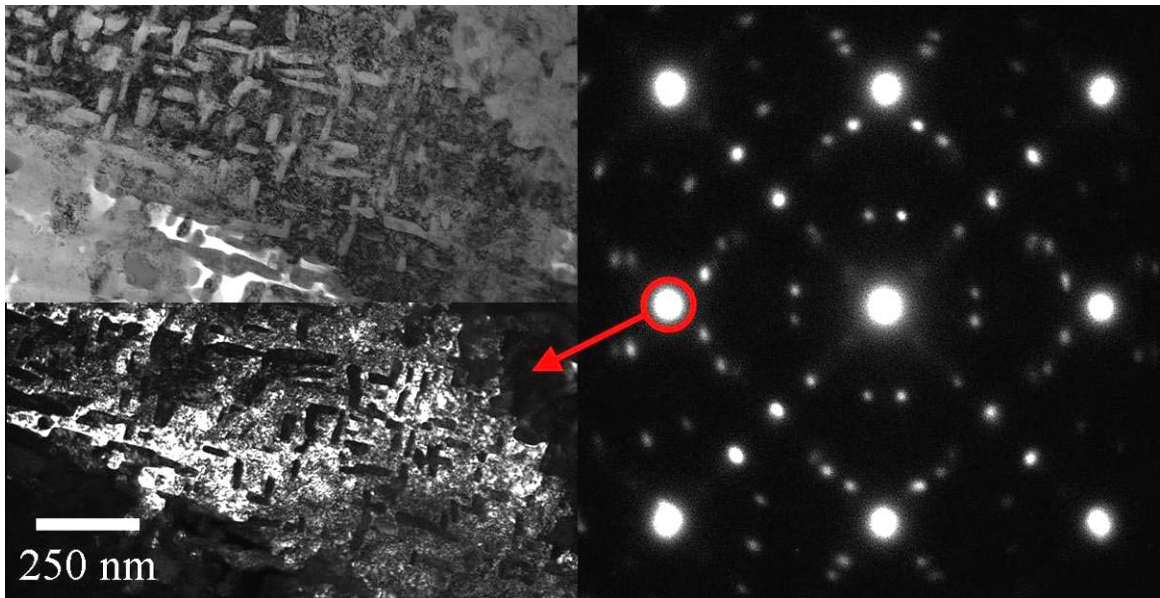


Figure 3.27: TEM dark field analysis of Fe-bcc diffraction spot from diffusion layer of HT-9, after 3 weeks exposure to 500°C SCW. (Note: This diffraction pattern is indexed in Figure 3.30.)

Diffraction analysis was performed to help determine which phases are present in each sub-layer.

Figure 3.28 shows a bright field image and corresponding diffraction pattern of an outer oxide grain. This diffraction pattern was indexed as Fe_3O_4 with a zone axis of $[-111]$. The remainder of the outer oxide layer provided diffraction patterns which were indexed as Fe_3O_4 .

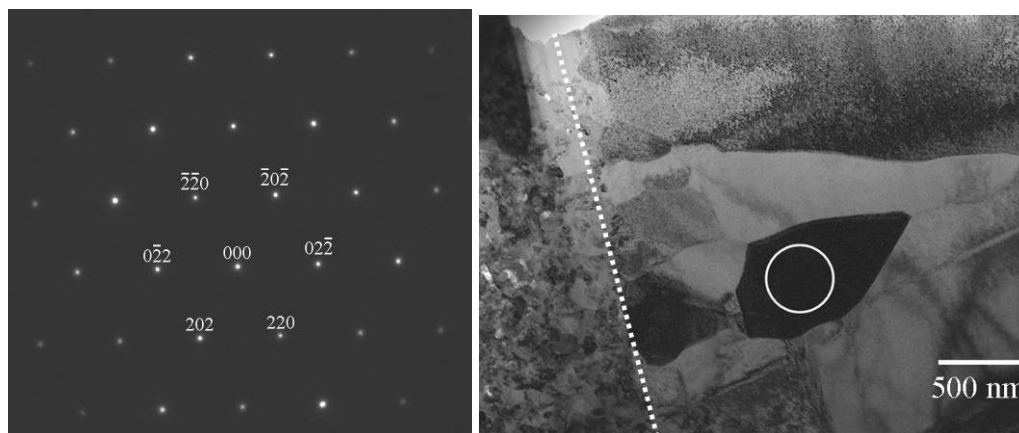


Figure 3.28: TEM diffraction pattern and corresponding bright field image of Fe_3O_4 , with a zone axis of $[-111]$, from outer oxide layer of HT-9, after 3 weeks exposure to 500°C SCW.

The inner oxide layer shows a large region of grains that diffract together (that is, they respond to tilt in the same manner). This region takes up more than half of the viewable inner oxide layer of the TEM sample fabricated for this study. Figure 3.29 shows a diffraction pattern and bright field image showing highly-oriented grains. The diffraction pattern was indexed as FeCr_2O_4 with two zone axes of $[111]$ and $[112]$, indicating two preferential orientations, and Fe-bcc with a zone axis of either $[112]$ or $[212]$. Simulated JEMS diffraction patterns were used to find the possible zone axes of $[112]$ and $[212]$ for Fe-bcc, which cannot be determined from the diffraction pattern because only a single row of diffraction spots can be seen in the diffraction pattern. The rest of the inner oxide layer provided diffraction patterns that were also indexed as FeCr_2O_4 .

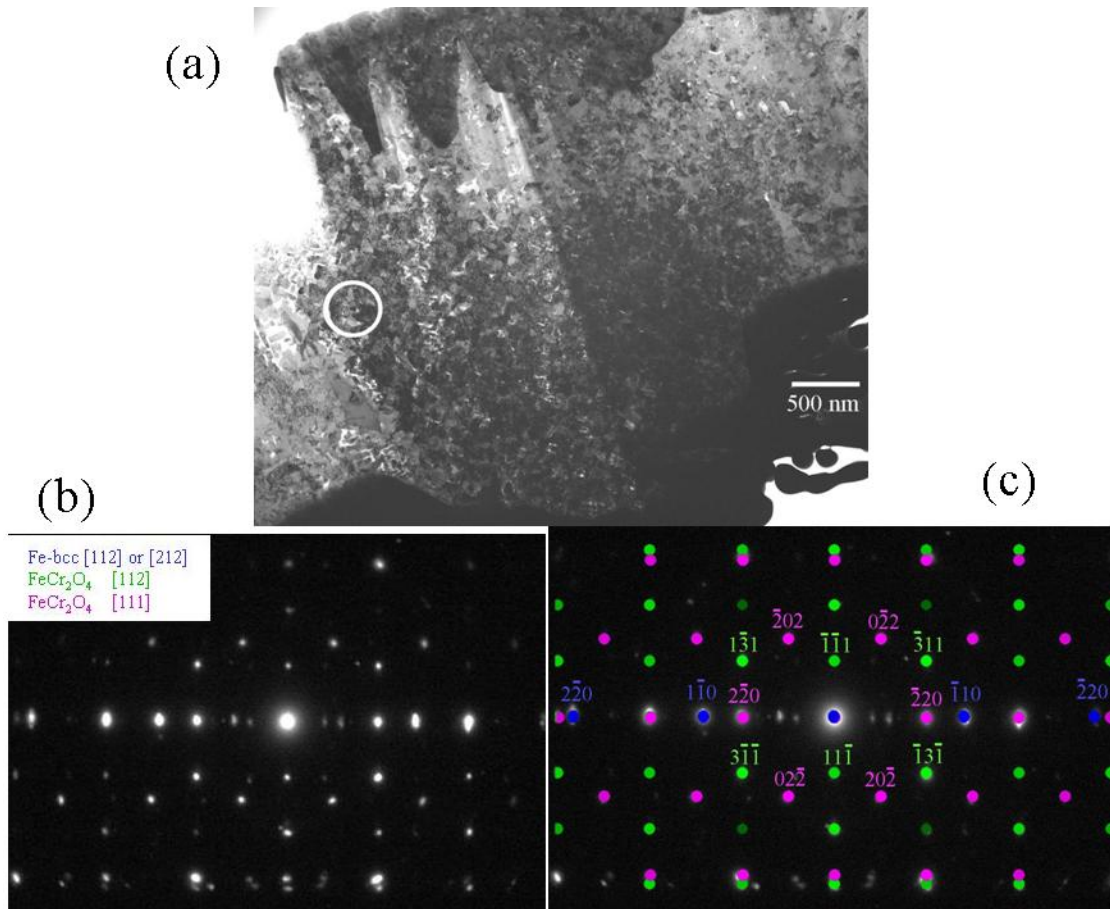


Figure 3.29: TEM (a) bright field image of highly-ordered FeCr₂O₄ grains within the inner oxide of HT-9, after 3 weeks exposure to 500°C SCW, (b) corresponding diffraction pattern, and (c) JEMS indexing of the experimental diffraction pattern.

The diffusion layer also exhibits strong preferential grain orientation. Figure 3.30 shows a diffraction pattern from the highly-oriented grains in the diffusion layer shown in Figure 3.26. The overall pattern is a composite of several sub-patterns: a dominant pattern of Fe-bcc with a zone axis of [100] and two additional patterns of FeCr₂O₄. The additional patterns of FeCr₂O₄ both have zone axes of [011], and are perpendicular to

each other as seen in the spot overlay of the experimental diffraction pattern in Figure 3.30.

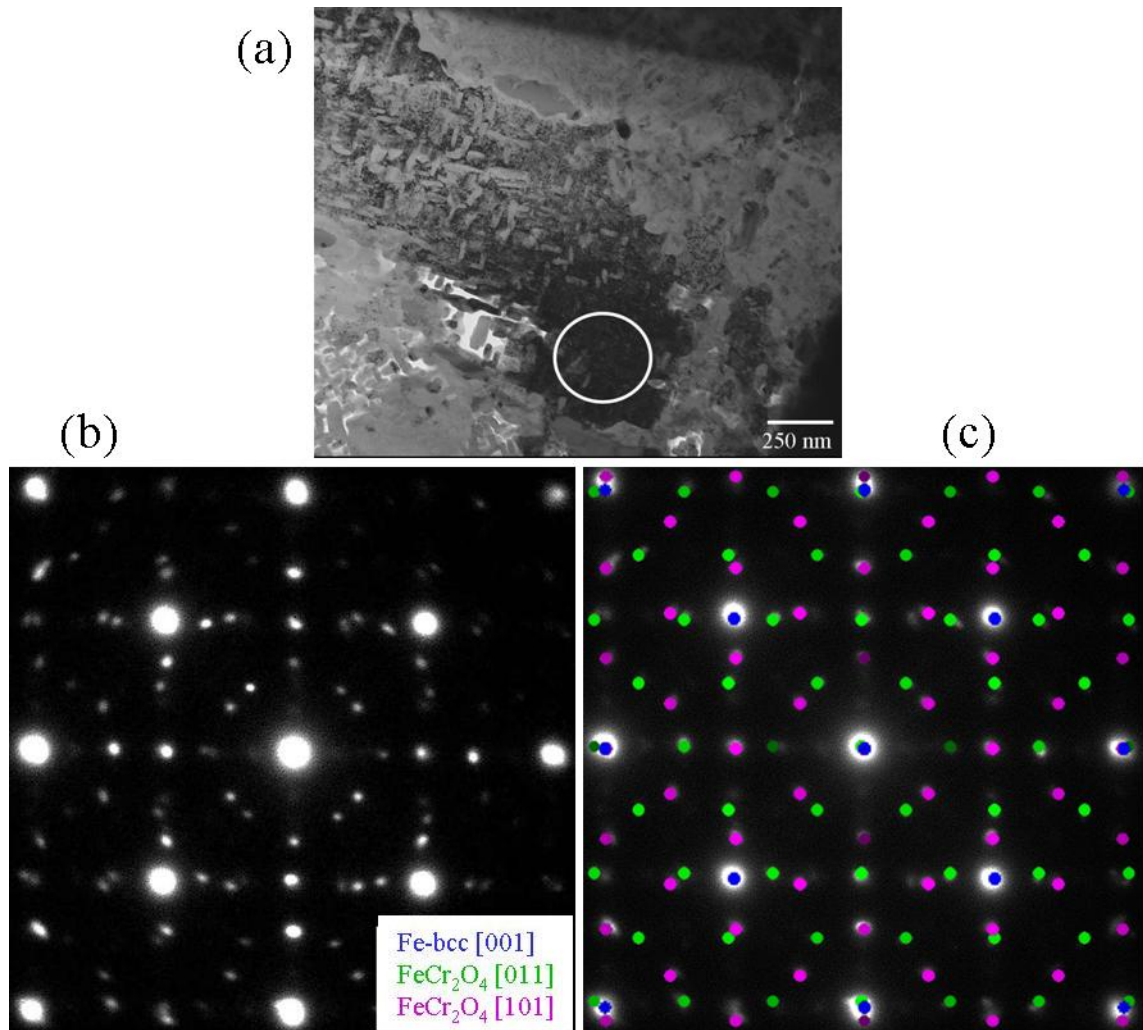


Figure 3.30: TEM (a) bright field image of highly-ordered Fe-bcc and FeCr₂O₄ within the diffusion layer of HT-9, after 3 weeks exposure to 500°C SCW, (b) corresponding diffraction pattern with zone axis [001] for Fe-bcc and with zone axes of [011] and [101] for FeCr₂O₄, and (c) JEMS indexing of the experimental diffraction pattern..

Figure 3.31 shows a diffraction pattern taken from a different part of the diffusion layer than the diffraction pattern in Figure 3.34. This pattern is very similar (same orientation and same indexing) to the diffraction pattern in Figure 3.29, which was taken from the inner oxide layer. One possible explanation for these diffraction patterns being the same is that as the oxide grows into the diffusion layer, it transforms the Fe-bcc portions into FeCr_2O_4 following the orientation of the existing FeCr_2O_4 platelets.

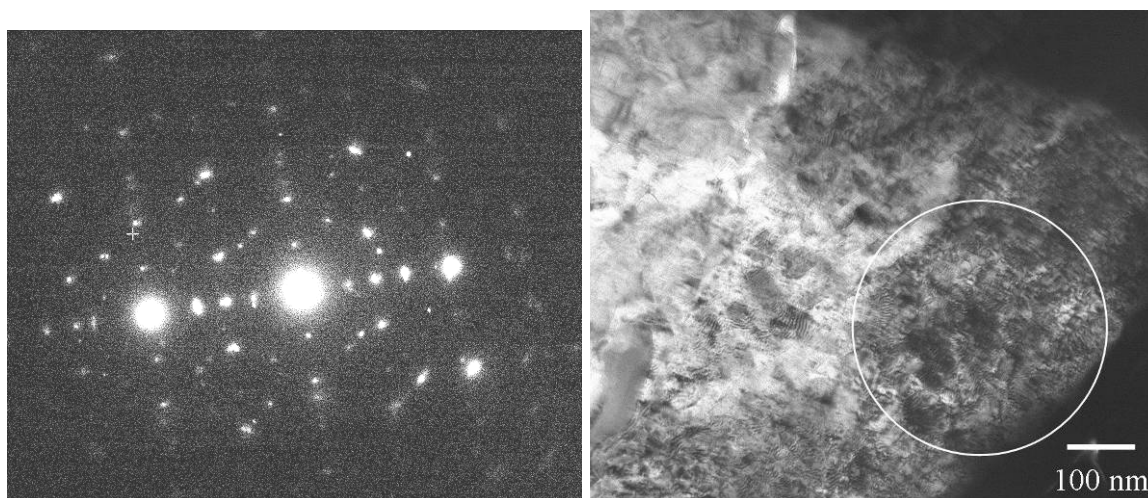


Figure 3.31: TEM diffraction pattern and corresponding bright field image of highly-ordered FeCr_2O_4 , with zone axes $[111]$ and $[112]$, and Fe-bcc within the diffusion layer of HT-9, after 3 weeks exposure to 500°C SCW. This diffraction pattern is exactly the same as that shown in Figure 3.29.

Energy Dispersion Spectroscopy analysis, providing chemical information to be coupled with the preceding diffraction pattern analysis, was performed on each layer with the purpose of confirming the identification of phases within each layer.

Just as EDS analysis showed no presence of chromium in the outer oxide layer for 9Cr ODS, no chromium was found in the outer oxide layer of HT-9. This information combined with TEM diffraction analysis indicates that the outer oxide layer consists of only Fe_3O_4 . In contrast, EDS analysis showed chromium to be present in the inner oxide layer, which is consistent with the presence of FeCr_2O_4 but does not tell us anything about the presence of Fe_3O_4 .

It is fairly easy to see in the SEM image in Figure 3.23 where each layer begins and ends, yet in the TEM image in Figure 3.24 of the same sample it is difficult to see the interfaces on either side of the diffusion layer. However, TEM EDS spectra taken across the diffusion layer/inner oxide interface shows a sharp contrast in oxygen concentration between the diffusion layer to the inner oxide layer as seen in Figure 3.32. The dotted line in the figure shows the approximate location of the diffusion layer/inner oxide interface. Figure 3.32 shows the ratios of the amplitudes of the $K_{\alpha 1}$ peaks of Cr/Fe and O/Fe from a manual EDS line scan across the diffusion layer/inner oxide interface as indicated in Figure 3.33.

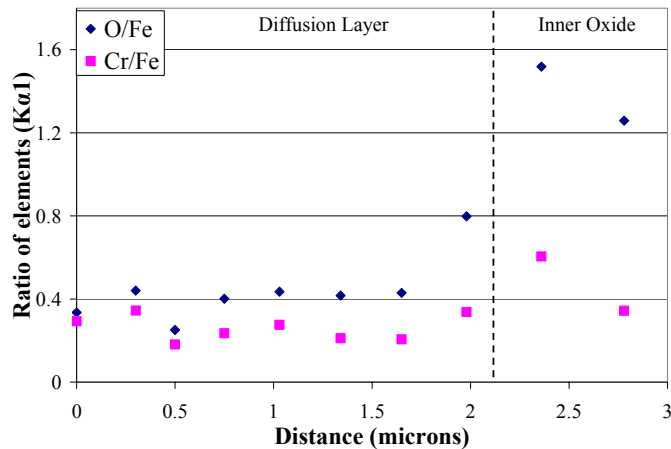


Figure 3.32: TEM EDS of the ratios of oxygen/iron and chromium/iron $K_{\alpha 1}$ spectral lines from diffusion layer to inner oxide of HT-9, after 3 weeks exposure to 500°C SCW.

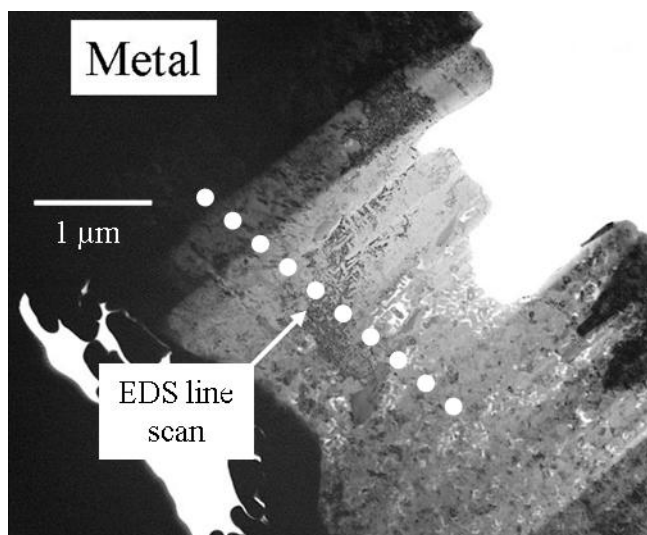


Figure 3.33: Location of EDS line scan data presented in Figure 3.32.

The same sample was also examined using microbeam synchrotron radiation diffraction and fluorescence. The microbeam fluorescence data for iron and chromium $K_{\alpha 1}$ in this oxide layer are shown in Figure 3.34. The outer oxide layer shows no

chromium, in agreement with the TEM EDS analysis. The inner oxide/diffusion layer interface is not defined by the sharp contrast that was seen in the fluorescence data for 9Cr ODS. Analysis of microbeam synchrotron radiation diffraction patterns in this same sample show a substantial decrease in the intensity of the Fe-bcc diffraction peaks as we go across the diffusion layer/inner oxide interface from the diffusion layer into the inner oxide layer. However, the Fe-bcc peak is still observed in the inner oxide layer, as in this work.

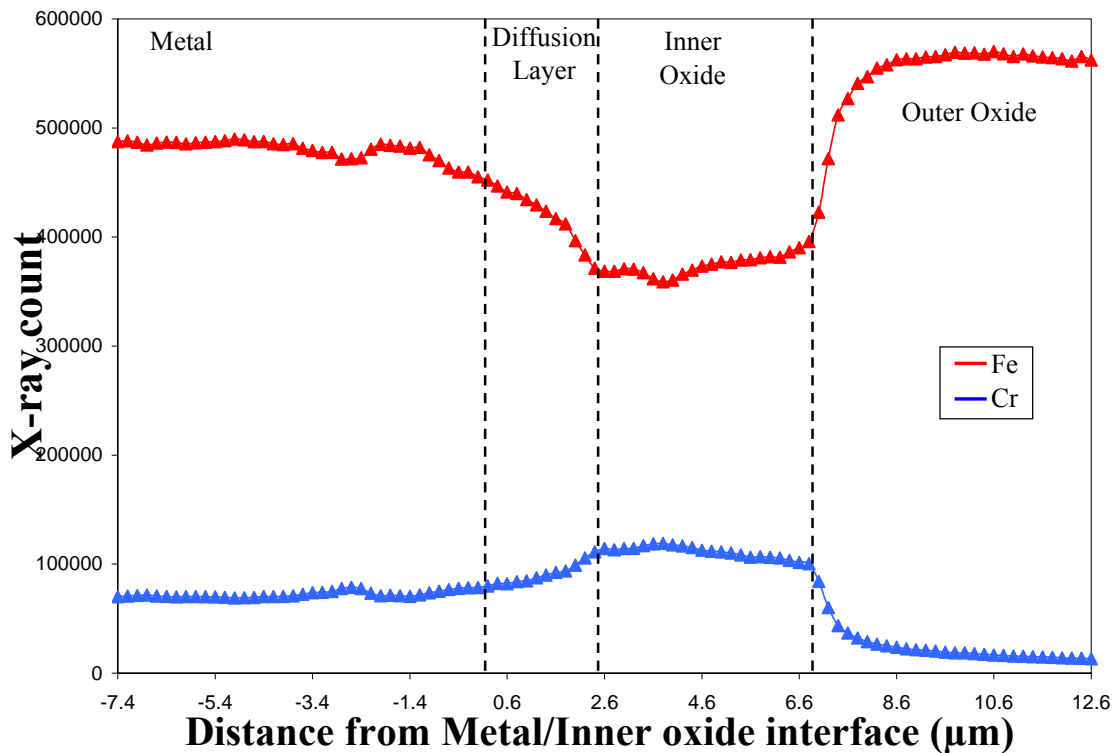


Figure 3.34: Microbeam synchrotron fluorescence of counts associated with iron and chromium $K_{\alpha 1}$ in HT-9, after 3 weeks exposure to 500°C SCW.

A summary of the phases found in each sub-layer of the oxide are listed in

Table 3.2.

Table 3.2: List of phases found within the various layer of HT-9 500°C, 3 weeks SCW corroded sample.

Layer	Outer oxide	Inner oxide	Diffusion layer	Meta l
Phases Found	Fe_3O_4	FeCr_2O_4 and possibly Fe_3O_4	Fe-bcc and FeCr_2O_4 and/or Fe_3O_4	Fe-bcc

3.1.3 SCW Alloy Corrosion Summary

Each of the oxide layers developed on HT-9 and 9Cr ODS exhibit an outer oxide layer, an inner oxide layer, and a diffusion layer. These sub-layers exhibit the same phases for both the HT-9 sample and 9Cr ODS, with the exception of an additional phase of Cr_2O_3 found at the oxide front of 9Cr ODS, 4 week sample. The grain sizes and morphologies for each sub-layer were also similar for both HT-9 and 9Cr ODS. The HT-9 sample shows highly oriented inner oxide and diffusion layers, which indicate that the crystal lattice of the metal influences the growth of the grains of FeCr_2O_4 . In the diffusion layer of the 9Cr ODS 2 week sample, there is a finger-like structure of FeCr_2O_4 found along the grain boundaries of the iron grains. In the 9Cr ODS four week sample, the finger-like structure no longer exists, but instead is replaced by a solid band of Cr_2O_3 at the front of the oxide at the diffusion layer/metal interface with FeCr_2O_4 trailing immediately behind the Cr_2O_3 .

3.2 Analysis of oxide layers formed after exposure to LBE

The alloys examined for LBE analysis are Alloy #3 and HT-9, with chemical compositions listed previously in Table 2.1. Alloy #3 is a model alloy consisting of only two elements: iron and chromium. The alloy HT-9 has similar chromium content to Alloy #3, but has additional elements of nickel, silicon, and manganese all of which are present in less than 1 wt%. The comparison of the TEM examinations between the oxide layers formed on these two alloys shows how the addition of minor alloying elements affects the structure of the oxide layer and consequently the corrosion behavior.

Figure 3.35 shows optical images of Alloy #3 and HT-9 which allow a view of the metal grains far from the oxide. The metal grains in Alloy #3 are equiaxed, appear homogeneous from the surface, and have dimensions of no less than 10 μm on any edge. The metal grains of HT-9 appear on the average smaller than those of Alloy #3 and have laths (sub-grain boundaries) on each grain reaching from one end of the grain to the other (Figure 3.35(b)).

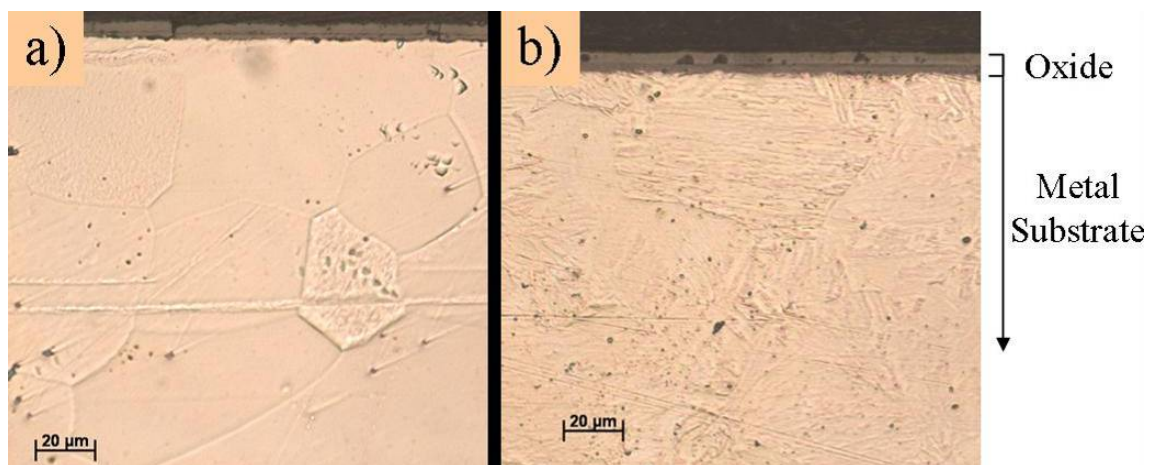


Figure 3.35: Optical images of LBE corroded (a) Alloy #3 and (b) HT-9.

3.2.1 Analysis of oxide layer formed on Alloy #3 after 4 weeks exposure to 500°C LBE

The oxide layer formed on Alloy #3 after corrosion exhibits two distinct sub-layers: an outer oxide and an inner oxide layer. No diffusion layer was found using TEM. The SEM image in Figure 3.36 shows the interface between the inner oxide/metal to be porous. The location chosen for the TEM specimen appeared on the surface to have the least porosity, but the porosity beneath the surface between the inner oxide/metal layers caused the specimen to split along the interface during preparation in the FIB, as shown in Figure 3.36. The image shows the outer and inner oxide layers to be approximately 3.75 μm and 2.5 μm , respectively.

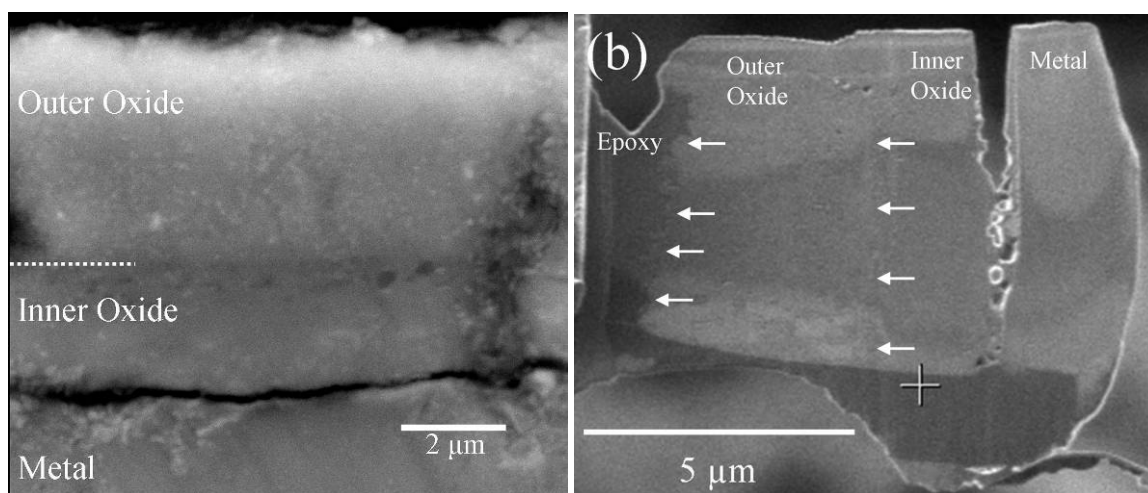


Figure 3.36: (a) SEM backscatter electron image of Alloy #3 showing the oxide layers and (b) FIB image of porous inner oxide/metal interface during sample preparation.

Figure 3.37 shows a TEM bright field image which reveals the entire oxide sub-layer structure. Starting from the top of the image, the regions shown are: the epoxy, the outer oxide, the porous region within the inner oxide along the inner oxide/outer oxide interface, the inner oxide, the remaining porous region along the metal/inner oxide interface, and the metal.

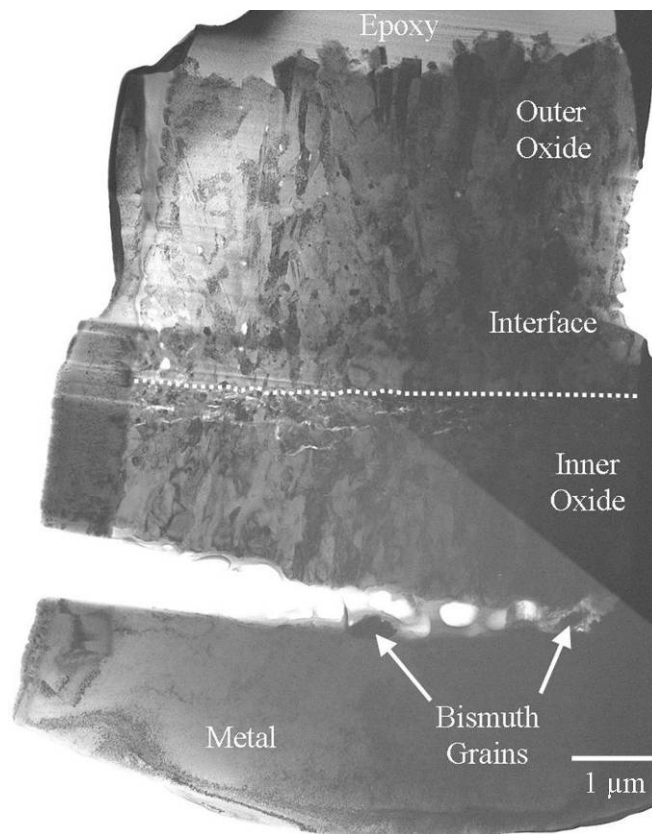


Figure 3.37: TEM bright field image of entire Alloy #3 specimen.

The surface of the outer oxide layer varies up to one micron from minimum to maximum distance from the outer oxide/inner oxide interface as seen in Figure 3.37. The outer oxide layer exhibits mostly columnar grains, which are either perpendicular or are slightly angled from the normal to the outer oxide/inner oxide interface. The outer oxide grains are up to 2 μm in length and up to 400 nm wide. There are equiaxed grains of up to 400 nm in diameter as seen in the outer oxide layer at the outer oxide/inner oxide interface in the TEM bright field image in Figure 3.38. The porosity along the outer oxide/inner oxide interface is less than the porosity along the inner oxide/metal interface so that the specimen has remained intact along that interface.

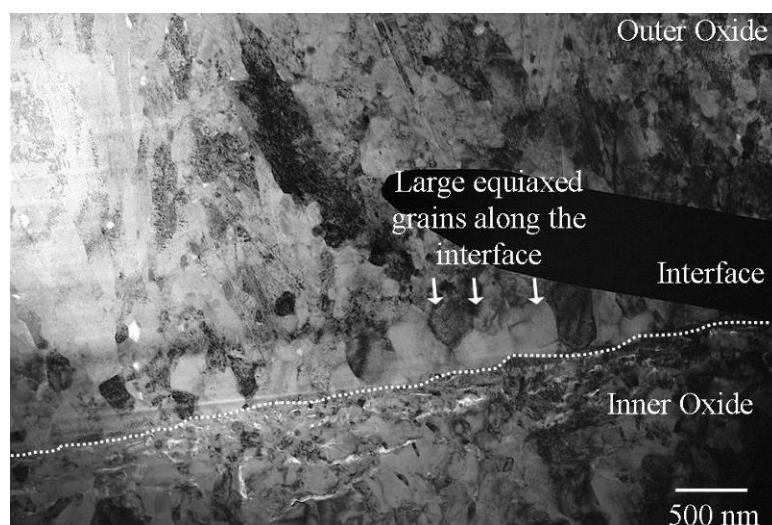


Figure 3.38: TEM bright field image of large equiaxed grains along outer oxide/inner oxide interface of Alloy #3. (Note: The beam stop is present in this image.)

The inner oxide layer shown in Figure 3.39 has short semi-columnar grains as well as equiaxed grains which are up to one micron in length and 400 nm wide. The inner oxide grains show no preferred orientation.

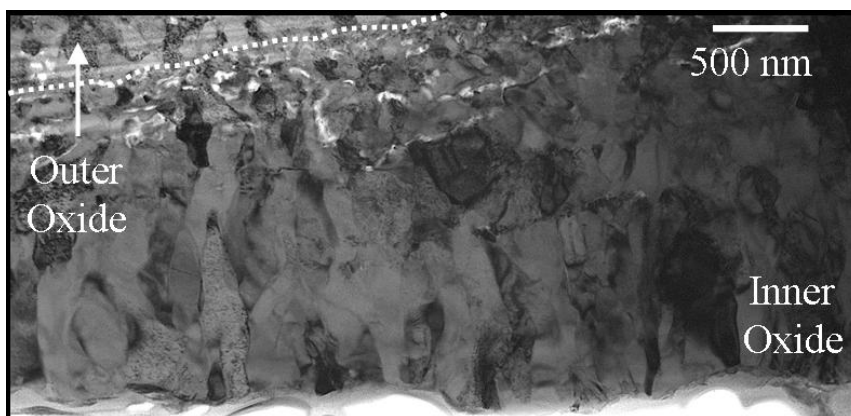


Figure 3.39: TEM bright field image of Alloy #3 inner oxide grain structure.

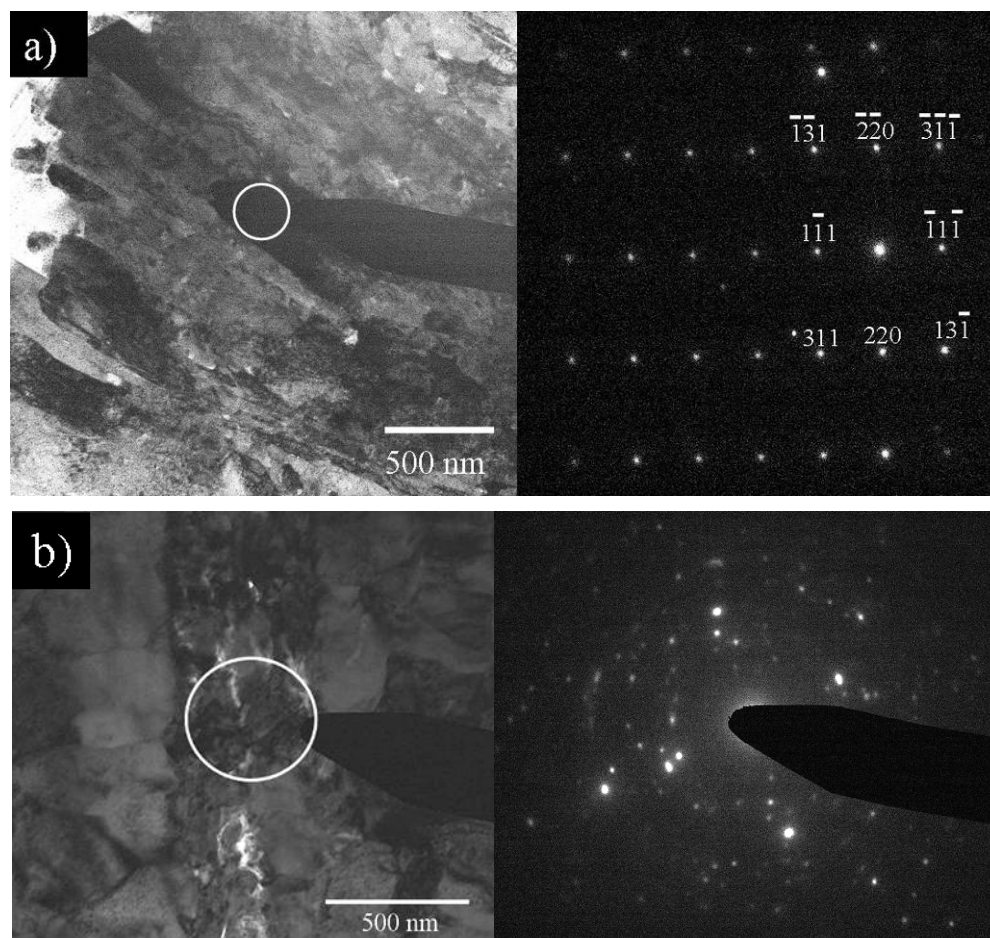
After initial SEM and TEM bright field analysis, TEM diffraction patterns were taken to help determine which phases are present in each sub-layer.

The TEM diffraction pattern in Figure 3.40(a) was taken from the outer oxide layer and indexed as Fe_3O_4 with a zone axis of $[-112]$. All diffraction patterns from the outer oxide layer were indexed as Fe_3O_4 .

Diffraction patterns within the inner oxide along the outer oxide/inner oxide interface that included the semi-porous region showed spotty to full rings, as shown in Figure 3.40(b), as opposed to the crystalline spot pattern that would be expected considering the outer oxide and inner oxide have crystalline spot diffraction patterns. The diffraction patterns characteristic of this region are clearly distinct from the other regions

but could not be indexed. The bright field images show smaller grains along the outer oxide/inner oxide interface in contrast to the larger grains found in each respective layer.

A TEM diffraction pattern from the inner oxide layer is shown in Figure 3.40(c) and indexed as FeCr_2O_4 with a zone axis of $[011]$. All diffraction patterns from the inner oxide were indexed as FeCr_2O_4 .



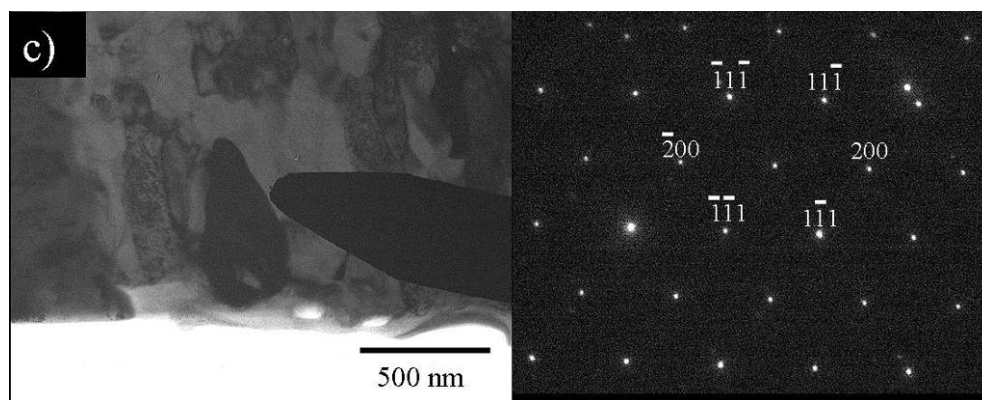


Figure 3.40: TEM diffraction patterns and corresponding bright field images of (a) a Fe_3O_4 grain with zone axis $[-112]$ within the outer oxide layer, (b) an unindexed pattern from a region at the outer oxide/inner oxide interface, and (c) a FeCr_2O_4 grain with zone axis $[011]$ within inner oxide layer of Alloy #3.

An oval grain approximately 300 nm wide by 400 nm long was found (Figure 3.41) still attached to the metal and has a spot pattern much smaller (approximately a factor of 3) than the metal, indicating a larger lattice parameter. The diffraction pattern was indexed with a zone axis of $[101]$ and found to have d-spacings of 3.96, 3.75, and 3.30 Å corresponding to values tabulated in the Powder Diffraction File for bismuth (44-1246) of 3.954, 3.737, and 3.28 Å, respectively.

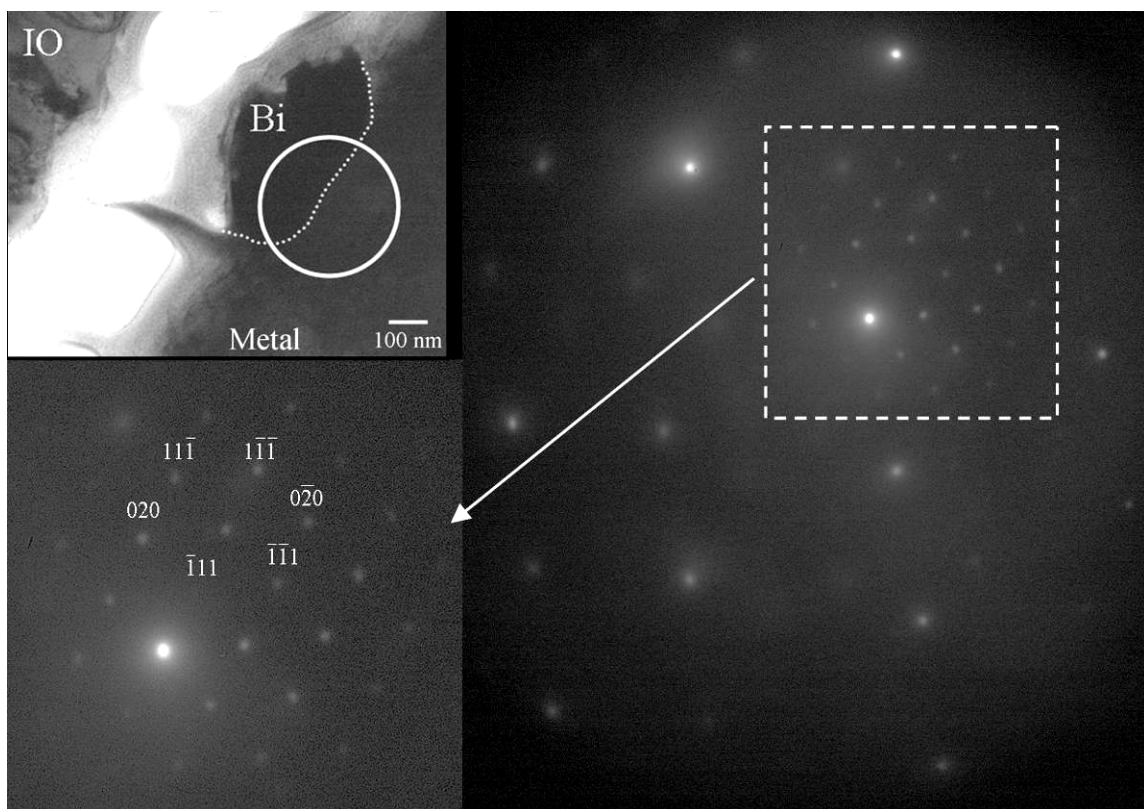


Figure 3.41: TEM bright field image and corresponding diffraction pattern of bismuth grain with zone axis $[101]$.

Energy Dispersion Spectroscopy analysis, providing chemical information to be coupled with the preceding diffraction pattern analysis, was performed on each layer for the purpose of confirming the identification of phases within each layer.

EDS analysis shows no chromium to be present in the outer oxide. This information combined with TEM diffraction analysis indicates that the outer oxide consists of only Fe_3O_4 . EDS analysis shows chromium to be present within the inner oxide which indicates FeCr_2O_4 to be present, but does not confirm or deny the presence of Fe_3O_4 .

EDS analysis shows minute traces of lead and bismuth within the inner oxide, but shows larger amounts of lead throughout the outer oxide. Figure 3.42 shows plots of the ratios of the amplitudes of the $L_{\alpha 1}$ spectral lines for Bi/Fe and Pb/Fe. It can be seen from these plots that there is a significant enrichment of bismuth at the metal/inner oxide interface while lead is enriched throughout the outer oxide. The presence of lead in the outer layer is not unexpected, since the sample was corroded in lead bismuth eutectic and it is generally agreed that the outer oxide/inner oxide interface corresponds to the original metal surface before oxidation. Therefore, the penetration of lead is more likely in the outer oxide layer as opposed to the inner oxide layer.

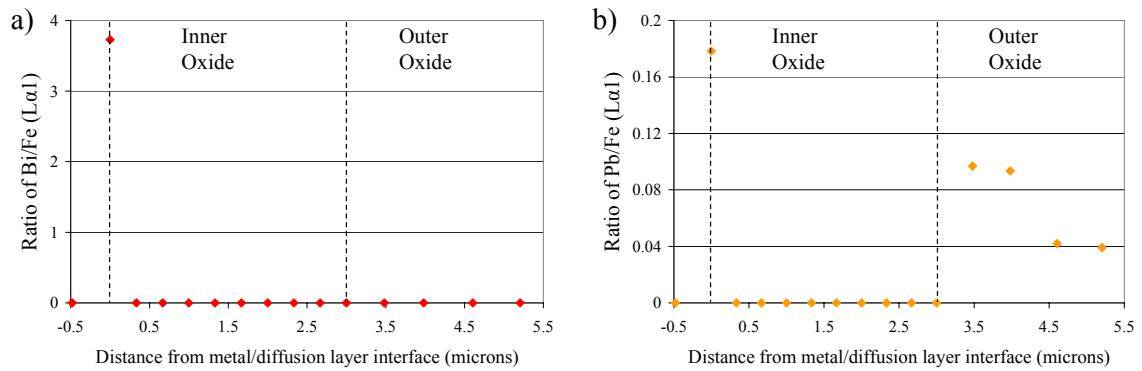


Figure 3.42: TEM EDS of bismuth and lead $L_{\alpha 1}$ spectral emission lines throughout Alloy #3 from metal/diffusion layer interface with emphasis on (a) Bi/Fe ratio and (b) Pb/Fe ratio.

The outer surface of the outer oxide layer shows a box-like grain structure. EDS spectra taken from those grains and shown in Figure 3.43 exhibit, surprisingly, slightly less lead and bismuth than the rest of the outer oxide. EDS analysis confirms that the

box-like structures are extensions of the grains within the outer oxide or, possibly, re-deposition of particulates from the solution, as opposed to particles of LBE adhering to the surface.

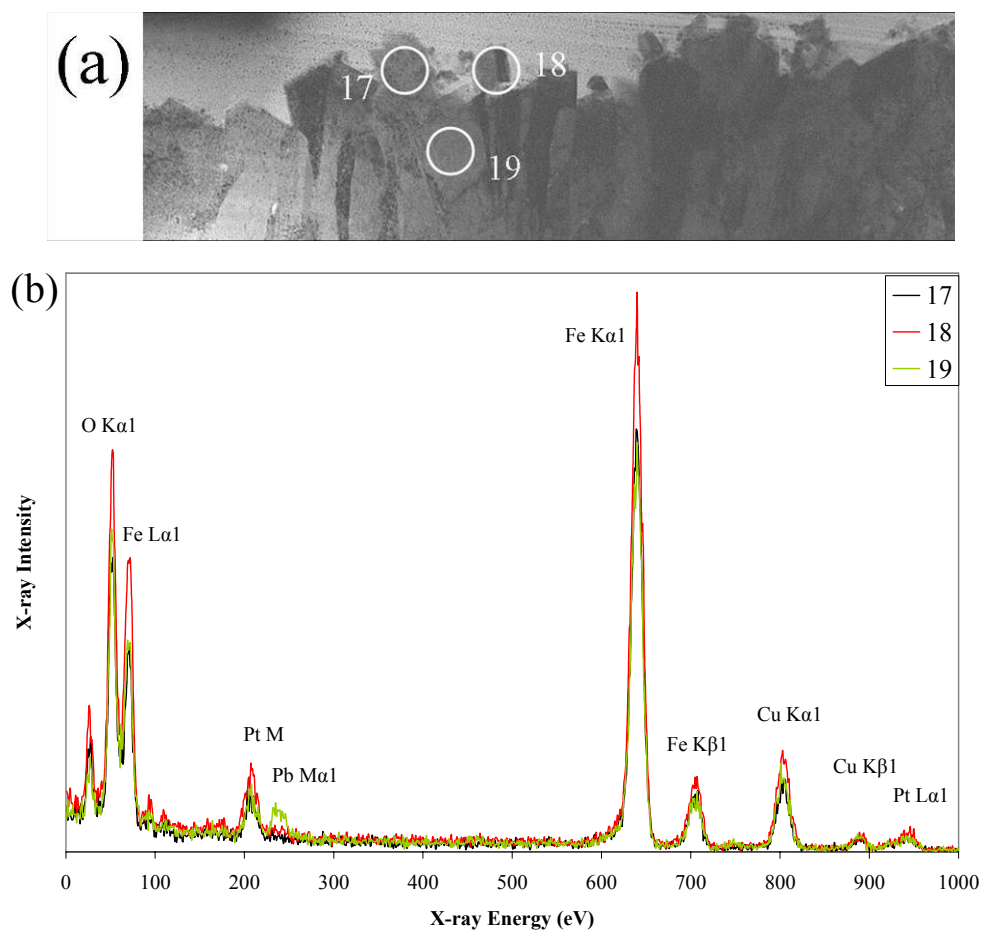


Figure 3.43: EDS (a) locations and (b) spectra overlay of box-like surface structures and a reference point within the outer oxide layer for Alloy #3.

It is interesting to note that large amounts of lead and bismuth were found by EDS analysis along the inner oxide/metal interface. EDS analysis was performed on two grains

at the inner oxide/metal interface and on a reference inner oxide grain for comparison as shown in Figure 3.44. The spectra (Figure 3.45) for the grains at locations 2 & 20 have four well defined bismuth peaks as well as reduced iron, chromium, and oxygen peaks. This confirms the TEM diffraction information, which indicated the grains to be bismuth.

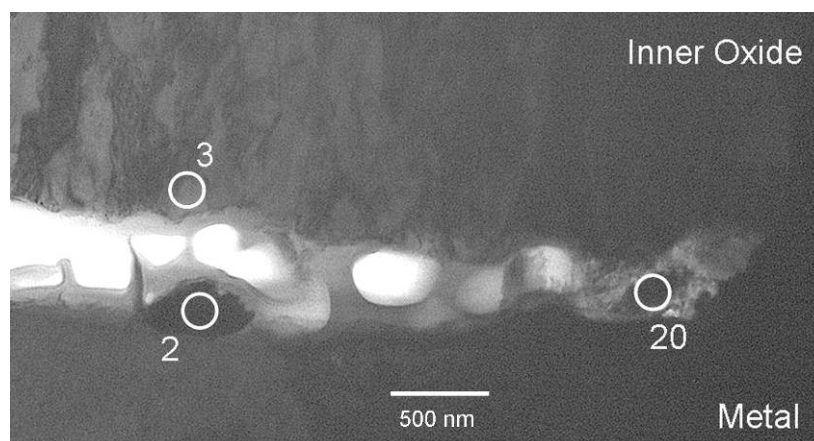


Figure 3.44: EDS locations of reference inner oxide (3) and bismuth grains (2 & 20).

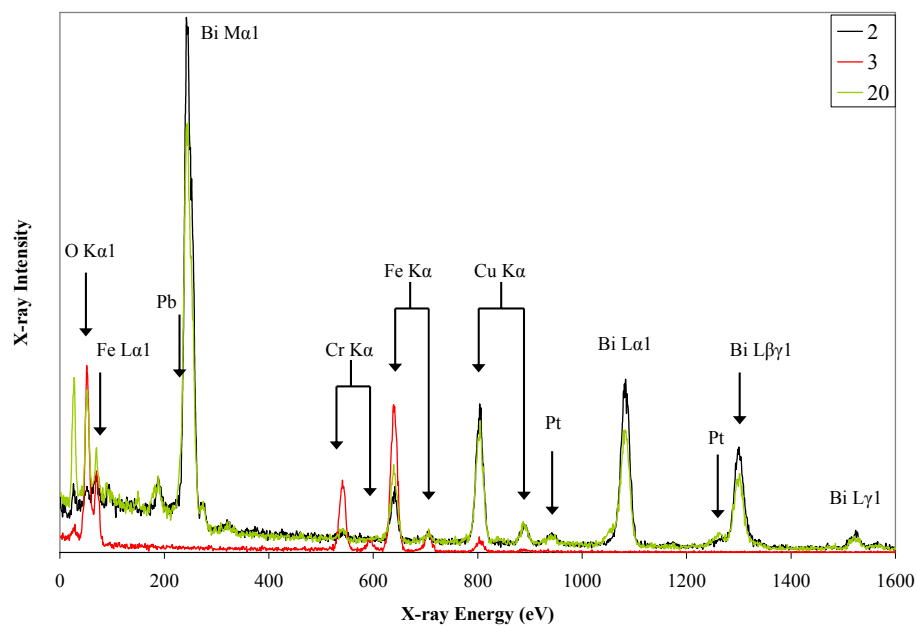


Figure 3.45: EDS spectra of bismuth grains (black & green) and reference inner oxide spectrum (red).

In addition to TEM analysis, the oxide was also examined by the APS at Argonne National Laboratory in order to acquire synchrotron diffraction and fluorescence information.

The synchrotron fluorescence data in Figures 3.46 and 3.47 agree with the TEM information, in respect to the oxide layer thicknesses as well as the presence of a porous metal/inner oxide interface. Figure 3.46 shows the X-ray counts of iron and chromium $K_{\alpha 1}$ peaks, which indicate the inner oxide with an increase of chromium and a decrease of iron, and the outer oxide with an increase in iron and a decrease of chromium to zero. Additionally, the iron content in the outer oxide decreases from the outermost portion of the oxide to the outer oxide/inner oxide interface. This agrees with the SEM image in Figure 3.36(a) which appears to show higher LBE contamination closer to the outer oxide/inner oxide interface. Figure 3.47 shows X-ray counts of copper $K_{\alpha 1}$ peaks with a significant increase of copper at the metal/inner oxide interface, which can be attributed to re-deposition of the brass tubing or the epoxy into a very porous region during polishing. This would be expected since the sample was found to be very porous at the metal/inner oxide interface through SEM and TEM imaging. Finally, the epoxy region of Figure 3.46 shows a step-wise decrease in iron, which can be attributed to the jagged surface of the outer oxide layer. Since the synchrotron microbeam is 0.2 m wide by 2 m

long, it is expected that the smaller perturbations of the outer oxide surface would produce a step-wise decrease.

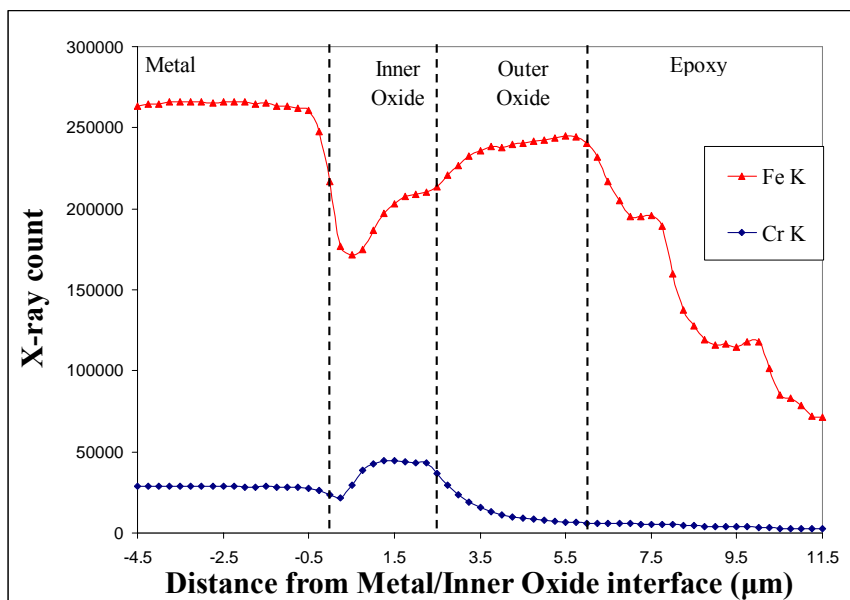


Figure 3.46: Microbeam synchrotron fluorescence of counts associated with iron and chromium $K_{\alpha 1}$ for Alloy #3.

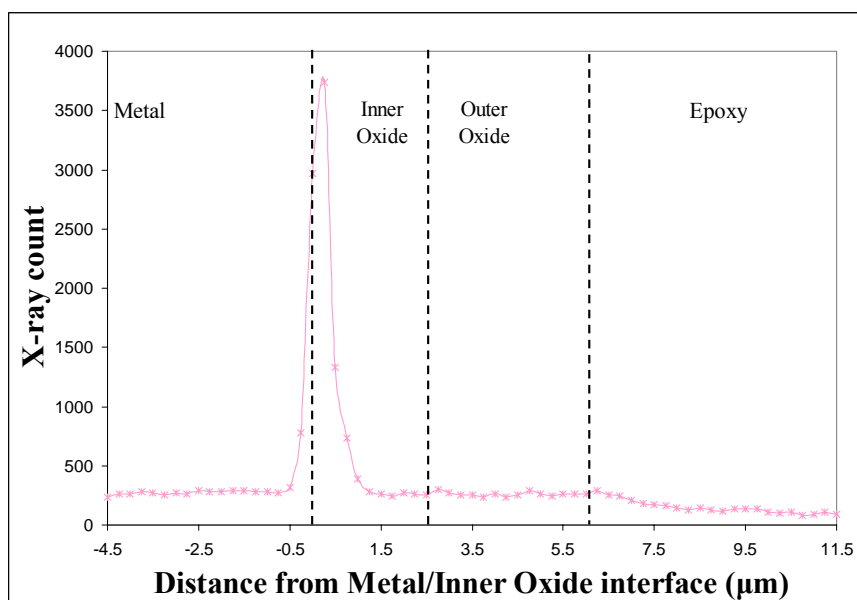


Figure 3.47: Microbeam synchrotron fluorescence of counts associated with copper $K_{\alpha 1}$ for Alloy #3.

A summary of the phases found in each sub-layer of the oxide are listed in Table 3.3.

Table 3.3: List of phases found within the oxide layers of Alloy #3.

Layer	Outer oxide	Inner oxide	Inner oxide/metal interface	Material
Phases Found	Fe_3O_4	FeCr_2O_4 and possibly Fe_3O_4	bismuth	Fe - bcc

3.2.2 Analysis of oxide layer formed on HT-9 after 4 weeks exposure to 500°C LBE

The oxide layer formed on HT-9 after corrosion exhibits two distinct sub-layers as seen in Figure 3.48: an outer oxide and an inner oxide layer with thicknesses of approximately 4.24 μm and 3.12 μm , respectively. The ratio of the outer oxide layer to the inner oxide layer is approximately 1.36. The SEM image in Figure 3.48 shows a significant amount of lighter features throughout the inner part of the outer oxide. It may be possible to correlate these lighter features to either lead or bismuth or a combination of both, since these elements are heavier than iron, chromium, and oxygen and would therefore appear brighter in a SEM image and evidence of LBE contamination in the outer oxide layer was found in the oxide formed on Alloy #3. The full TEM sample is shown in the bright field image in Figure 3.49. This sample underwent damage during milling, which can be seen by the artifacts mentioned in section 2.2.3.

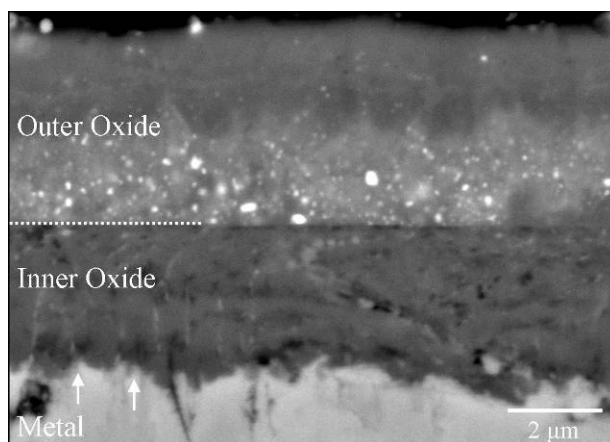


Figure 3.48: SEM backscatter electron image of HT-9, after 4 weeks exposure to 500°C LBE.

The outer oxide consists of long thin grains (up to 2 μm long by 400 nm wide) and smaller equiaxed grains ($\sim 300\text{-}400$ nm in diameter). An equiaxed grain (800 nm long by 400 nm wide) was found within the outer oxide layer at the inner oxide/outer oxide interface. This grain appeared dark, during bright field imaging, at all angles of rotation of the sample. The inner oxide/outer oxide interface is clearly distinguishable in the TEM image and is shown by the white dotted line at the right in Figure 3.49. The inner oxide exhibits bright field contrast from a group of narrow elongated grains, approximately 2 μm long by 300-400 nm wide (arrowed), as sketched schematically in Figure 3.49. These grains are also visible in the metal region (arrowed), and are likely a inter lath grain boundary phase, either retained austenite or ferrite. In the inner oxide these grains are associated with fine porosity (shown in more detail in Figure 3.50(b)), possibly resulting from the oxidation process. There are also equiaxed oxide grains within the inner oxide layer up to 250 nm in diameter. The metal layer has a large metal grain of approximately 2 μm wide by 3 μm long at the metal/inner oxide interface.

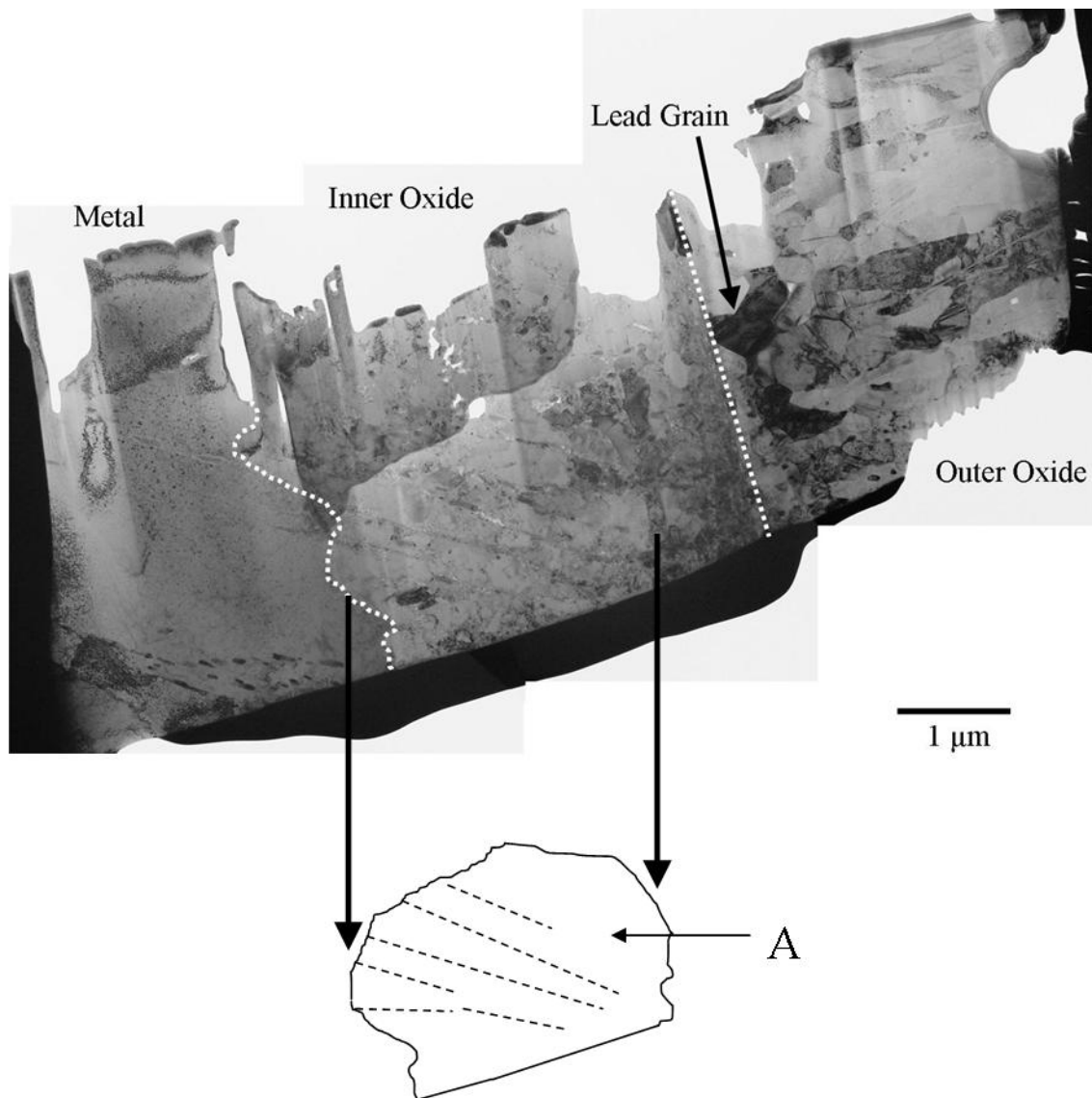


Figure 3.49: TEM bright field image of entire HT-9, after 4 weeks exposure to 500°C LBE and sketch of FeCr₂O₄ grains (region “A”) within the inner oxide layer with pores and small grains in between the grains depicted as dashed lines.

After initial SEM and TEM bright field analysis, TEM diffraction patterns were taken to help determine which phases are present in each sub-layer.

A diffraction pattern was taken from a grain within the outer oxide layer (Figure 3.50(a)) and indexed as Fe₃O₄ with a zone axis of [-112]. Another diffraction

pattern was taken from a grain within the inner oxide layer (Figure 3.50(b)) and indexed as FeCr_2O_4 with a zone axis of $[-111]$. The highly oriented area of the inner oxide layer, from which the diffraction pattern was taken for the inner oxide grain, exhibits the exact same diffraction pattern. There are small areas within this region that do not diffract to the same conditions, as seen by the contrast of lighter areas as opposed to the generally dark region. These lighter areas mostly consist of pores but also of very fine grains as mentioned previously.

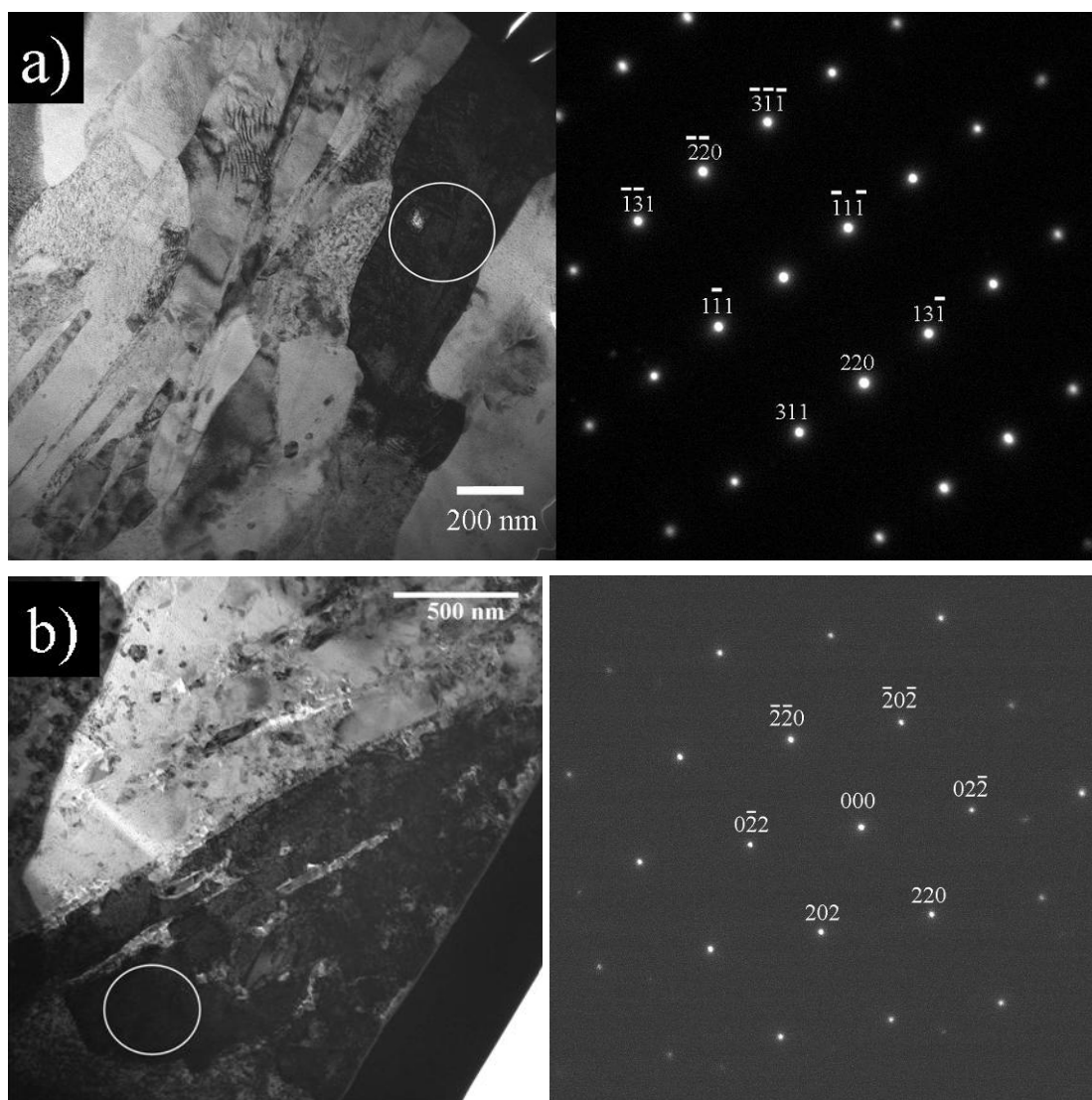


Figure 3.50: TEM diffraction patterns and corresponding bright field images from HT-9, after 4 weeks exposure to 500°C LBE, of (a) a Fe_3O_4 grain within the outer oxide layer, with a zone axis of $[-112]$ and (b) a FeCr_2O_4 grain within the inner oxide, with a zone axis of $[-111]$ showing a highly-structured region within the inner oxide layer.

Energy Dispersion Spectroscopy analysis, providing chemical information to be coupled with the preceding diffraction pattern analysis, was performed on each layer with the purpose of confirming the identification of phases within each layer.

EDS analysis shows no chromium to be present in the outer oxide layer, therefore, combined with the TEM diffraction analysis this indicates that the outer oxide layer consists of only Fe_3O_4 . In contrast, EDS analysis shows chromium to be present in the inner oxide layer, therefore it can be said that FeCr_2O_4 is definitely present but nothing can be said of the presence of Fe_3O_4 in the inner oxide layer.

The diffraction pattern from the region of highly structured grains within the inner oxide layer was indexed as FeCr_2O_4 and EDS analysis shows chromium to be present throughout the area, which indicates the entire sub-structure to consist of FeCr_2O_4 .

It is interesting to note that a large equiaxed lead grain (400 nm wide by 600 nm long) was found within the outer oxide along the outer oxide/inner oxide interface. The lead grain was discovered through EDS and its presence is verified by the spectrum in Figure 3.51, which shows strong lead peaks.

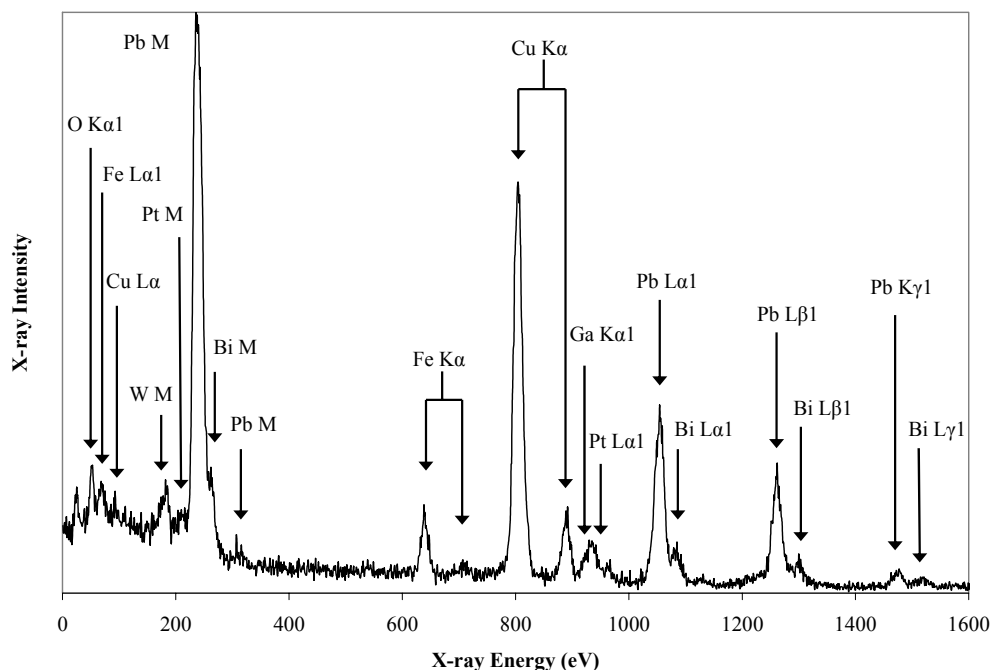


Figure 3.51: EDS spectrum of lead grain in outer oxide of HT-9, after 4 weeks exposure to 500°C LBE.

The metal grain at the inner oxide/metal interface is about the same size and shape of the highly-structured group of grains within the inner oxide along the metal/inner oxide interface. This indicates that the oxide grains within the inner oxide layer are developed from the iron grains in the metal, although, unlike the inner oxide layer for the HT-9 SCW sample the TEM diffraction analysis from the inner oxide layer for this sample did not have Fe-bcc diffraction spots.

In addition to TEM analysis, the oxide was also examined by the APS at Argonne National Laboratory in order to acquire microbeam synchrotron diffraction and fluorescence information.

The microbeam synchrotron fluorescence data in Figure 3.52 shows the X-ray counts of iron and chromium $K_{\alpha 1}$, which indicate the inner oxide layer with an increase of chromium and a decrease of iron, and the outer oxide layer with an increase in iron and a decrease of chromium to zero. Additionally, the iron content in the outer oxide layer decreases from the outermost portion of the oxide to the outer oxide/inner oxide interface. This agrees with the SEM image in Figure 3.48 which appears to show higher LBE contamination closer to the outer oxide/inner oxide interface. The outer oxide layer shows no presence of chromium which agrees with TEM analysis.

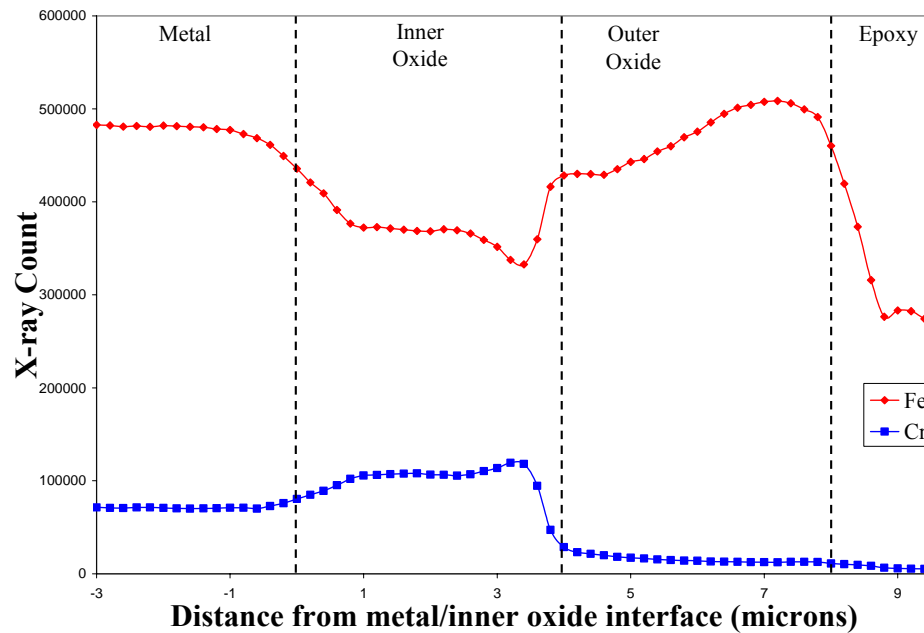


Figure 3.52: Microbeam synchrotron fluorescence of counts associated with iron and chromium $K_{\alpha 1}$ for HT-9, after 4 weeks exposure to 500°C LBE.

A summary of the phases found in each sub-layer of the oxide are listed in

Table 3.4.

Table 3.4: List of phases found within the various layer of HT-9 500°C, 4 weeks LBE corroded.

Layer	Outer oxide	Inner oxide	Metal
Phases Found	Fe ₃ O ₄ and lead	FeCr ₂ O ₄ and possibly Fe ₃ O ₄	Fe-bcc

3.2.3 LBE Alloy Corrosion Summary

Each of the oxide layers developed on HT-9 and Alloy #3 have an outer oxide layer and an inner oxide layer, but do not have a diffusion layer. These sub-layers exhibit the same phases for both the HT-9 sample and Alloy #3. Lead contamination was found in the outer oxide for both alloys, but bismuth contamination at the inner oxide/metal interface was only found in Alloy #3. This is likely due to the high porosity at that interface for Alloy #3 which might have allowed the LBE to find its way there during corrosion. The inner oxide layer for HT-9 is highly structured and evidence shows that FeCr₂O₄ takes the form of the metal grains as it advances through the metal, whereas the inner oxide layer for Alloy #3 does not.

Chapter 4

Summary and Conclusions

Oxide layers formed on steel alloys during corrosion in supercritical water (SCW) and in lead-bismuth (LBE) were characterized using transmission electron microscopy (TEM), with the goal of understanding corrosion behavior. The oxides studied were formed on a model steel alloy (91 wt% Fe and 9 wt% Cr) in LBE, on HT-9 in LBE and SCW, and on 9Cr ODS in SCW at two weeks and four weeks. The oxides were characterized mainly using TEM imaging and diffraction, to determine phases present, oxide morphology and chemical composition, orientation relationships, grain size and shape, etc. The samples were also examined with optical microscopy, scanning electron microscopy, energy dispersion spectroscopy, electron energy loss spectroscopy, and complimentary parallel work performed using microbeam X-ray diffraction and fluorescence. TEM samples were prepared using a focused ion beam. The focused ion beam allowed for site-specific electron transparency of the desired regions with large viewing areas and fast production time. The main conclusions are as follows:

1. The oxide layers studied exhibit sub-layers: an Fe-rich outer oxide, a Cr-rich inner oxide; in the SCW samples a diffusion layer, composed of a mixture of metal and oxide was also observed. Columnar grains were seen in the outer layer, while the inner layer exhibited more equiaxed grains. Diffraction patterns taken from the inner and outer oxide layers could be indexed as either Fe_3O_4 or FeCr_2O_4 . Coupled with chemical analysis, the outer layer was found to be composed of Fe_3O_4 and the inner

layer thought to be composed of a mixture of both phases. The ratios of the outer oxide layer to the inner oxide layer for both HT-9 samples were approximately the same, but different for the other alloys.

2. The structure of the outer oxide layers formed in SCW and LBE showed some differences. The outer oxide columnar grains of the LBE samples tended to be smaller than those of the SCW samples, while the equiaxed inner oxide grains of the LBE samples were larger than those of the SCW samples. Even though the HT-9 SCW sample was exposed for one less week than the LBE sample, the overall oxide thickness on the HT-9 SCW sample was larger. An influence of the original metal microstructure on the oxide formation was seen in HT-9, through an orientation relationship between Fe-bcc and the oxide grains. Neither of the lead-bismuth eutectic corroded samples developed a diffusion layer, whereas both supercritical water samples developed diffusion layers between the inner oxide layer and the base metal. The lack of a diffusion layer for the LBE corroded samples may be due to the lower availability of oxygen for oxide development.
3. For each case, the oxide sub-layers thought to be protective were studied in detail.
 - a. For 9Cr ODS, the protective layer is thought to be the diffusion layer. Diffraction analysis of this layer shows the evolution of $\text{FeCr}_2\text{O}_4 + \text{Fe}$ into a Cr_2O_3 ribbon at the diffusion layer/metal interface between 2 weeks and 4 weeks. EELS analysis shows the ribbon at the oxide front to be composed primarily of Cr_2O_3 , but with small grains of Fe-bcc within the ribbon. The development of the Cr_2O_3 layer is associated with a shrinking of the diffusion layer relative to the overall oxide thickness.

- b. For HT-9, the structure of the bare metal influences the oxide growth, leading to “packs” of similarly oriented grains. SEM images showed that oxide advancement followed the metal lath sub-boundaries. The SCW sample exhibits an orientation relationship of Fe-bcc and FeCr_2O_4 within the diffusion layer. This orientation relationship was found to extend from the diffusion layer into the inner oxide layer. The diffusion layer of HT-9 formed in SCW exhibits a highly oriented structure consisting of Fe-bcc and FeCr_2O_4 , similar to that of the inner oxide layer. It is postulated that as the oxygen diffuses into a metal grain for HT-9, FeCr_2O_4 sub-grains develop evenly throughout the metal grain until the iron lattice gives way to the FeCr_2O_4 lattice(s).
 - c. For Alloy #3 (91 wt% Fe and 9 wt% Cr), it does not appear that a protective oxide layer has formed. The highly porous inner oxide/metal interface and the LBE contamination found along that interface indicate that the metal is directly exposed to the LBE, despite having developed an oxide layer. Even though the addition of chromium to steel alloys is known to aid in the development of a protective oxide, it is apparent that additional minor alloying elements of the other steel alloys that were studied, increased oxidation resistance.
4. Evidence was found for ingress of the lead-bismuth coolant into the oxide layer. A lead grain was found by EDS at the outer oxide/inner oxide interface of HT-9 and two bismuth grains were found at the inner oxide/metal interface of Alloy #3. SEM images show light features in the outer oxide layers of the LBE corroded samples, which can be correlated to LBE contamination. Since lead and bismuth were found

individually within the oxide layer, this suggests that the lead and bismuth may separate during cool-down, or possibly upon ingress into the layer at high temperature.

5. If the band of Cr_2O_3 is formed from the FeCr_2O_4 grains within the diffusion layer of 9Cr ODS, it is postulated that the remaining iron cation migrates to the outer oxide layer while the remaining oxygen anion is available for further oxidation of the base alloy. The apparent effect of the structure of the metal grains for HT-9, on the structure of the oxide layer formed upon it, indicates that the metal grain boundaries are the preferred thoroughfares for the exchange of iron and oxygen atoms during corrosion. The large size of the metal grains and the lack of a diffusion layer for Alloy #3 suggest that iron diffusions from the metal/inner oxide interface through the inner oxide layer to the outer oxide to form Fe_3O_4 , or from the surface of the metal to the LBE since the inner oxide/metal interface was found to be very porous with significant amounts of LBE.

It is clear that the materials issues related to Gen-IV reactors, including the SCWR and LFR studied in this work, are considerable. The high temperatures, high radiation doses, and aggressive corrosion environment raise significant questions regarding irradiation, creep strength, and corrosion resistance. This study addressed the last of these concerns, that is, the ability of designers to achieve corrosion protection by proper alloy design. The study focused, in particular, on the mechanisms of how such protection is achieved and furnished clues to guide future alloy selection and fabrication, in terms of their ability to form a protective and stable oxide layer.

Bibliography

“A Technology Roadmap for Generation IV Nuclear Energy Systems.” http://nuclear.energy.gov/genIV/documents/gen_iv_roadmap.pdf U.S. DOE Nuclear Energy Research Advisory Committee and the Generation IV International Forum, December 2002.

- . A.T. Motta, A. Yilmazbayhan, E. Breval, and R.J. Comstock. “Transmission electron microscopy examination of oxide layers formed on Zr alloys.” *Journal of Nuclear Materials*, v 349, n 3, March 1 (2006), p. 265-81.
- . A. Yilmazbayhan, A.T. Motta, R.J. Comstock, G.P. Sabol, Barry Lai, Zhonghou Cai. “Structure of zirconium alloy oxides formed in pure water studied with synchrotron radiation and optical microscopy: relation to corrosion rate.” *Journal of Nuclear Materials*, v 324, n1, January 1 (2004), p. 6-22.
- . IAEA. “Waterside Corrosion of Zirconium Alloys in Nuclear Power plants.” *IAEA-TECDOC-996*, 1998.
- . L. Tan, Y. Yang, and T.R. Allen. “Oxidation behavior of iron-based alloy HCM12A exposed in supercritical water.” *Corrosion Science* 48 (2006), p. 3123-3138.
- . X. Ren, K. Sridharan, and T.R. Allen. “Corrosion of ferritic-martensitic steel HT9 in supercritical water.” *Journal of Nuclear Materials* 358 (2006), p. 227-234.
- . Y. Chen, K. Sridharan, S. Ukai, and T.R. Allen. “Microstructural examination of oxide layers formed on an oxide dispersion strengthened ferritic steel exposed to supercritical water.” *Journal of Nuclear Materials* 359 (2006), p. 50-58.
- . Y. Chen, K. Sridharan, S. Ukai, and T.R. Allen. “Oxidation of 9Cr oxide dispersion strengthened steel exposed in supercritical water.” *Journal of Nuclear Materials* 371 (2007), p. 118-128.
- . S. Ohtuska, S. Ukai, M. Fujiwara, T. Kaito, and T. Narita. “Improvement of Mechanical Properties of 9Cr ODS Martensitic Steel by Controlling Titanium Concentration.” *Materials Transactions* vol. 46, no. 3 (2005), p. 487-492.
- . Personal comments of Peter Hosemann, Ph.D. candidate of Montanuniversität Leoben, Austria, March 26, 2008.

- . K. Sridharan, A. Zillmer, J.R. Licht, T.R. Allen, M.H. Anderson, and L. Tan. "Corrosion Behavior of Candidate Alloys for Supercritical Water Reactors." *Proceedings of ICAPP '04*. Pittsburgh, PA USA (2004), Paper 4136.
- . Personal correspondence with Yun Chen, Lizhen Tan, Kumar Sridharan, and Todd Allen of The University of Wisconsin, March 3, 2008.
- . Orlov, Y.I. "Proceedings: International Workshop on Physics of Accelerator-Driven Systems for Nuclear Transmutation and Energy Production." Trento, Italy. 1997.
- . V. Tcharnotskaia, C. Ammerman, and K. Woloshun. "Results from the Initial Operation of the LANL DELTA Loop." <http://nstg.nevada.edu/LBE/pdf/Tcharnotskaia.pdf>. Accessed March 27, 2008.
- . Java Electron Microscopy Image Simulation, v32125u2007, developed by Pierre Stadelmann at the Centre Interdépartmental de Microscopie Electronique of the Ecole Polytechnique Fédérale de Lausanne.
- . A. Yilmazbayhan. "Microstructural Basis of Uniform Corrosion in Zr Alloys." *The Pennsylvania State University*, Ph.D. thesis in Nuclear Engineering, 2004.
- . Giannuzzi, Lucille A. and Fred A. Stevie. "Introduction to Focused Ion Beams: Instrumentation, Theory, Techniques and Practice." Springer, 2005.
- . L.A. Giannuzzi, J.L. Drown, S.R. Brown, R.B. Irwin, and F.A. Stevie. "Focused Ion Beam Milling and Microminipulation Lift-Out for Site Specific Cross-Section TEM Specimen Preparation." *Materials Research Society Symposium Proceedings*, 480 (1997), p. 19-27.
- . J. Zhang and N. Li. "Oxidation Mechanism of Steel in Liquid-Lead Alloys." *Oxidation of Metals*, vol. 63 (2005), p. 353-381.
- . A.T. Motta, A.D. Siwy, J.M. Kunkle, J.B. Bischoff, R.J. Comstock, Y. Chen, and T.R. Allen. "Microbeam Synchrotron Radiation Diffraction and Fluorescence Study of Oxide Layers formed on 9Cr ODS Steel in Supercritical Water." *Proceedings of the 13th Environmental Degradation of Materials in Nuclear Power Plants*, (2007), NACE.

Appendix

Power Diffraction Files

The following tables summarize the power diffraction files used in the indexing of the diffraction patterns given in this paper. The values were obtained from the ICDD [PCDPDFWIN v. 2.01, 1998].

Table A.1: ICDD #: 01-1262, Body-centered cubic, Fe, $a=2.857 \text{ \AA}$.

D-spacing (\AA)	Intensity	h	k	l
2.0300	100	1	1	0
1.4400	50	2	0	0
1.1700	80	2	1	1
1.0100	50	2	2	0
0.91000	60	3	1	0
0.83000	20	2	2	2
0.76000	60	3	2	1
0.67000	30	3	3	0
0.64000	20	4	2	0
0.61000	20	3	3	2
0.58000	20	4	2	2

Table A.2: ICDD #: 19-0629, Face-centered cubic Fe_3O_4 , $a=8.396 \text{ \AA}$.

D-spacing (\AA)	Intensity	h	k	l
4.852	8	1	1	1
2.967	30	2	2	0
2.532	100	3	1	1
2.4243	8	2	2	2
2.0993	20	4	0	0
1.7146	10	4	2	2
1.6158	30	5	1	1
1.4845	40	4	4	0
1.4192	2	5	3	1
1.3277	4	6	2	0
1.2807	10	5	3	3
1.2659	4	6	2	2
1.2119	2	4	4	4
1.1221	4	6	4	2
1.0930	12	7	3	1
1.0496	6	8	0	0
0.9896	2	6	6	0
0.9695	9	7	5	1
0.9632	4	6	6	2
0.9388	4	8	4	0
0.8952	2	6	6	4
0.8802	6	9	3	1
0.8569	8	8	4	4
0.8233	4	10	2	0
0.8117	6	9	5	1
0.80	4	10	2	2

Table A.3: ICDD #: 34-0140, Face-centered cubic FeCr_2O_4 , $a=8.3790 \text{ \AA}$.

D-spacing (\AA)	Intensity	h	k	l
4.8390	13	1	1	1
2.9620	33	2	2	0
2.5260	100	3	1	1
2.4180	7	2	2	2
2.0943	22	4	0	0
1.7105	11	4	2	2
1.6125	39	5	1	1
1.4812	48	4	4	0
1.4162	2	5	3	1
1.3247	3	6	2	0
1.2777	10	5	3	3
1.2632	5	6	2	2
1.2095	3	4	4	4
1.1734	1	7	1	1
1.1197	4	6	4	2
1.0907	12	7	3	1
1.0476	5	8	0	0
0.9873	2	6	6	0
0.9675	10	7	5	1
0.9612	2	6	6	0
0.9367	2	8	4	0
0.8931	1	6	6	4
0.8783	5	9	3	1
0.8552	12	8	4	4
0.8217	1	10	2	0
0.8101	7	9	5	1
0.8063	<1	10	2	2

Table A.4: ICDD #: 38-1479, Rhombohedral Cr_2O_3 , $a=4.95876 \text{ \AA}$, $c=13.5942 \text{ \AA}$.

D-spacing (\AA)	Intensity	h	k	l
3.6313	73	0	1	2
2.6653	100	1	0	4
2.4796	93	1	1	0
2.2658	7	0	0	6
2.1752	35	1	1	3
2.0477	6	2	0	2
1.8152	38	0	2	4
1.6723	87	1	1	6
1.6114	<1	2	1	1
1.5790	7	1	2	2
1.4649	28	2	1	4
1.4315	39	3	0	0
1.2958	14	1	0	10
1.2900	6	1	1	9
1.2394	9	2	2	0
1.2103	6	3	0	6
1.1958	1	2	2	3
1.1730	4	3	1	2
1.1485	7	0	2	10
1.1328	2	0	0	12
1.1238	7	1	3	4
1.0874	13	2	2	6
1.0602	1	0	4	2
1.0420	9	2	1	10
1.0306	1	1	1	12
1.0238	2	4	0	4
0.9750	<1	2	3	2
0.9583	<1	2	2	9
0.9463	6	3	2	4
0.937	5	4	1	0
0.9177	<1	4	1	3
0.8958	7	1	3	10
0.8883	3	3	0	12
0.8847	1	2	0	14
0.8660	10	4	1	6

Table A.5: ICDD #: 44-1246, Rhombohedral Bi, $a=4.547 \text{ \AA}$, $c=11.86 \text{ \AA}$.

D-spacing (\AA)	Intensity	h	k	l
3.9540	6	0	0	3
3.7370	2	1	0	1
3.2800	100	0	1	2
2.3690	27	1	0	4
2.2730	29	1	1	0
2.0320	5	0	1	5
1.9766	6	0	0	6
1.9423	<1	0	2	1
1.8686	13	2	0	2
1.6505	7	0	2	4
1.5565	3	1	0	7
1.5150	1	2	0	5
1.4918	8	1	1	6
1.4766	1	2	1	1
1.4436	10	1	2	2
1.3875	2	0	1	8
1.3303	5	2	1	5
1.3179	1	0	0	9
1.3126	2	3	0	0
1.2843	1	0	2	7
1.2608	<1	1	2	5
1.2456	<1	3	0	3
1.1843	<1	2	0	8
1.1404	1	1	1	9
1.1367	1	2	2	0
1.1182	<1	2	1	7
1.0935	1	3	0	6
1.0925	<1	2	2	3
1.0741	1	3	2	1
1.0504	<1	1	2	8
1.0401	<1	0	1	11
1.0248	1	1	3	4
1.0162	<1	0	2	10
0.99180	<1	3	1	5
0.98846	<1	0	0	12
0.98545	<1	2	2	6
0.97116	<1	0	4	2
0.94577	<1	2	0	11
0.93431	<1	4	0	4
0.93004	<1	3	0	9
0.92770	<1	2	1	10
0.91800	<1	1	3	7